Data-driven hydrodynamic models for Heaving Wave Energy Converters

by

Virag Mishra
B.E., Pt. Ravi Shankar Shukla University, India, 2005
M.S., Indian Institute of Technology, Madras, 2009

A Dissertation Submitted in Partial Fulfillment of the
Requirements for the Degree of

DOCTOR OF PHILOSOPHY

in the Department of Mechanical Engineering

Data-driven hydrodynamic models for Heaving Wave Energy Converters

by

Virag Mishra
B.E., Pt. Ravi Shankar Shukla University, India, 2005
M.S., Indian Institute of Technology, Madras, 2009

Supervisory Committee

Dr. Curran Crawford, Supervisor
(Department of Mechanical Engineering)

Dr. Bradley Buckham, Supervisor
(Department of Mechanical Engineering)

Dr. Peter Oshkai, Departmental Member
(Department of Mechanical Engineering)

Dr. Richard Dewey, Outside Member
(Ocean Networks Canada)

Supervisory Committee

Dr. Curran Crawford, Supervisor
(Department of Mechanical Engineering)

Dr. Bradley Buckham, Supervisor
(Department of Mechanical Engineering)

Dr. Peter Oshkai, Departmental Member
(Department of Mechanical Engineering)

Dr. Richard Dewey, Outside Member
(Ocean Networks Canada)

ABSTRACT

Empirical models based on linear and nonlinear potential theory that determine the forces on Wave Energy Converters (WECs) are essential as they can be used for structural, mechanical and control system design as well as performance prediction. In contrast to empirical modelling, Computational Fluid Dynamics (CFD) solves the mass and momentum balance equations for fluid domains. CFD and linear potential theory models represent two extreme in terms of capturing the full range of hydrodynamic effects. These are classified as white box models and the structure of these models is completely derived from first principles understanding of the system. In contrast black box models like a Artificial Neural Networks and Auto-Regressive with, Exogenous Input (ARX), map input and output behaviour of a system without any specific physics based structure. Grey box models do not strictly follow a first principles approach but are based on some observations of relationships between the hydrodynamic effects (*e.g.* buoyancy force) and system state (*e.g.* free surface height). The objective of this thesis is to propose a data driven grey box modelling

approach, which is computationally efficient compared to high fidelity white box models and still sufficiently accurate for the purpose of determining hydrodynamic forces on heaving WECs.

In this thesis, a unique data driven approach that combines features from existing works in modelling of WEC and application of nonlinear hysteretic systems is developed. To that end a CFD based Numerical Wave Tank that could provide the data needed to populate the new modelling framework is used. A hull which hydrodynamically represents a Self Reacting Point Absorbers (SRPAs) with heave plate is subjected to pan-chromatic wave fields and is forced to oscillate concomitantly. The results provide evidence that a SRPA with heave plate exhibits nonlinear relationships with motion parameters including relative position, velocity and acceleration. These parameters show causal relationships with the hydrodynamic force. A simulation methodology to establish confidence in the components of a model framework is developed and the hydrodynamic forces on SRPAs with heave plate and bulbous tank have been analyzed and compared. Two sets of numerical simulation were conducted. Firstly, the WECs were restricted to all degrees of freedom and subjected to monochromatic waves and later the WECs were oscillated at various frequency in a quiescent numerical tank. These results were validated against existing experimental data.

Earlier attempts by other authors to develop a data-driven model were limited to simple hulls and did not include rate dependent nonlinearities that develop for heave plates. These studies laid the foundation to current work. The model framework developed in this thesis accounts for the nonlinear relationship between force and parameters like velocity and acceleration along with hysteretic relationship between force and velocity. This modelling framework has a nonlinear static, a hysteresis (Bouc-Wen model) and a dynamic (ARX model) block. In this work the Bouc-Wen model is employed to model the hysteresis effect. Five different models developed from this modelling framework are analyzed; two are state dependent models, while the other three required training to identify dynamic order of model equations. These latter models (Hammerstein, rate dependent Hammerstein and rate dependent KGP models) have been trained and validated for various cases of fixed and oscillating HP cylinder. The results demonstrate significant improvement (max 39%) in prediction accuracy of hydrodynamic forces on a WEC with heave plate, for the model in which a rate dependent hysteresis block is coupled with Hammerstein or KGP models.

Contents

Supervisory Committee ii

Abstract iii

Table of Contents v

List of Tables viii

List of Figures ix

Acknowledgements xiii

Dedication xiv

1 Introduction 1

1.1 Background 2
1.2 Categorization of hydrodynamic models 5
1.3 Objectives and contributions 6
1.4 Organization of thesis 7

2 Hydrodynamic modelling of wave energy converters 9

2.1 Background 9
2.1.1 Wave Energy Converters 10
2.1.2 Potential flow (inviscid) approaches 12
2.1.3 Augmented potential flow approaches 13
2.1.4 Computational fluid dynamics 15
2.2 Numerical wave tanks 18
2.2.1 Governing equations 19
2.2.2 Turbulence modelling 20
2.2.3 Volume of fluid 21

2.2.4 Relaxation zone . . . 21
2.2.5 Arbitrary mesh interface . . . 22
2.2.6 Discretization schemes . . . 24
2.3 Validation of NWT in diffraction and radiation framework . . . 25
2.3.1 Domain and grid details . . . 26
2.3.2 Diffraction tests . . . 28
2.3.3 Radiation tests . . . 30
2.4 NWT results for radiation test on WEC B . . . 34
2.5 Summary and discussion . . . 36

3 Data-driven hydrodynamic modelling of WECs 39
3.1 System identification for hydrodynamic application . . . 40
3.1.1 Overview and classification . . . 40
3.1.2 Steps in system identification . . . 41
3.2 Input data . . . 42
3.2.1 Choice of model input . . . 43
3.2.2 Design of experiments . . . 43
3.2.3 Choice of excitation signal . . . 45
3.3 Block Oriented Models (BOM) . . . 46
3.3.1 Hammerstein model . . . 46
3.3.2 Rate dependent Hammerstein model . . . 49
3.3.3 Rate dependent Kolmogorov-Gabor polynimial model . . . 49
3.4 Blocks of BOM . . . 52
3.4.1 Static block . . . 53
3.4.2 Rate dependent block . . . 54
3.4.3 Dynamic block . . . 55
3.5 Parameter identification . . . 56
3.5.1 Error metric . . . 57
3.5.2 Static block identification . . . 58
3.5.3 Rate dependent block identification . . . 60
3.5.4 Dynamic block identification . . . 64
3.6 Model Validation . . . 69
3.7 Summary of the various candidate Data-driven models. . . . 71

4 Numerical wave tank trials 72

4.1 NWT trials for data generation 72
4.1.1 Spar geometry and CFD domain details 74
4.1.2 Grid sensitivity analysis 76
4.1.3 Input signal characteristics (Sea state) 78
4.2 Hydrostatic NWT Trail 80
4.3 Hydrodynamic NWT Trail 81
4.4 Characteristics of the 2D WEC Fluid Structure Interaction 84

5 Identification of data driven models for Heave Plate (HP) Spar geometry in irregular waves 87
5.1 Overview 87
5.2 Static block identification 89
5.3 Rate dependent block identification 90
5.4 Dynamic block identification 93
5.4.1 Choice of Range 1 model order and time delay 94
5.4.2 Choice of Range 2 model order 95
5.4.3 Choice of Range 2 time delay 96
5.4.4 Results of dynamic block identification 98
5.5 Validation 105

6 Summary and conclusions 115
6.1 Summary 115
6.2 Conclusions 116
6.3 Limitations 118
6.4 Future work 118

Bibliography 121

A Numerical tank verification study 134
A.1 Parameters for sensitivity analysis 134
A.2 Metrics for sensitivity analysis 135
A.3 Grid independence study-3D Mesh 136

B Hydrodynamic forces on WEC B 139

C Dynamic order and delay constants 144

List of Tables

Table 3.1 Summary of input and output of each block 71

Table 4.1 Characteristics of various NWT simulations used for data generation 73
Table 4.2 Grid independence study on 2D NWT 77
Table 4.3 Relative error $\epsilon_{\bar{H}}$ between target and resulting wave height $\pm$ standard deviation 78
Table 4.4 Characteristics NWT trials of various test cases used for data generation 83

Table 5.1 Summary of identification procedure, identified parameters, input variables required and composition of internal signal 88
Table 5.2 Values of parameters of Bouc-Wen equation, obtained from PSO for $R2$ 93
Table 5.3 Ranges analyzed for various data-driven model and test cases . . 99
Table 5.4 Optimal values of n_a, n_b and n_d for HP cylinder oscillating at $amp = 0.25\ m$ and $\omega = 1.25\ rad/s$ for realization $R1$ 101
Table 5.5 Optimal values of n_a, n_b and n_d for HP cylinder oscillating at $amp = 0.15\ m$ and $\omega = 1.25\ rad/s$ for realization $R1$ 104
Table 5.6 Optimal values of n_a, n_b and n_d HP cylinder oscillating at $amp = 0.05\ m$ and $\omega = 1.25\ rad/s$ for realization $R1$ 104
Table 5.7 Optimal values of n_a, n_b and n_d fixed HP cylinder for realization $R1$ 105
Table 5.8 Optimal values of n_a, n_b and n_d for fixed square cylinder and HP cylinder 106
Table 5.9 Error metric for all the cases of HP cylinder oscillation 109
Table 5.10 Approximate clock time required in each step 114

List of Figures

Figure 1.1 Schematics of the two WEC model configurations 3
Figure 1.2 Schematics of the floating point absorber-miniWEC 3

Figure 2.1 Schematics of four spar hulls analyzed by Yeung and Jiang (2011) 14
Figure 2.2 2D plane visualization of the structure of mesh for WEC A . . 23
Figure 2.3 2D plane view of a 3D mesh and domain for diffraction test . 26
Figure 2.4 2D plane view showing the position of spar relative to float over 1 time period 27
Figure 2.5 Normalized diffraction force magnitude (f_d/η) for WEC A, WEC B and Float 30
Figure 2.6 Variation of hydrodynamic force on oscillating spar for $A = 0.04$ m, r is the correlation coefficient. The x-axis is nondimensionalized over time period of oscillation. 33
Figure 2.7 Hydrodynamic forces on WEC B oscillating at amplitudes of 0.03 m, 0.04 m and 0.06 m. The x-axis is non-dimensionalized over time period of oscillation 36
Figure 2.8 CFD calculated hydrodynamic force on WEC with heave plate oscillating with an amplitude of 0.08 m 38

Figure 3.1 Working principle of system identification 41
Figure 3.2 Block diagram representing sequence of steps in system identification 42
Figure 3.3 Block diagram representing Hammerstein model 47
Figure 3.4 Block diagram of modified nonlinear system identification model with rate dependent block (*i.e.* Bouc-Wen model) 50
Figure 3.5 Possible scenarios in system identification describing causality, blocks represent discrete time steps 56
Figure 3.6 Process diagram representing difference between prediction and simulation 70

Figure 4.1 Classification of experiments for data generation. The input and output of these experiments are tabulated in Table 4.1 . . 73
Figure 4.2 Schematics of 2D prismatic test geometries: a square cylinder and a Heave Plate (HP) cylinder 74
Figure 4.3 Domain dimensions and mesh for NWT trials 75
Figure 4.4 Schematic of mesh sizes used in the sensitivity study 76
Figure 4.5 Distribution of characteristics of input signal for $H_s = 0.5\ m$ and $T_p = 10\ s$ 79
Figure 4.6 Variation of hydrostatic force with relative height 80
Figure 4.7 Variation of free surface height and relative Height for $R2$ . . 82
Figure 4.8 Flow field around HP cylinder oscillating at 0.25 m and 1.25 rad/s 86

Figure 5.1 Time series of excitation force f_{Ee} on oscillating HP cylinder . 91
Figure 5.2 Excitation force on oscillating HP cylinder ($amp = 0.05\ m$) for realization $R1$ with relative position and velocity 92
Figure 5.3 Amplitude spectrum of hydrodynamic force for realization $R1$ 96
Figure 5.4 Amplitude spectrum of internal force for realization $R1$ 97
Figure 5.5 NRMSE for fixed square cylinder for Range 1 100
Figure 5.6 NRMSE Vs n_a for HP cylinder oscillating at $amp = 0.25\ m$ for realization $R1$ and Range 1 and Range 2 using Hammerstein model 102
Figure 5.7 NRMSE for HP cylinder oscillating at $amp = 0.25\ m$ for realization $R1$ and Range 2 103
Figure 5.8 Comparison of amplitude spectrum of hydrodynamic force on square cylinder from CFD experiment and that estimated from Hammerstein model for training data-Range 1 (MAPE= 1.4×-2) 106
Figure 5.9 Comparision of CFD generated hydrodynamic force and Hammerstein model pridictions on fixed square and HP cylinder . 107
Figure 5.10 Hydrodynamic force on HP cylinder (Training data-Range 1) . 111
Figure 5.11 Hydrodynamic force on HP cylinder (Training data-Range 2) . 112
Figure 5.12 Hydrodynamic force on HP cylinder (Training data-Range 1) . 113

Figure A.1 Convergence of force on spar for different grid densities. M stands for millions of cells 137

Figure B.1 Comparison between CFD and experimental results of hydrodynamic force values on WEC B oscillating at $\omega = 4.04\ rad/s$ 139
Figure B.2 Comparison between CFD and experimental results of hydrodynamic force values on WEC B oscillating at $\omega = 3.72\ rad/s$ 140
Figure B.3 Comparison between CFD and experimental results of hydrodynamic force values on WEC B oscillating at $\omega = 3.47\ rad/s$ 140
Figure B.4 Comparison between CFD and experimental results of hydrodynamic force values on WEC B oscillating at $\omega = 3.15\ rad/s$ 141
Figure B.5 Comparison between CFD and experimental results of hydrodynamic force values on WEC B oscillating at $\omega = 2.90\ rad/s$ 141
Figure B.6 Comparison between CFD and experimental results of hydrodynamic force values on WEC B oscillating at $\omega = 2.65\ rad/s$ 142
Figure B.7 Comparison between CFD and experimental results of hydrodynamic force values on WEC B oscillating at $\omega = 2.34\ rad/s$ 142
Figure B.8 Comparison between CFD and experimental results of hydrodynamic force values on WEC B oscillating at $\omega = 2.08\ rad/s$ 143
Figure B.9 Comparison between CFD and experimental results of hydrodynamic force values on WEC B oscillating at $\omega = 1.77\ rad/s$ 143

Figure C.1 NRMSE for HP cylinder oscillating at $amp = 0.25\ m$ for realization $R1$ and Range 1 145
Figure C.2 NRMSE for HP cylinder oscillating at $amp = 0.15\ m$ for realization $R1$ and Range 1 146
Figure C.3 NRMSE for HP cylinder oscillating at $amp = 0.15\ m$ for realization $R1$ and Range 2 147

Figure C.4 NRMSE for HP cylinder oscillating at $amp = 0.05\ m$ for realization $R1$ and Range 1 148
Figure C.5 NRMSE for fixed HP cylinder for realization $R1$ and Range 1 149

ACKNOWLEDGEMENTS

A fellowship with supervisors is what nurture's an idea into a treatise. I start with an expression of gratitude toward Drs. Bradley J. Buckham and Curran Crawford. I have always looked for wisdom in the aphorism and knowledge in the cogent disquisition. Equally indelible is the involvement of Dr. Peter Oshkai. The originality of their ideas have inculcated maturity in the thesis and the individual. I am also sincerely appreciative for the insightful feedback provided by committee members Late Dr. Martial Agueh and Dr. Richard Dewey.

Also, I would like to thank the Natural Sciences and Engineering Research Council of Canada (NSERC) and Mitacs for their financial support and Compute Canada for the computational resources throughout this research.

I thank my friends and colleagues at the SSDL, WCWI, PRIMed and IESVic. I am thankful to Dr. Ilamparithi Thirumarai Chelvan and Ravi Krishna Chaitanya for sharing your thoughts and challenging mine, to Helen Bailey, Kush Bubbar, Scott J Beatty and Shahab Yeylaghi for the exciting discussions we had, to Juan P Ortiz and Meysam Karimi for pushing me when required, to Premkumar Govindappa for your good stories and Prashant Pednekar and Archana Pednekar for having an open ear to my niggles.

Parents do owe a special mention for their indubitable belief and prayers. Your love and wisdom has guided me through the tumult of life leading to culmination of this thesis. I am in-dept to my brother Ritwick Mishra, for upholding all these years what should have been my *Dhárma*.

This thesis is a synopsis of an ardent affair; and the one who without any trepidation left the cocoon of homeland with me to see the greyest as well as the most scintillating days has to be thanked with pious of words. Thanks to my lovely wife Richa Mishra for everything. And thanks to my daughter Vŕtti for understanding why *Pitaji* is at school when he should be at the park. Hopes and prayers that just like the meaning of your name life will come full circle one day.

Gratitude and prayers to *Pitŕ* and *Matŕ* (Ancestors) and *Brahman* for providing me every opportunity leading to this thesis.

Virag Mishra

DEDICATION

To Late Shri Kishore Kumar Sharma

Chapter 1

Introduction

Wave Energy Converters (WECs) are mechanical devices that harvest energy from the surface of ocean by virtue of interaction between waves and the device itself. Wave energy converters have yet to converge on a standard design and operating principle, and the different types are classified based external shape, operating principle, direction of motion *etc*. Point absorbers are devices that have small dimensions compared to the wavelengths of incident waves and are activated by hydrodynamic forces distributed over the WEC hull. To complete energy conversion, forces created by the interaction of the wave and the hull must be transferred to a Power Take Off (PTO). When the PTO is located between two floating bodies, it is called a *self-reacting* system and this category of WECs is called the Self Reacting Point Absorber (SRPA). SPRAs exploit the dynamic and hydrodynamic properties of moving bodies to absorb and convert ocean wave energy into useful forms. In this thesis a new technique is developed to predict the hydrodynamic forces on WECs, in typical operating conditions through numerical modelling.

Numerical modelling for wave energy conversion can be classified under two categories based on the underlying assumptions namely, linear and nonlinear. Linear models are based on the assumption of small waves, inviscid and incompressible fluid and small body movements. In linear modelling, principle of superposition is also applied. These simplifications lead to errors which successively add up and evidently render the model inaccurate. A mathematical model is required which could reduce the errors associated with superposition of forces from different experiments and be able to capture the important nonlinearities. The above requirements suggest that data driven meta-models (black box), or a combination of data and physics based modelling (grey box) could be a good alternative. When these models are used the

complexity of the physical system of fluid-body interaction is captured using limited experiments and the data thus generated can be used to train the model to operate in various realizations of input conditions. The numerical technique developed in this thesis for hydrodynamic analysis of WECs is a combination of data and physics based model.

1.1 Background

Heave plates as shown in Figure 1.1 and Figure 1.2, have become a critical component of many ocean structures and SRPAs design. Therefore interest in the evaluation of hydrodynamic behaviour of SRPAs with heave plates has increased (Cong and Teng, 2019). The primary purpose of a heave plate in offshore platforms is to mitigate the heaving motion (Lake et al., 1999; Li et al., 2013). In point absorber wave energy converters, heave plates are employed at depth below free-surface as relatively stationary bodies against which the Power Take Off (PTO) can stroke (Beatty et al., 2013). It is the fluid inertia that reduces the response of heave plate to the reaction force of PTO. In the vicinity of the plate, due to large diameter to thickness ratio of the plate and directional asymmetry, the flow field is also asymmetrical, rotational (vortical), and transient under the action of irregular waves (Brown et al., 2017). It is due to these fluid phenomenona that the models of SRPA hydrodynamics based on potential theory fail to accurately predict the hydrodynamic forces on these WECs (Beatty et al., 2015).

Mathematical models are crucial, for example, for power production assessment, simulation of device motions and model-based control strategies. Models based on potential theory variegate in their degree of nonlinearity, yet all suffer from limitation of fundamental assumptions of inviscid fluid, irrotational flow, small waves, small body motion and superposition. Fully nonlinear CFD models are able to describe the full range of hydrodynamic effects, but are computationally very expensive to assess a physically down-scaled tank test situation, let alone a simulation of a full scale commercial operation (perhaps including multiple SRPAs in a farm arrangement). For example, perform a simulation of WEC motion under realistic ocean conditions in 3D space it would require a dedicated $\$500,000-1$M CPU cluster and that cluster would be obsolete in $5-10$ years. However, by developing a system identification modelling technique the simulation and testing time can be reduced drastically and the model prediction can be performed on a home computer. This methedology

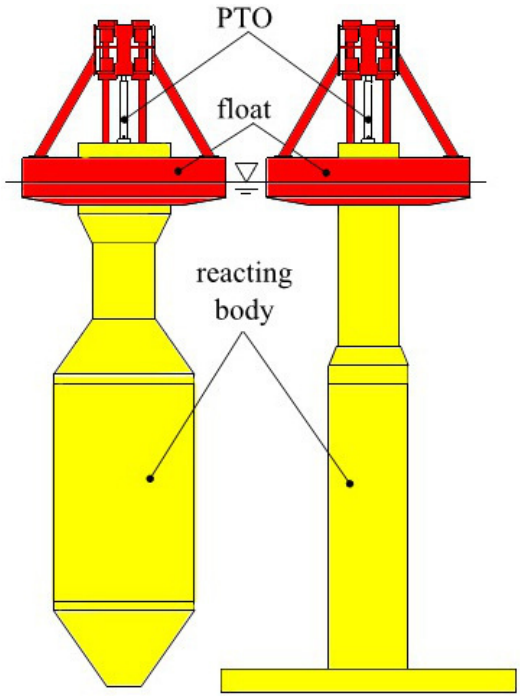

Figure 1.1: Schematics of the two WEC model configurations analysed in Chapter 2 — WEC A (left) features a bulbous tank and WEC B (right) features a large heave plate. Both WECs have identical float shapes, drafts, PTOs, and instrumentation systems. (From (Beatty et al., 2015))

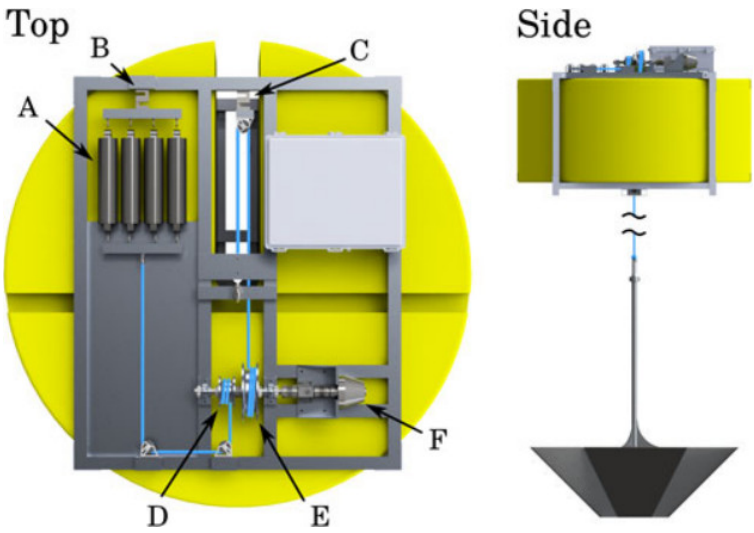

Figure 1.2: The spar with heave plate uses the rotation of a spring loaded spindle to produce power. The labeled components are A) the extension springs, B) the spring load cell, C) the heave plate tether load cell, D) the spring spindle, E) The tether load cell, and F) the rotary dashpot. (From Brown et al. (2017))

will provide a foundation for development of machine learning algorithms for online application of PTO controls during operation of WEC.

In a problem which involves flow of fluids, conservation of mass and momentum across discritized domains provides accurate accounting of energy dissipation. Discretization of fluid domain into finite volumes to solve fluid flow problems is known as Finite Volume Method (FVM) based CFD, and is one of many popular numerical modelling techniques. The accuracy of finite volume based CFD models are negatively impacted by weaknesses in the techniques for meshing the interfaces of the water, air and SRPA hulls. Most WECs involve relative motion between components. The challenges and expertise associated in maintaining the required quality of mesh for successful application either results in excessive computational overhead or inaccurate solutions.

Other physics based numerical approaches like nonlinear potential theory models or Smooth Particle Hydrodynamics (SPH) with characteristics between the CFD and potential theory extremes are limited to simple geometries which do not represent the diversity of WEC designs. Another limitation of SPH is the requirement of fixed number of water particles and enclosed simulation domains, implying necessity of large numerical tanks hence excessive computational resource.

Several modeling techniques including data driven techniques have been developed in the past and can be classified based on accuracy and computational speed. The models whose structure is completely derived on first-principles understanding of the system, even if some parameters are estimated from data are known as white box models. For example several parameters in turbulence modelling are tuned to case specific data still Direct numerical simulation (DNS), Large eddy simulation (LES), Detached Eddy Simulation (DES), Reynolds Averaged Navier-Stokes (RANS) along with other formulations based on Navier-Stokes can be categorized as white box models. Black-box models map input and output behaviour of a system without any specific physics based insights being used to chapter the connections between those inputs and outputs. Both the model structure and parameters are determined from experimental modelling. Black box models might even open up the range of inputs considered since they don't use physical principles to dictate what the relevant input-output relationships are. While white-box models can supply useful insights into the various factors that influence the behavior of a system, black-box models can be more straightforward to produce and sometimes provide a more accurate model.

Grey box models do not follow a first-principles approach, but are based on some

physical understanding. The shades of grey are determined by the extent of first principles understanding and dependency of data required (Nelles, 2001). The grey box models for hydrodynamic applications can be based on potential theory formulation or nonlinear CFD. The models that solve the linear decomposition of hydrodynamic problem into combination of radiation and diffraction phenomenon (Cummins, 1962; Falnes, 2007) and potential flow based models with varying degree of non linearity, (Babarit et al., 2012; Babarit, 2015; Bhinder et al., 2015) are examples of grey box model. Morison's approach (Morison et al., 1950) of modelling viscous flow to identify real world fluid behaviour around cylinders can be classified as white box model, but the models developed by abstracting this idea to model flow around other geometries can be refereed as grey box models.

1.2 Categorization of hydrodynamic models

For WEC applications, several model structures have been categorized and analyzed in literature (Giorgi et al., 2016b). A brief description of the classification relevant for the selection of model structure developed in this thesis is provided below.

Continuous/discrete time When the mathematical expression describing the system assumes infinite number of points between any two time values the model is a continuous time model. An advantage of CT models is that they provide a good insight into system understanding, because the model parameters are strongly related to the physical system properties. When difference equation rather than a differential equation is used to describe a system at discrete intervals, the model is called discrete time model. In this thesis Reynolds Averaged Navier-Stokes equations are used to generate the inputs for the model and the data driven model that is developed are based on discrete time approach. Discrete time modelling uses signals only specified at the discrete time instants $t = kT_s$, where k is integer and T_s is sampling period.

Causal/noncausal A system is causal if the output at current instant depends only on the present and past input where as in a noncausal system the output at current instant depends on the future input (Falnes, 2007).

Linear/nonlinear input-output relationship If the constants of equation are responsible for describing a linear relationship between input and output of the

mathematical model, it can be classified as linear. For example a spring-mass system with a constant spring coefficient shows a linear input-output relationship between the restoring force and displacement, whereas the drag coefficient in viscous fluid problems shows a quadratic relation between velocity and drag force. (Refer Section 3.4.1 for more explanation on this classification and its application to this thesis).

Static/dynamic A model in which the output depends on the instantaneous value of input rather than previous or future input values is a static model. Where as in a dynamic model the memory effects are accounted by sweeping over the past or future time instants. In other words, in dynamic models current value of an output can be dependent on the range of inputs seen over a previous time period as well as on the range of outputs seen over that same time period. In this thesis a dynamic model is considered over the simplicity of static model.

A mathematical model is required to model WECs with heave plate designs, which exploits accuracy of nonlinear CFD simulation but not its tardiness for industrial application. The objective of this thesis is find a balance between the physics based modelling approaches (use of representative differential equations) and data from previous tests (used of parameter identification).

1.3 Objectives and contributions

The overall objective of this research is to develop a data-driven grey box modelling approach suitable for model based performance assessment and simulation of heaving SRPAs with heave plates. The developed modeling approach would be similarly applicable to other wave-body interactions where significant viscous-driven separation hydrodynamic phenomena are present. More specific objectives are itemized as below.

1. **Objective** A data-driven mathematical model for accurate evaluation of hydrodynamic forces on SRPAs with heave plates is required to describe a broader range of WECs.

   Contribution A framework for development of high-fidelity data-driven numerical models, that accurately estimate the hydrodynamic forces acting on a SRPAs with heave plate is proposed in this thesis. A CFD based wave tank is used to generate inputs for data-driven models. Performance of five different

models including two proposed models based on the framework are validated with a SRPA design with heave plate. The integration of model component to model the fluid hysteretic effects into existing models, and its application to wave energy conversions are the novel contributions of this thesis.

2. **Objective** Establishing confidence in numerical methods for data generation methodology is another objective of this thesis. To avoid the need for physical experimentation to provide the data sets on which the new data driven approach must be built, a technique for modeling SRPA heaving motions in CFD is implemented and results compared against data produced in published physical experiments.

   Contribution A methodology for estimation of hydrodynamic forces is presented to validate the data generated by NWT. This methodology includes viscosity which is neglected in potential theory calculations. The NWT results are validated for two SRPA designs using 3D geometries. After validation with physical tank results for two different SPRAs, a solution methodology is developed using NWT trials for the purpose of data generation for the data-driven models.

3. **Objective** An objective of the thesis is to demonstrate a solution approach for transient simulation of a 3D body fitted mesh, which would capture the dynamics of multibody WEC.
   Contribution The hydrodynamic analysis of WECs is primarily dependent on the ability to simulate its dynamic motion. As multiple WEC configurations utilize the concept of harnessing energy by relative motion between different components, the challenge associated with designing a WEC, is simulation of multi-body motions using appropriate boundary conditions and capturing the interaction between these bodies. Though recent development in overset mesh motion can be an expensive alternative, a methodology is developed in this work for heaving multibody motion by simulating relative motion between float and spar for two SRPAs.

1.4 Organization of thesis

This section provides a map of the dissertation. Each chapter is provided with a dedicated literature review, as the nature of the subjects of the chapters is substantially

different. The thesis is sketched out in the following chapters:

Chapter 1 contains a statement of the key contributions which will be proved by this dissertation followed by an overview of the structure of the document itself.

Chapter 2 contains the literature review, details of governing equations and design of Numerical Wave Tank (NWT) experiments. The hydrodynamic forces were calculated using CFD tank experiments in classical framework. The performance of the SRPA designs, fixed and constrained to heave motion in regular waves are compared. This chapter also provides justification on the requirement of data driven models.

Chapter 3 contains introduction, literature review on data driven models. Along with the detailed description of models used in this thesis and the identification and parameter estimation process for various models.

Chapter 4 contains details related to the NWT trials involved in the data generation and discussion on the results, which reiterates on the required model architecture.

Chapter 5 demonstrates the implementation of modelling framework to using four different cases of fixed and oscillating SPAR designs with heave plate and one case of fixed square cylinder. Results of training and validation simulations for various cases of WECs in irregular sea is discussed and the performance of various data-driven models are compared.

Chapter 6 The thesis is concluded in Chapter 6 with summary and discussion on the contributions as well as recommendation on future work.

Appendices provide details of the physical and numerical models used, and supplementary information referred to in the main text.

Chapter 2

Hydrodynamic modelling of wave energy converters

In this chapter a review of physics driven modelling techniques classified as white box model in Chapter 1 is presented along with a review on various WEC and Numerical Wave Tank (NWT) designs. Two WECs which are distinct geometrically, and hence are expected to have a characteristically different power conversion are analyzed under different sets of conditions. One of the design features a bulbous tank and other features a large heave plate attached to the bottom of spar. The WECs are subjected to monochromatic waves, or oscillated with controlled heave motion. The objective of these experiments are to develop confidence on CFD generated results by comparing them with physical tank experimental results, before CFD can be used to generated data for data-driven models.

2.1 Background

Physics based modelling for wave energy conversion, can be broadly classified under two categories based on the underlying assumptions; namely inviscid and viscid modelling. Inviscid modelling can be further sub divided in linear and nonlinear modelling. It is extremely difficult to devise a generalized modelling approach, therefore this section tries to assimilate the diverse concepts into a few different groups and presents a review of existing models.

2.1.1 Wave Energy Converters

In the current section, the WEC design used in this chapter has been discussed and an attempt has been made to classify some of the WEC designs analyzed in literature along with a brief discussion on the modelling techniques used.

SRPAs, which are the WECs used for numerical analysis in this thesis, have been analysed numerically and also in a physical tank (Beatty et al., 2013, 2015, 2019). SRPAs typically employ a buoyant, surface piercing body referred to as the float which reacts against a second surface piercing body referred to as the reacting body, to generate mechanical energy. The WEC device in the current analysis is axisymetric, SRPAs primarily operating in heave mode as shown in Figure 1.1. It has a torus sliding along a vertical float and a hydraulic Power Take Off (PTO) system is driven by relative motion between the two bodies. Since this system does not need to react against the seabed, it can be installed in deep water. The key difference between these strategies is the shape of the reacting body. The first, denoted WEC A, is modeled after a WaveBob™(WaveBob Ltd., Ireland) device, featuring a positively buoyant float and a streamlined reacting body with an integral water ballast tank. The second, denoted WEC B, is modeled after a PowerBuoy (Ocean Power Technologies Inc, USA) device, featuring the same float as WEC A, but with a reacting body that has fitted with a large diameter heave plate. A $1:25^{th}$ scale model of a point absorber floating point WEC has been studied experimentally and numerical (Beatty et al., 2013, 2015) and the same models are studies in this chapter.

Heave plates are a critical component of many ocean structures and WECs. Therefore interest in the evaluation of their hydrodynamic behaviour has increased (Cong and Teng, 2019). The primary purpose of heave plate in offshore platforms is to mitigate the heaving motion (Lake et al., 1999; Li et al., 2013). In point absorber wave energy converters, heave plates are employed at depth below free-surface as relatively stationary bodies against which the Power Take Off (PTO) can stroke (Beatty et al., 2013). It is the inertia that reduces the response of heave plate to the reaction force of PTO. Due to large diameter to thickness ratio of the plate and directional asymmetry, the flow field is also asymmetrical, rotational (vortical), and transient under the action of irregular waves (Brown et al., 2017). It is due to these fluid phenomenona that the mathematical models based on potential theory fail to accurately predict the hydrodynamic forces on these WECs (Beatty et al., 2015).

In published studies on these WECs, it was concluded that parametrically excited

motions must be considered in more than one degree of freedom. Self-reacting devices, where coupling between different modes is important, are highly sensitive to the nonlinear coupling of heave, roll or pitch. It is clearly demonstrated in Tarrant and Meskell (2016) that the nonlinear heave, roll and pitch coupling occurs at large motion amplitudes and that the partially linear potential model is able to predict the parametric resonance, validating the model against experimental tests in a wave tank.

A set of power performance measures were estimated and the mean power absorption of eight WEC with different working principles were compared and a cost based analysis of WECs was done in Babarit et al. (2012). A similar classification, but based on capture width ratio was presented by the same author in Babarit (2015). Falcão (2010) suggests classifying WECs in three different groups based on oscillating flow field, oscillating body and over-topping. Based on the motion characteristics Penalba et al. (2017a) classified WECs into four different categories *viz.* oscillating wave converters, heaving point absorbers, oscillating pitch converters and oscillating surge converters. The WECs discussed in this thesis can be placed in the heaving point absorbers category.

Experimental analysis of the laboratory scaled model of the Wavestar which is a heaving WEC is done in Hansen et al. (2013). Wavestar is a semi-submerged hemispherical shaped WEC, oscillating around a pivot point. The limitations of using linear fluid structure assumption in analyzing this hull shape is shown in Zurkinden et al. (2014). The coupling of ocean structures can be defined either as one-way coupling or two-way coupling. A one-way coupling is when the flow-field is influenced by changing boundary shape, as in predefined rigid body motion. A more complicated case is a two way coupling like in ocean WEC, where the fluid forces effect the motion, as well as the radiation and diffraction due to the presence of the body alters the flow field. The importance of moorings have been identified by several authors like (Johanning et al., 2007) and (Fitzgerald, 2009). (Fitzgerald and Bergdahl, 2008) and (Garrett, 2005) mention that the design of moorings should be integrated with the dynamic analysis of WECs. The importance of moonpool region from wave energy production perspective has been highlighted in (Liu et al., 2020). Moonpool is the annular space in-between the spar and the float walls. It was concluded that compared with the single buoy and moonpool buoy, the moonpool can enhance the wave energy conversion in the frequency of 1.7–2.5 rad/s. When the wave period is short, the moonpool hinderd the motion of the cylinder buoy.

2.1.2 Potential flow (inviscid) approaches

Traditionally, the numerical analysis of ocean waves for engineering application have been based on the Stokes theory (Stokes, 1847), which assumes small amplitude waves, irrotational and invicid flows . This strategy helps in solving the problem using linear decomposition and the excitation and frequency response of the device can be constructed from the discrete frequency components. Several models for analysis of WECs are based on Cummins equation (Cummins, 1962). Cummins equation is used to evaluate fluid-body force corresponding to incident, diffracted and radiated waves in time domain. Frequency dependent addedmass and drag coefficients which are functions of single state variable (acceleration and velocity respectively) are used in mathematical models based on Cummins equation. Hence they do not take into account the effect of coupling between different state variables in realistic field conditions. However theories which were developed a couple of centuries ago helped in our understanding of the water wave mechanics and lead to the development of more relevant linear and non-linear theories as Boussinesq-type (Madsen, 1998) or statistical (Booij et al., 1999) modelling.

With a rise in the demand of oil and discovery of oil basins in deep oceans, the focus of ocean research in the 20^{th} century shifted to investigate the interaction of fixed and floating structures and thereafter design of ocean structures (Folley et al., 2004). Models based on potential flow theory integrate the pressure over the hull inorder to determine hydrodynamic forces, but because of invicid approximation it neglects the force due to form drag. Morison et al. (1950) proposed the idea of adding the drag force calculated using the drag coefficient into the force equation. Potential flow theory and the Morison's Equation which were the state of art are limited to simple geometries. These theories either employ the known results from flow around a vertical and horizontal cylinders or other exact techniques (Lewin, 1963; Mei, 1966).

With the use of computers direct calculation of transient problems using Green's functions (Shaw, 1975) and hybrid element method (Mei, 1978) for arbitrary geometries in simple harmonic waves became practical. Evans (1976) derived a general theory for the efficiency of wave absorption for a long cylinder of arbitrary cross-section oscillating in single or dual modes and later verified it experimentally in Evans et al. (1979). The same idea was extended to, two independently oscillating bodies in Srokosz and Evans (1979). In all the references presented above an *a priori* knowledge of added mass and damping coefficients for the body as a function of wave

frequency and amplitude was required in order to compute the response of the body.

These hydrodynamic coefficents have to be determined either by experimental measurment (Morison et al., 1950; Keulegan and Lloyd., 1958; Sarpkaya and Isaacson, 1981) or other numerical techniquies. Experimental determination of these coefficients is thus possible only for wave conditions reproducible in a wave tank. In order to numerically determine the hydrodynamic coefficients, Landweber and Macagno (1967) proposed to use a conformal mapping technique, which was revised and extended in Ramos and Guedes Soares (1997). The Frank Close fit approch (Frank, 1967) which is based on Green's function formulation has been widely used, even though it was found to calculate unreasonably high values of coefficients for some irregular frequencies. Even in recent times, coefficients are calculated using potential flow solvers and then used in time domain equations of motion (Beatty et al., 2013, 2015). Brown et al. (2017) calculated instantaneous values of these coefficients by utilizing least squares over the entire signal generated from experimental analysis of a WEC with damper plate. The details of the WEC used by Brown et al. (2017) for analysis is shown in Figure 1.2.

2.1.3 Augmented potential flow approaches

The time or frequency domain solution obtained with the assumption of small amplitude fails to represent complexities associated with both the turbulent sea state and the response of the device to the flow field. The non-linear dependence of heave forces on velocity for various Keulegan-Carpenter (KC) numbers was studied by Tao et al. (2000), who calculated the viscous damping forces on the Tension Leg Platform (TLP) column experiencing springing vibration. Evans et al. (1979) developed relations between these hydrodynamic coefficients for two bodies based on the results of single body by Newman (1976). Bonfiglio et al. (2011) performed prescribed harmonic oscillation experiments on a floating body to determine the hydrodynamic radiation coefficients of the body at numerous frequencies using a viscous solver. The coefficients are determined using velocity potential methods, and were compared with CFD determined values in a similar test setup. Potential solvers with viscous or nonlinear corrections for application in WEC analysis, have either used simplified geometries or simplified experiments (monochromatic wave field and single DOF motion) as previously mentioned in order to calculate parametric coefficients (Bhinder et al., 2015; Malenica et al., 1999; Bai et al., 2014; Penalba et al., 2017b). The time domain numer-

ical model used in Beatty et al. (2013, 2015) was based on potential theory which used drag coefficients from experimental results and added mass and damping coefficients derived from Boundary Element Method (BEM). The effect of viscosity on the heave added mass and damping coefficients for four cylinders with different bottom shapes using Free-Surface Random-Vortex Method (FSRVM) has been documented in Yeung and Jiang (2011). As shown in Figure 2.1, the bottom shapes are flat (BS), semi circular (SC), triangular (TC) and reversed-curvature (RC) which represented range of shapes from bluff to streamlined. The authors studied the effect of draft and bottom shape on the hydrodynamic coefficients. It was reported that increasing the draft increases its Response Amplitude Operator (RAO) and added mass but decreased its damping. It was also found that the damping largely increases with introduction of viscosity whereas added mass increases at lower frequencies but decreases at higher frequencies for all the bodies.

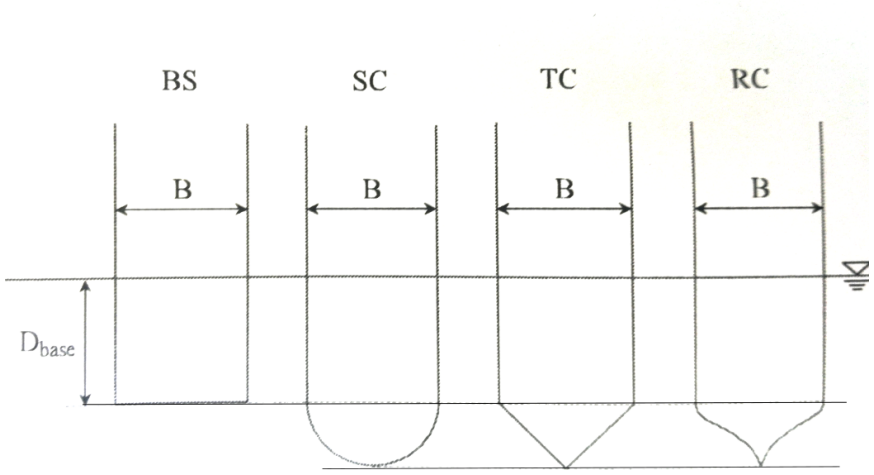

Figure 2.1: Schematics of four spar hulls analyzed by Yeung and Jiang (2011). The bottom shapes are flat (BS), semi circular (SC), triangular (TC) and reversed-curvature (RC). (From Yeung and Jiang (2011))

The simulation results of moored floating system was reviewed and validated with the tank test data of a moored horizontal cylinder subjected to monochromatic, bichromatic and pan chromatic waves in Roy et al. (2015). A methodology is proposed which introduces a non-linear hydro-static restoring moment in the WEC numerical model in Zurkinden et al. (2014)

2.1.4 Computational fluid dynamics

The solution obtained using models which assume small amplitude waves and/or small oscillation of WEC in irrotational and invicid flow, fails to represent complexities associated with both the turbulent sea state and the response of the device to the flow field. CFD simulations with realistic transient panchromatic input conditions are inclusive of all the fluid-body forces, and capable of including the nonlinear effects. CFD simulations capture all the complexity in the fluid domain with added computational cost. The reason for such computational cost is the ability of CFD models to predict velocity and pressure fluids at any point in the spacial or temporal domain. Such an extensive knowledge is very useful in wave energy production context as the final objective of CFD analysis for WEC design is calculation of the total force applied by the fluid on the body and the fluid-body interaction. Thus the body of CFD work in the literature can be broken down into generation and propagation of waves and fluid-WEC interactions.

CFD modelling of propagating monochromatic water waves over a submerged bar has been done by Morgan et al. (2011) in the open-source CFD library OpenFOAM (Weller et al., 1998). The problem of absorption of reflected waves from the outlet boundary was addressed by Jacobsen et al. (2012) where the authors extended OpenFOAM to include a generic wave generation and absorption method. Newly developed boundary conditions for wave generation and absorption using a piston type wave maker and active wave absorption was discussed in Higuera et al. (2013a). A companion paper (Higuera et al., 2013b) by the same authors discusses specific cases applied to coastal engineering by solving two phase free surface problems in a 3D domain. Under operating conditions a WEC is subject to different wave environments and the above papers provide an insight to boundary conditions used and their specification using OpenFOAM. Propagation and breaking of regular waves was modelled by Chenari et al. (2015). Extreme wave events were investigated by Vyzikas et al. (2013) by modelling a focused wave event, in an experimental wave tank and in an OpenFOAM Numerical Wave Tank (NWT). In a transient simulation good agreement between the two results were found initially, until unwanted wave reflections contaminated the experimental wave tank results. The wave reflection can be controlled by various active and passive methods (Windt et al., 2019). This highlights one of the advantages of the NWT approach for wave energy experiments.

Agamloh et al. (2008) used a 3D numerical flume to perform coupled fluid-

structure interaction simulation of a wave energy device in order to asses power output. The technique was also expanded to evaluate the interference between two buoys. By performing forced oscillation on simple 2D circular and rectangular cylinders using OpenFOAM, Bonfiglio et al. (2011) were able to measure the hydrodynamic forces on the body during radiation experiments and compare their values to those predicted by boundary element solvers. The above mentioned approach was repeated by Garrido-Mendoza et al. (2013) and Guedes and Santos (2014) to determine the added mass and radiation resistance coefficients of a floating body at discrete frequencies.

A two-dimensional OpenFOAM numerical wave tank was used to simulate non-linear wave-body interactions between monochromatic waves and a stationary surface piercing body in water of finite depth, with flat and sloping bottoms in Li and Lin (2010). A good agreement with experimental and numerical results of other researchers was found. This study was later extended by Li and Lin (2012) to include irregular waves and varying water depth. Chen et al. (2014) assessed how OpenFOAM performs when applied to non-linear wave interactions with offshore structures for a range of wave conditions.

Anbarsooz et al. (2014a) studied the behaviour of a submerged circular cylinder WEC subjected to highly nonlinear incident waves in a viscous numerical wave tank developed based on Navier-Stokes equation. In Anbarsooz et al. (2014b) a fast fictitious domain method to model a submerged wave energy converter subjected to nonlinear waves. In this method the solid objects in the domain are identified using a scalar parameter, and the momentum and continuity equations are solved in the entire domain including the solid object. The methedology presented in this work reduces the complexity of grid generation close to a solid object, apart from the fluid-solid two phase interaction. It was shown that the maximum efficiency of WEC occurs at larger damping coefficients and as the wave height increases it moves towards lower lower spring constants relative to calculations done from linear theory. The authors limited the applications of the described method to non-turbulent flow regimes and low amplitude steep waves. The details of wave generation techniques for both the above mentioned analysis are provided in Anbarsooz et al. (2013). The authors have used a piston type and a flap type wave-makers in intermediate and deep waters. It was found that for large wave steepness, the numerical and experimental wave heights are slightly lower than the analytical values. The solution was obtained using a control volume approach in conjunction with the fast-fictitious-domain-method for treating the solid objects. It was found that the wave-body interaction could not

be accurately predicted when turbulence dominated. Several other studies can be found in literature which attempted to include the non-linear viscous damping forces by directly solving Navier-Stokes equations (Tao et al., 2000; Agamloh et al., 2008; Afshar, 2010; Yeung and Jiang, 2011; Palm et al., 2013).

An exciting area of research is the simulation of Fluid Structure Interaction (FSI) in multiphase flows. A notable application in this topic area is the interaction of waves with ocean structures. Development in the numerical modelling of wave energy FSI can be attributed to the learnings in the field of naval hydrodynamics. The VOF technique of Hirt and Nichols (1981) and the immersed boundary formulation were combined in (Weymouth et al., 2006; Weymouth, 2008) to simulate ship hydrodynamics with overall first-order accuracy. Shen and Chan (2008) similarly applied the combined VOF and immersed boundary approach in several 2D case studies, including wave propagation over a submerged structure and wave generation by a moving bed. Paik (2010) incorporated the level set method (Osher and Sethian, 1988) into CFDShip-Iowa, a computational ship code developed at the University of Iowa based on RANS models. Sanders et al. (2011) conducted preliminary numerical study on the rigid-body motion in 2D incompressible two-phase flows, also by incorporating the level set formulation for the free surface representation. Thus some of the the capabilities in FSI that were particularly relevant to wave energy application are interaction of free surface flows with structures, dynamic meshing, green water, structural deformation *etc.*

In the context of two-body heaving SRPAs the simulation of fliud in the moonpool region is particularly challenging. Such FSI problems pose significant challenges to current numerical methods, as both the fluid-fluid interface and fluid-solid interface must be accurately computed to faithfully represent the important physics involved. Though recent development in overset meshing adds several capabilities in simulation of heaving motion of two closely placed annulus geometries. As of time of this research, it is believed that all the overset capabilities were at infancy when this work started and to this date these capabilities are only available commercially and are not present in the open source domain. Thus, few works have been conducted along this direction in ocean energy domain, and even fewer have considered the realistic interactions involving all the important aspects: fluid motion, structure movement and multiphase free-surface flow.

2.2 Numerical wave tanks

NWTs are a set of boundary conditions that can be applied to patches which replicate physical boundaries in physical wave tanks. This boundary conditions are used to perform wave generation or absorption and assign values of fluid parameters (velocity, pressure, viscosity, turbulence properties, fluid type *etc*) to finite volume cells. NWTs have been used for many years in ocean engineering to analyze fluid structure interaction. Numerical tanks not only provide an alternative to the expensive physical tank experiments but also give the flexibility of designing an experiment. Thus, it is important that the numerical tank uses high fidelity numerical models. The numerical tank in this study is based on the open-source CFD software OpenFOAM. OpenFOAM uses a finite-volume discretization technique that require a computational mesh which divides the spatial domain into discrete finite domains known as control volumes. The governing equations are solved for each finite control volume in the mesh, and the variables like velocity and pressure are solved and computed at the nodes and face centres respectively for a staggered grid. Sections 2.2.1-2.2.6 provides a background on the fundamentals of NWT utilized in this thesis and has been divided into several parts which briefly touch upon the governing equations of fluid flow, solid body motion, relaxation zone, volume of fluid, arbitrary mesh interface and various discretization schemes used.

Some of the important advantages of using a numerical wave tank for analysis are as below.

- Reflections from 'tank' walls can be effectively controlled
- Can test the device at full scale, eliminating scaling effects
- Free response tests can be implemented
- The device can be constrained to different modes of motion without requiring mechanical restraints, which can add friction and alter the device dynamics
- Hydrodynamic force measurement.
- Specialist equipment, including a prototype WEC device, is not required

However, NWTs are not without drawbacks. Some of the disadvantages are itemized as below.

- The chief disadvantage, over a conventional wave tank, is the excessively long time to perform the numerical computation. Thus it is a key part of any NWT assessment. The computational requirements can be quantified by the run time, t_r, normalised by the simulated time, t_s , and the normalised for run time per cell. The normalised for run time for most of the state of solver were found to be in the range $250 - 300$ as published in Windt et al. (2019).

- NWTs can take considerable experience to use well, in particular setting up a spatial mesh, which offers a reasonable compromise between computation time and accuracy.

- The pressure peaks, due to the impact between waves and the WEC, occur over short time scales; therefore, it is necessary to utilise small time steps, in order to accurately describe the pressure peaks, which increases the simulation time.

2.2.1 Governing equations

The Reynolds Averaged Navier-Stokes (RANS) equations are time-averaged equations of motion for fluid flow. These equations are derived by time averaging of the Navier-Stokes equations. For an unsteady, incompressible, turbulent flow the continuity equation Eq. (2.1) and the momentum equations Eq. (2.2) are:

$$\frac{\partial \overline{U_i}}{\partial x_i} = 0 \tag{2.1}$$

$$\rho\frac{\partial \overline{U_i}}{\partial t} + \rho\frac{\partial \overline{(U-U_g)_i}\,\overline{U_j}}{\partial x_j} = \rho g_i - \frac{\partial p}{\partial x_i} + \frac{\partial \tau_{ij}}{\partial x_j} + \mu\frac{\partial^2 \overline{U_i}}{\partial x_j^2} \tag{2.2}$$

where ρ is fluid density, x_i $(i = 1, 2, 3)$ represent x, y and z directions respectively, t is time, g_i $(i = 1, 2, 3)$ are the body force intensities in x, y and z directions respectively, p is pressure, $(U - U_g)_i$ $(i = 1, 2, 3)$ is the resultant velocity components in x, y and z directions respectively when the grid points have a velocity U_g in that direction, $\overline{U_j}$ $(i = 1, 2, 3)$ are the mean velocity components in x, y and z directions respectively and μ is dynamic viscosity of the fluid. In the above $\tau_{ij} = -\rho\overline{u_i' u_j'}$ represents the Reynolds stress components and u_i' $(i = 1, 2, 3)$ are the components of fluctuating velocity in x, y and z directions respectively. These equations cannot be solved directly as they no longer constitute a closed set and require additional equations in the form of turbulence models. In this study the realizable k-ε model (Shih et al., 1995) for turbulence

has been used. The aim of any turbulence model is to express the Reynolds stress in terms of known or calculable quantities. In Cartesian coordinates the components of the viscous stress tensor which represents additional momentum transfer due to turbulent fluctuations are defined based on the Boussinesq eddy viscosity hypothesis as:

$$\tau_{ij} = -\frac{2}{3}\rho k\delta_{ij} + \mu_t S_{ij} \tag{2.3}$$

$$S_{ij} = \frac{\partial \overline{U_i}}{\partial x_j} + \frac{\partial \overline{U_j}}{\partial x_i} \tag{2.4}$$

In the above δ_{ij} is Kronecker delta (= 1 when $i = j$, otherwise 0), k is the kinetic energy, μ_t is the turbulent viscosity and S_{ij} is the mean strain rate. As the Reynolds stresses are not known, appropriate turbulence models (realizable k-ε in current study) are introduced for calculating these stresses and their interaction with the mean flow variables. These models are called closure models. The additional viscosity due to turbulence of flow known as the turbulent viscosity μ_t is given by:

$$\mu_t = \rho C_\mu \frac{k^2}{\varepsilon} \tag{2.5}$$

where C_μ is calculated as follows for realizable k-ε model:

$$C_\mu = \frac{1}{A_0 + A_s k U^*/\varepsilon} \tag{2.6}$$

A_0 is a model constant (= 4.0), where as the parameter A_s is a function. Readers are directed to (Shih et al., 1995) for further curiosity on model parameters used in realizable k-ε turbulence models.

2.2.2 Turbulence modelling

In this study the realizable k-ε model (Shih et al., 1995) for turbulence has been used. This turbulence model belongs to the family of 2-equation eddy viscosity models and involves two transport equations, one for the kinetic energy (k) and other for the dissipation rate of the kinetic energy (ε). The transport equations for k and ε are:

$$\rho\frac{\partial k}{\partial t} + \rho\frac{\partial (kU_j)}{\partial x_j} = -\rho\overline{u_i' u_j'}\frac{\partial U_i}{\partial x_j} - \rho\varepsilon + \frac{\partial}{\partial x_j}\left[\left(\frac{\mu_t}{\sigma_k} + \mu\right)\frac{\partial k}{\partial x_j}\right] \tag{2.7}$$

$$\rho\frac{\partial\varepsilon}{\partial t}+\rho\frac{\partial(\varepsilon U_j)}{\partial x_j}=C_{\varepsilon 1}\frac{\varepsilon}{k}\rho\overline{u_i'u_j'}\frac{\partial U_i}{\partial x_j}-C_{\varepsilon 2}\rho\frac{\varepsilon^2}{k}+\frac{\partial}{\partial x_j}\left[\left(\frac{\mu_t}{\sigma_\varepsilon}+\mu\right)\frac{\partial\varepsilon}{\partial x_j}\right] \tag{2.8}$$

where $C_{\varepsilon 1}, C_{\varepsilon 2}$, are constants, σ_k and σ_ε are the turbulent Prandtl numbers for k and ε respectively. The values of the constants for realizable k-ε turbulence model are as follows: $C_{\varepsilon 1} = 1.44,\ C_{\varepsilon 2} = 1.9,\ \sigma_k = 1,\ \sigma_\varepsilon = 1.2$.

2.2.3 Volume of fluid

The multi-phase problem is addressed using the volume of fluid formulation, where an additional parameter known as the volume fraction (α) is used to represent the phase of the fluid in the finite volume cells. The free surface is tracked as $\alpha = 0$ represents the pure air phase while $\alpha = 1$ represents pure water phase and the interface is represented by the intermediate α values. The properties of the fluid are computed based on the volume fraction of the cell:

$$\phi = \alpha\phi_w + (1-\alpha)\phi_a \tag{2.9}$$

where ϕ is any fluid property like density (ρ) and viscosity (μ); while index w and a indicate water and air respectively. The diffusive property of the VoF method at the wave interface is suppressed by introducing an artificial compression term into the transport equation for the volume fraction as mentioned in (Rusche, 2002).

$$\frac{\partial\alpha}{\partial t}+\nabla.(\alpha(U-U_g)_i)+\nabla.(\alpha(1-\alpha)U_r)=0 \tag{2.10}$$

Eq. (2.10) is the transport equation for the volume fraction, where U_r is the velocity field suitable to compress the interface. The artificial compression term has an effect only at the interface region (Hemida, H., 2008).

2.2.4 Relaxation zone

The relaxation zones are implemented to avoid reflection of waves from the far field boundaries. The free surface is displaced from equilibrium due to generation of waves caused either by the heaving motion of the spar or its reflection from the float. The deformation of the free surface may propagate to the boundaries of the numerical tank and in turn be reflected to contaminate the near field of the WEC. The present relaxation technique was implemented in Jacobsen et al. (2012) and is based on Mayer et al. (1998).

A relaxation function (ξ_R) is calculated using Eq. 2.11 inside the relaxation zone

$$\xi_R(\chi_R) = 1 - \frac{\exp(\chi_R^{3.5} - 1)}{\exp(1) - 1} \tag{2.11}$$

The value of χ_R in the above equation should be between 0 and 1. The term χ_R is defined such that ξ_R should be 1 at the interface of relaxed and unrelaxed zone. The value of fluid velocity (U) or volume fraction (α), can be found out by substituting the value of ξ_R in the Eqs. 2.12 and 2.13 below,

$$U = \xi_R Uc + (1 - \xi_R)Ut \tag{2.12}$$

$$\alpha = \xi_R \alpha_c + (1 - \xi_R)\alpha_t \tag{2.13}$$

where index c and t indicate computed and target values respectively.

2.2.5 Arbitrary mesh interface

In the current work, two different finite volume domains surrounding the spar and the float have been considered. The governing equations for continuity, momentum, turbulence and rigid body motion are solved separately for each domain. The exchange of values of fluid properties takes place across the outer boundary of the inner domain and the inner boundary of outer domain using a conservative interpolation method by local Galerkin projection proposed in Farrell and Maddison (2011). This technique has been implemented in OpenFOAM and is known as an Arbitrary Mesh Interface (AMI). It enables simulation across disconnected, adjacent, mesh domains; where each face accepts contributions from partially overlapping faces of the neighbour patch. AMI weights define the contribution as a fraction of the intersecting areas. For each face, the sum of the weights should equal 1. Conservation errors are introduced as the sum of weights deviates from 1 where the patch geometries are not well matched. Though these errors are localized and do not cause the method to fail, users can specify a lower limit to the sum of weights. When the sum of weights goes below this limit, the interpolation across the AMI boundary cells stops and a Dirichlet boundary condition is imposed to particular patch faces.

The grid for the float and spar have been generated separately, yet care has been taken that the inner most extent of domain containing the float matches exactly with the outer most extent of the domain containing the spar. Initially the spar and

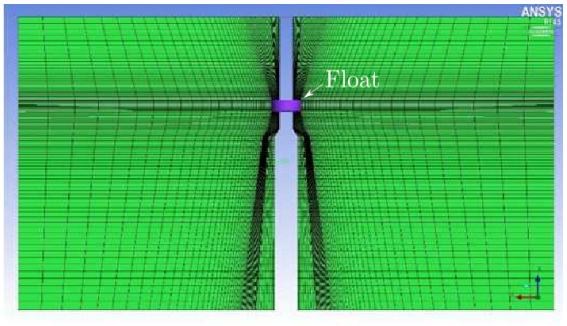

(a) View of the complete extent of mesh in the outer domain (Front view)

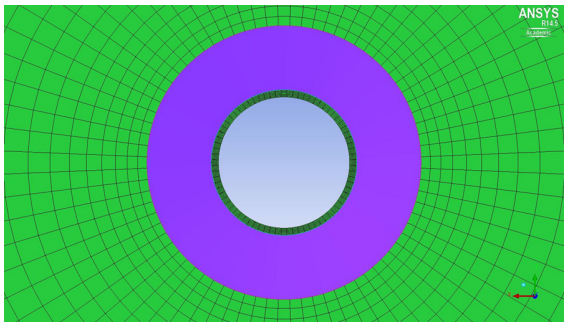

(b) View of the mesh close to float in the outer domain (Top view)

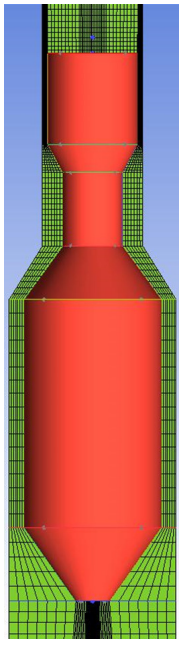

(c) View of the mesh in the inner domain (Front view)

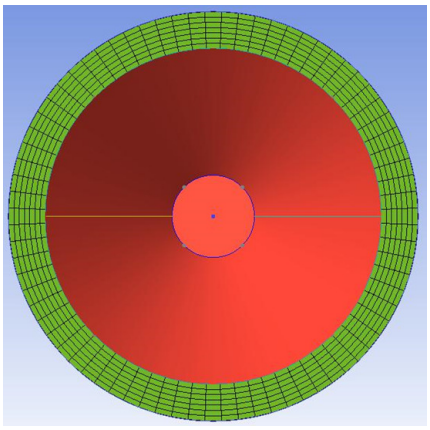

(d) View of the mesh in the inner domain (Bottom view)

Figure 2.2: 2D plane visualization of the structure of mesh in the outer and inner domain close to float and spar of WEC A.

float are placed at the centre of their respective CFD domains. Thus when both the domains are combined the central axis of the combined domain coincides with the central axis of each individual domain. The outer domain is shown in Figure 2.2a and Figure 2.2b and the inner domain in Figure 2.2c and Figure 2.2d. Perfectly overlapping boundaries at the mesh interface throughout the simulation would imply consistent spatial distribution of fluid properties, but it can be seen from Figure 2.2c that the interface close to the upper conical section of the WEC is also conical. Thus, with the current dynamic mesh algorithm maintaining overlapping interfaces throughout the simulation at the upper conical section is not possible. This is treated as a limitation in the current study and may be addressed in any future work.

2.2.6 Discretization schemes

The governing equations are solved at the center of the cells in a finite volume domain discretized into structured hexahedral cells. The discretisation scheme used for the Laplacian and gradient terms as $\nabla.(\mu\nabla U)$ is Gaussian integration (here after referred as Gauss) with linear interpolation of values from cell centres to face centres, and the interpolation scheme for the diffusion coefficient (μ) is linear (central differencing) with explicit surface normal gradient scheme which includes non-orthogonal correction. For the divergence terms the discretisation scheme used is Gauss and the interpolation schemes for velocity (U), turbulent kinetic energy (k) and dissipation of kinetic energy (ε) is first/second order, bounded. A first order, bounded implicit scheme is used for the first time derivative. The algorithm used for the resolution of the governing Equations 2.1 and 2.2 is based on the PIMPLE method which is a combination of the algorithms SIMPLE (Semi-Implicit Method for Pressure Linked Equations) and PISO (Pressure Implicit with Splitting of Operator). The SIMPLE algorithm (Patankar, 1980; Versteeg and Malalasekera, 2007) is used to solve steady-state problems with emphasis on the treatment of the non-linear effects of the velocity rather than the precise determination of the pressure field. Each iteration is assumed to be a pseudo time step. Stability is assured and convergence is improved by under-relaxation of fluid properties. The PISO algorithm (Marquez, 2013; Issa, 1986), is suitable for solving the velocity-pressure coupling for each time step in a transient simulations. The non-linear effects of the velocity are reduced by setting small time steps characterized by Courant numbers (Courant et al., 1967) below 1.

2.3 Validation of NWT in diffraction and radiation framework

The objective of CFD simulation in the classical framework of diffraction and radiation is to establish confidence in the quality of the numerical wave tank results. Data generated by NWT will be used for the data-driven models described in Chapter 3. The experiment design for data generation is discussed in Chapter 4. In these experiments the oscillating WECs are subjected to panchromatic wave inputs. In this chapter, results from a simplified setup of NWT is validated. The simplified experiments in NWT consists of diffraction and radiation. The results are validated against the experimental and numerical results in Beatty et al. (2015). In the published results, the Boundary Element Method (BEM) code WAMIT was used to calculate the nondimensionalized parameter, and two sets of physical tank experiments were performed. These experimets will be referred as diffraction experiment and radiation experiment. In the diffraction experiment, direct measurements were taken of the wave forces on the WEC bodies while held fixed in regular waves. In the radiation experiment, forced oscillation of spar induces WEC body motions in a quiescent tank. The hydrodynamic force on the components of WEC is recorded over the duration of experiment. Though the performance of BEM model was validated against different physical tank experiment conditions, it failed to simulate the complex flow phenomenon in the moon-pool region between the float and spar. A numerical moon-pool lid was introduced at the water surface in the annular gap between the float and reacting body. The moon pool lid mitigates erroneous BEM numerical solutions such as negative added mass and unrealistically high radiation damping in the fluid domain arising from resonant oscillations.

The methodology to simulate oscillating motion between two annulus geometries discussed in Section 2.2.5 is used to address this issue and will be one of the major contribution from the current thesis as mentioned in Section 1.3. The Finite Volume Method (FVM) code OpenFOAM is used to for comparison with experimental and WAMIT results. The finite volume mesh is shown in Figure 2.2, Figure 2.3 and Figure 2.4. The water depth in all the cases is 2.0 m. The spatial domain is assumed to have finite and infinite size (i.e. tank wall effects were neglected) for FVM and BEM calculations. A two-body analysis of each WEC configuration was performed in OpenFOAM, so that the hydrodynamic effects of float and reacting body were included in the presence of the other body. But the effect of float was not considered

in BEM and physical tank experiments.

2.3.1 Domain and grid details

Two different meshes were used to perform diffraction and radiation tests. The diffraction tests involves generation and absorption of waves a, therefore a cuboid shaped domain is used where as wave are not generated in radiation test therefore a cylindrical domain is used. The acceptable distance between the cell centroid and wall adjacent cells is usually measured in the wall unit y^+ as, and is given by the formula $y^+ = l_1 u_\tau / \nu$ where $u_\tau = \sqrt{\tau_w / \rho}$ is the friction velocity and τ_w is the wall shear stress. For the wall law to be applicable, the grid size should be adjusted such that $30 \leq y^+ \leq 300$, and the wall adjacent cells are not placed in the buffer layer of $y^+ = 5 \sim 30$. An excessively fine mesh has been avoided near the body surface when standard and nonlinear k-ε turbulence models are used.

The verification study of determining grid resolution and domain dimensions are presented in Appendix A. The grid resolution close to the freesurface are based on the Appendix A. A separate verification study for 3D tank is described in Section A.3.

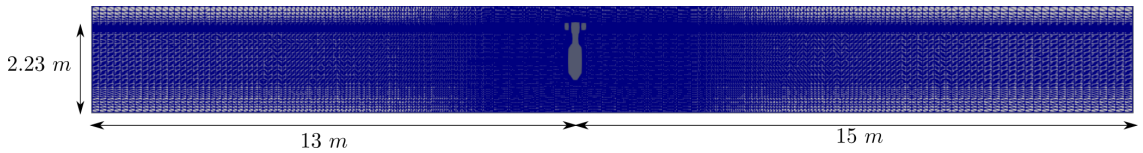

(a) Mesh for WEC A in xy plane

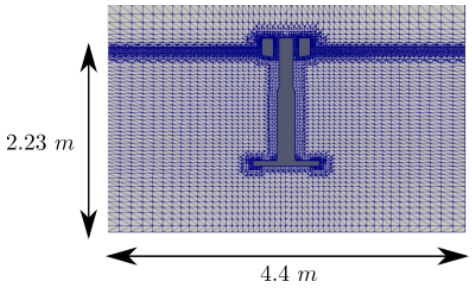

(b) Mesh for WEC B in yz plane

Figure 2.3: 2D plane view of a 3D mesh and domain for diffraction test

Diffraction tests

The domain dimensions and the associated structured mesh around the WEC is shown in Figure 2.3. For this test the spar is placed at 15 m from inlet and 13 m from outlet,

because wave modelling requires larger distance from inlet and outlet boundaries to allow wave generation and absorption. A generation zone and absorption zone is placed close to the inlet and outlet respectively according to the discussion in Section 2.2.4. Figure 2.3a shows the domain dimensions in xy plane when WEC A is in the NWT. Whereas, Figure 2.3b shows the mesh around WEC B in yz plane. In all the tests, numerical tank is 2.23 m deep and 4.4 m and the total number of finite volume cells in the domain were around 4 million.

Radiation tests

The outer and inner computational domain is contained in $r \in [0.176, 5.5]$ m and $r \in [0.0, 0.176]$ m respectively in the radial direction and the extent in the azimuthal direction for both the domains is $z \in [-3.21, 2.79]$ m. The draft is $z = 1.4$ m.

The structured hexahedral mesh extends to both the domains such that continuity of node points and gradient is maintained in the same domain and also across the AMI boundary. A narrow band of highly resolved mesh can be seen at the location of free surface to maintain a sharp air-water interface and suppress the diffusive nature of the VoF technique. It can bee seen from Figure 2.4 that when a heaving motion is imposed between the domains, the outer boundary of the inner domain also oscillates at the same frequency and amplitude as the spar.

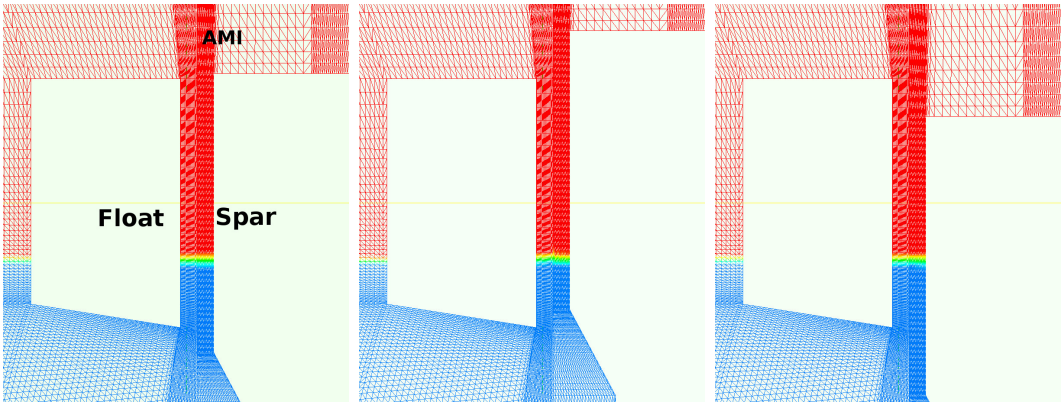

(a) $t = 0, T$ (b) $t \backsimeq \frac{T}{4}$ (c) $t \backsimeq \frac{3T}{4}$

Figure 2.4: 2D plane view showing the position of spar relative to float over 1 time period

Grids with varying degree of mesh resolution have been studied for their prediction of force values in the grid independence study. The total cell count for different grids are approximately $3-5$ million. The results of the grid independence study have been

discussed in Section A.3. In the previous study by Yu and Li (2013), the geometry was simplified to a locked single-body system in order to avoid mesh deformation in the moon-pool region. An important feature of this study is that the mesh deformation close to the float and spar has been avoided by use of AMI, hence the system is representative of actual WEC operation and the forces are expected to be calculated with accuracy.

2.3.2 Diffraction tests

The wave excitation forces in the heave direction on all bodies were measured in regular waves for frequencies in the range of $1.5 - 4\ rad/s$ and for wave heights of $0.04\ m$. Diffraction tests were executed for each body with the other body held fixed at its equilibrium position. The durations of experiments in NWT were limited to 20 time periods in this thesis to avoid longitudinal tank reflections as well as to attain steady state. 10 time period of wave oscillations were chosen for analysis between 1.5 to 4 rad/s. The physical tank experiment (Beatty et al., 2015) were conducted for 150 sec. In these experiments, the float and reacting body were held fixed, the heave forces and the water surface elevation were recorded. The excitation force magnitude and phase data were extracted from the force time series in following steps.

1. First, the force time series was split into non-periodic transient and periodic steady-state data.

2. The initial (physical wave tank and NWT data) and final transients (physical wave tank data) were discarded.

3. From the remaining data the force time series was split into windows of data, of duration 1 wave period, each containing an excitation force maximum and minimum.

4. Lastly, for each window, the diffraction force magnitude for physical wave tank experimental and numerical results were obtained. An ensemble averaging over one time period was done over the sample period.

The CFD, experimental and BEM derived diffraction forces, for WEC A, WEC B, and the float, are summarized by the frequency dependent diffraction force plots shown in Figure 2.5. WEC A features a bulbous tank and WEC B features a large heave plate. Both WECs have identical float shapes (refer Figure 1.1). A comparison

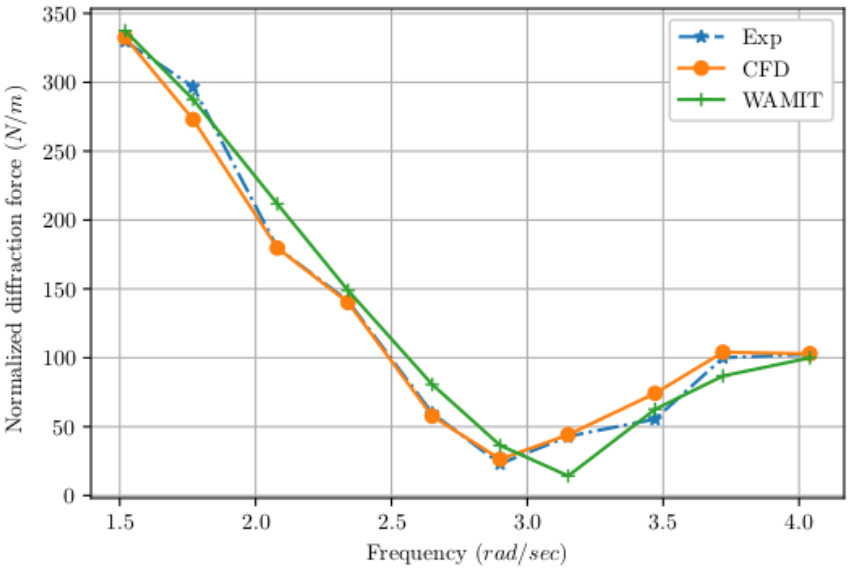

(a) Diffraction force on WEC A

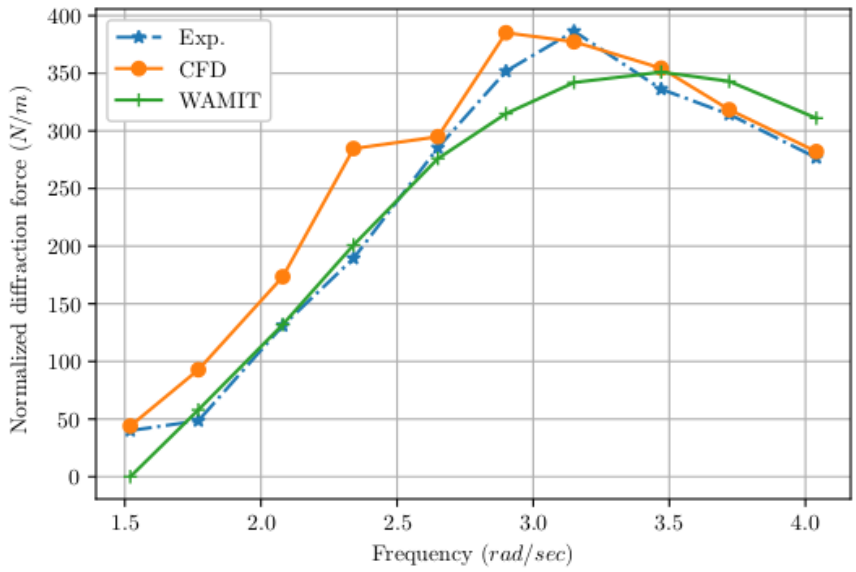

(b) Diffraction force on WEC B

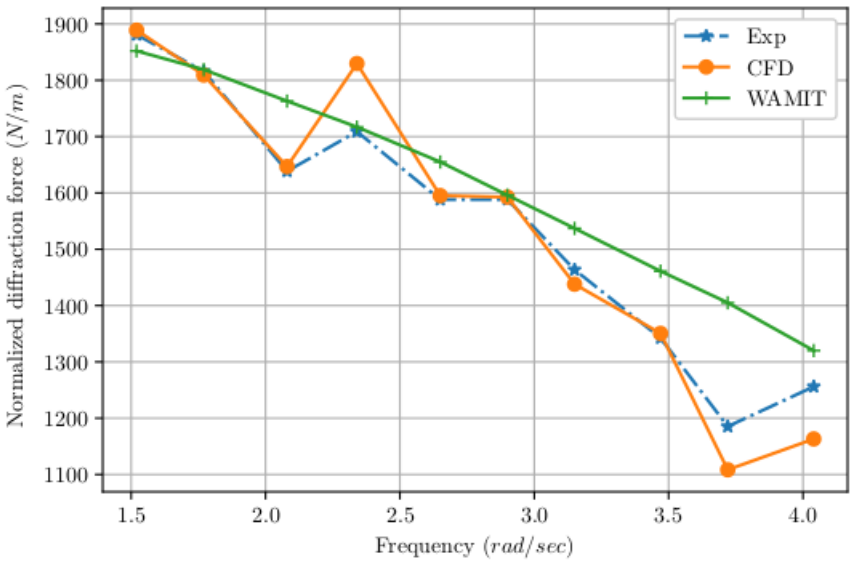

(c) Diffraction force on Float

Figure 2.5: Normalized diffraction force magnitude (f_d/η) for WEC A, WEC B and Float. The physical tank experiment and WAMIT results were processed and reproduced from the experiments done by Beatty et al. (2015)

.

of force time series for all the frequencies for WEC B and float is also presented in Figure B.9a to Figure B.1a in Appendix B.

Key observations to be made from Figure 2.5 are as follows. First, the numerical diffraction force data agrees well with the tank test data as well as BEM calculated values. The excitation force magnitude curves seen in Figures 2.5a, 2.5b and 2.5c, are normalized by wave amplitude, and are observed to collapse together. It should be noted that in setup in NWT the float was present with the spar whereas in physical wave tank or WAMIT results the float was not considered along with spars. This might have contributed to the difference what-so-ever between the values of diffraction forces. It is apparent therefore, that diffraction forces are well predicted by FEM and BEM analysis in most of the wave frequencies tested.

2.3.3 Radiation tests

The objective of the radiation tests was to establish the methedology to simulate motioin of two annulus geometries oscillating in heave and to see the influence of oscillating amplitude and frequency on the profile of hydrodynamic force. These tests comprised of forced heave only motions of WEC A and WEC B. WEC A features a

bulbous tank and WEC B features a large heave plate. Both WECs have identical float shapes (refer Figure 1.1).

WEC A

The hydrodynamic forces on a oscillating self-reacting point absorber wave energy converter WEC A is calculated using CFD. The component geometries of float and spar are enclosed in two different fluid domains, each subjected to relative motion using a dynamic mesh algorithm. The transfer of field variables across the domains is achieved through an Arbitrary Mesh Interface (AMI). This unique methodology avoids cell deformation close to the component parts of the WEC, thus eliminating the errors in force calculation due to deformed cells. The continuity and momentum equations along with the free surface are solved separately in each domain. The validation of radiation force calculated from CFD is done by the experimental results of Beatty et al. (2015).

In this section four cases are analysed for the forces acting on the WEC when the spar is oscillating at a constant frequency. The displacement profiles used as input in these cases were generated using a sine function $x(t) = A\sin(\omega t)$. Where A is the amplitude of oscillation of the spar, ω is the angular frequency and t is the instantaneous time. Four different cases with the amplitude $A = 0.04m$ but with different angular frequencies $\omega = 2.06,\ 2.61\ , 3.17$ and $3.99\ rad/s$ were used. The variation of hydrodynamic forces acting on the WEC as obtained from CFD were compared with the experimental results. The variation of forces for different cases are shown in Figure 2.6a, Figure 2.6b, Figure 2.6c and Figure 2.6d. The Pearson's coefficient of correlation between the CFD and experimental results are 0.99, 0.98, 0.99 and 0.99 respectively. The values of correlation coefficients were found to be close to a perfect correlation. However, it should be noted that the filtered values of experimental data were used for finding the coefficients. The comparison of values of hydrodynamic forces obtained from CFD and experiment are satisfactory for all the cases, though a negligible phase shift can be seen in all the cases. The coefficient reflect the correlation of the magnitude only and not of the phase of the profile. One of the possible reason for this shift may be the absence of float in the physical tank experiment another possible explanation can be the mapping of the interface near the upper conical region when the spar is not at the mean position, as mentioned in Section 2.2.5. It can also be seen that the discrepancy in peak force magnitude increases with frequency. The

possible reason for this discrepancy can be the poor resolution of the linear motor that was used as an actuator to control the displacement of the spar in the physical experiment. The close proximity of the tank bottom in experiments can be another possible contributor to this discrepancy. The distance between the spar and tank bottom is only 0.6 m at mean position in experiment, while the same is 2.71 m in CFD. The decision on the depth of numerical tank was taken to ensure minimum influence on the WEC hydrodynamics from the NWT tank bottom.

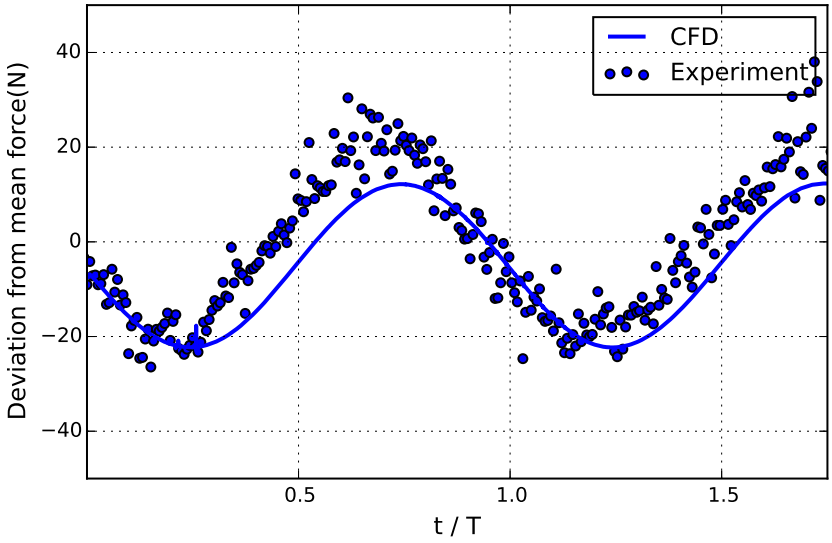

(a) $\omega = 2.06\ rad/s$ $(r = 0.99)$

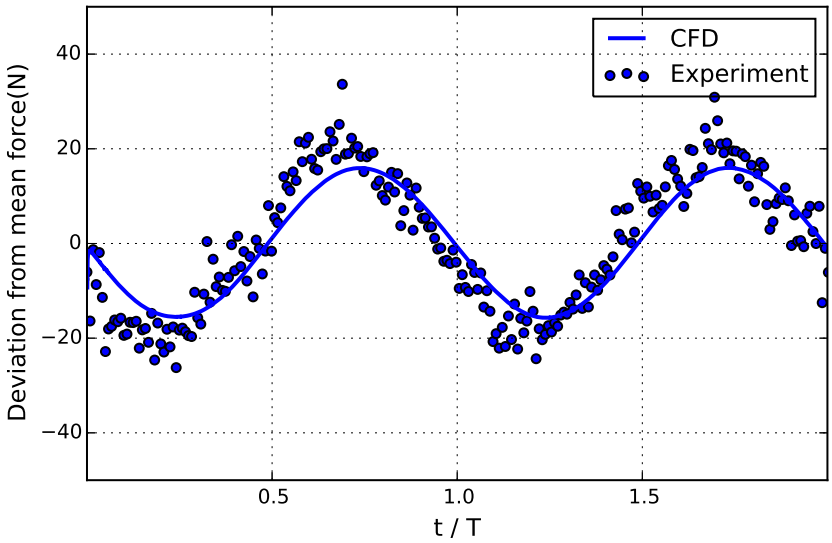

(b) $\omega = 2.61\ rad/s$ $(r = 0.98)$

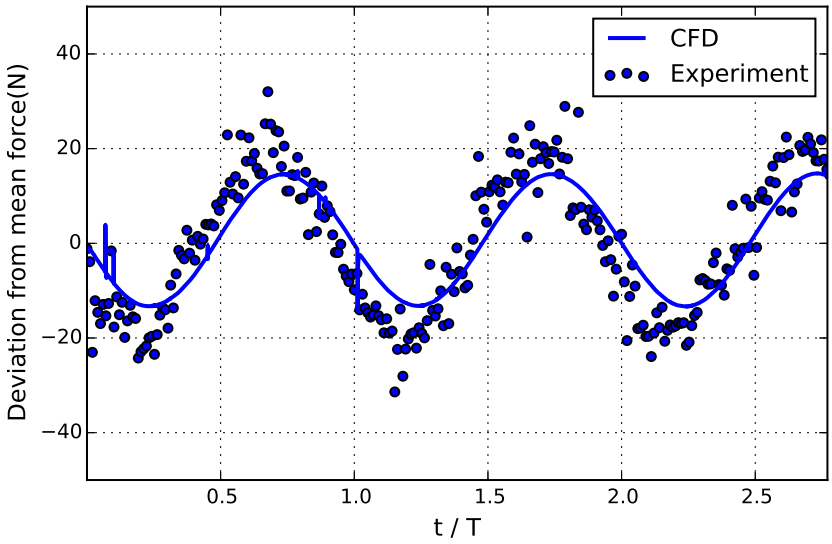

(c) $\omega = 3.17\ rad/s$ $(r = 0.99)$

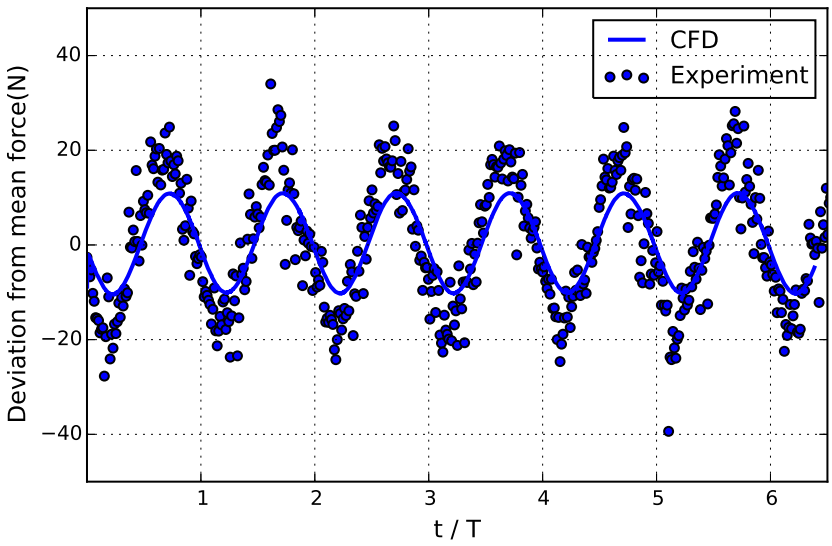

(d) $\omega = 3.99\ rad/s$ $(r = 0.99)$

Figure 2.6: Variation of hydrodynamic force on oscillating spar for $A = 0.04$ m, r is the correlation coefficient. The x-axis is nondimensionalized over time period of oscillation.

2.4 NWT results for radiation test on WEC B

For this test the spar of WEC B was subjected to forced oscillation with amplitudes in the range of $0.03 - 0.08\ m$ and frequency in the range of $1.5 - 3.99\ rad/s$ using CFD simulations in a quiescent tank. The test was performed for 30 s and the displacement, acceleration, and heave force were recorded. The hydrodynamic force on WEC B for amplitudes of $0.03\ m,\ 0.04\ m\ , 0.06\ m,\ 0.08\ m$ is plotted in Figure 2.7a, Figure 2.7b, Figure 2.7c and Figure 2.8b respectively. The time in the x axis is normalized with the time period of ocsillation. It can be seen that as the amplitude increases the profile of hydrodynamic force changes.

Beatty et al. (2015) concluded that the experimentally derived total damping from the physical wave tank radiation tests results for both the bodies is much greater than the BEM derived damping (Beatty et al., 2015). The reason stated for this is that the BEM code accounts for the damping effect due to radiation of waves but does not account for viscous effects. Since radiation is a free surface phenomenon and the geometries of both the reacting bodies are small at the free surface, the radiation damping is negligible. From this argument it is clear that viscous effects are the dominant source of damping for both reacting bodies. Apart from the viscous effect, the nonlinear relationship between the body position and hydrodynamic force is exposed by Figure 2.8. The body was oscillated in a perfectly sinusoidal manner about the mean position, yet the output force profile deviated from the perfect sine form.

The validation of the NWT using the diffraction and radiation tests establishes confidence in the overall accuracy of results generated using this NWT. Though inaccuracies exists between the NWT and physical wave tank results, the source of these can be attributed to several reasons as mentioned below.

- It has been concluded in Beatty (2015) that the transverse waves were present in the physical tank experiment. An assessment of the tank standing wave resonant frequencies and are given in Beatty (2015, Appendix F). The regression results indicate repeatable differences between the centreline and offset wave probe signals at 2.6 rad/s-4 rad/s. These repeatable differences are likely a result of excitation of transverse standing waves between the walls of the tank.

- It has also been mentioned in Beatty (2015) that the poor resolution of the linear motor (used as a position control actuator forcing the displacement of

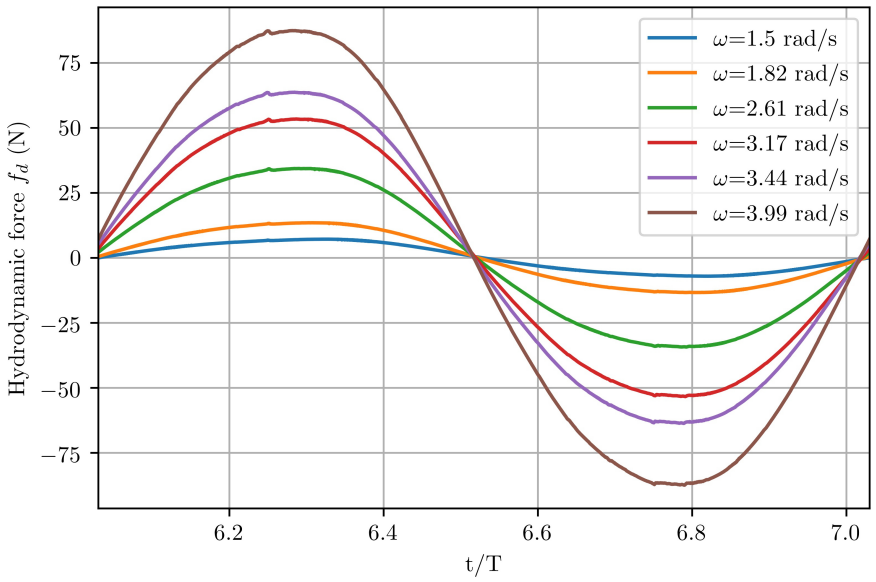

(a) Amplitude = 0.03 m

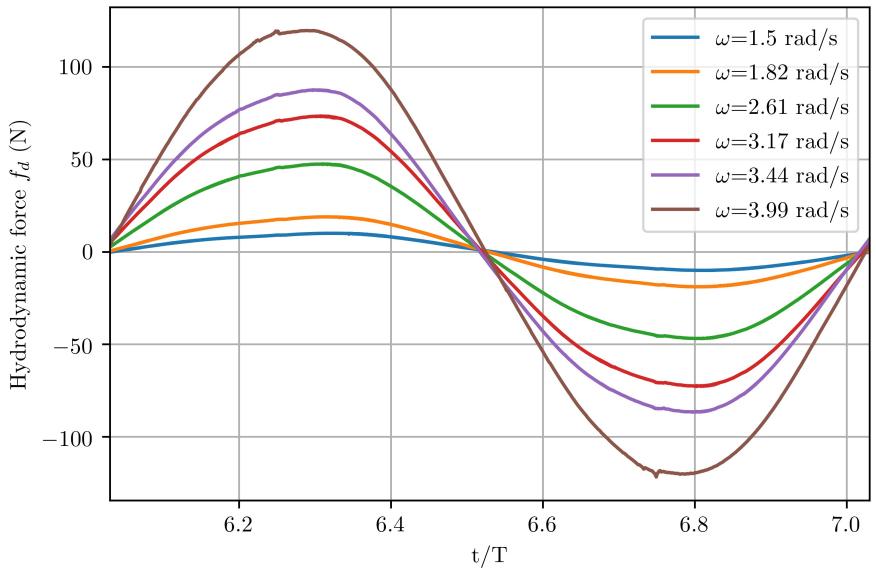

(b) Amplitude = 0.04 m

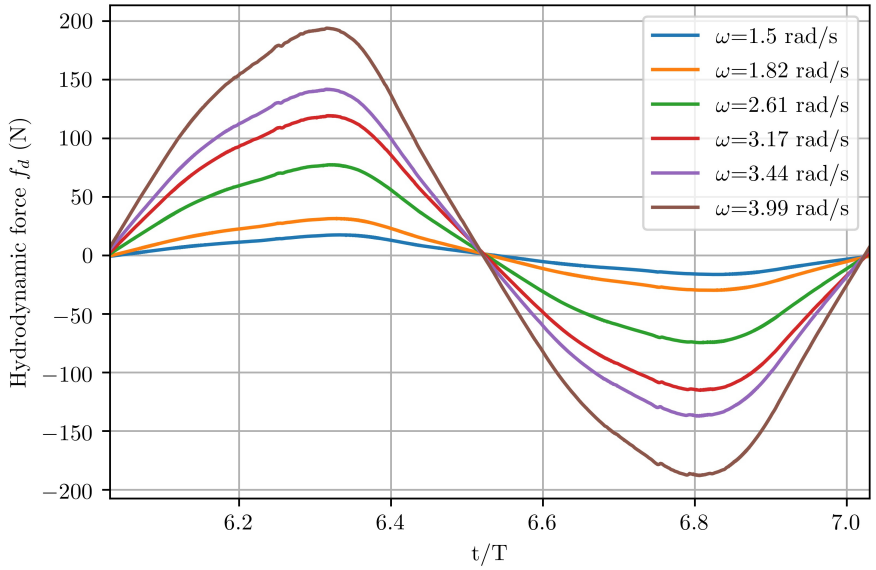

(c) Amplitude = 0.06 m

Figure 2.7: Hydrodynamic forces on WEC B oscillating at amplitudes of 0.03 m, 0.04 m and 0.06 m. (Hydrodynamic forces on WEC B oscillating at amplitude of 0.08 m is shown in Figure 2.8b. The x-axis is non-dimensionalized over time period of oscillation

spar in the experiment) as possible source of error in the physical tank test.

- In the physical experiments, the float was not present, and the tank depth was kept 2 m.

2.5 Summary and discussion

The potential theory formulation for WEC analysis along with the various assumptions also requires a set of reduced experiments. These simplified tank tests are used to generate constant hydrodynamic coefficients. Due to the nature of the tank tests and the superposition of various components in the mathematical model the accuracy of the results is adversely affected. The modified form of Newton's second law with distinct diffraction and radiation components derived from these tests is called Cummins equation (Cummins, 1962). Several attempts that have been made to include the non-linearity (mainly, viscid forces) as an additional term to the famous Cummins' equation have been discussed in this chapter. Though this approach is systematic, time tested and accurate for simple geometries and simplified environ-

mental conditions, it fails to predict the response for either oscillation of complex single/multi body geometry or complex environmental conditions. It can be confidently said that the due to the mathematical complexity, the sources of nonlinearity cannot be segregated. It was found that force magnitude obtained from CFD or NWT compared very well with the physical tank test results. But, due to absence of viscosity the BEM method could not provide accurate values of damping. Thus these results developed confidence in CFD methedology for further analysis.

In engineering applications, hysteresis nonlinearlity is often used to model the memory effect (Talatahari et al., 2012). The hysterisis nonlinearity has rate dependent characteristics, *i.e.* the output is nonlinearly dependent on the rate of input. This has been confirmed based on Figure 2.8a as the input to the NWT was sinusoidal oscillation of WEC B. From the WECs context it means that the hydrodynamic force should be related to the rate of input like body velocity/relative velocity or higher derivative of it like acceleration. The geometry considered is WEC B. The hydrodynamic force plotted in Figure 2.8a with heave velocity show hysteresis effect, these results have been plotted over various cycles of oscillations. The above mentioned hysteresis and nonlinearity indicate that the model structure previously studied should be analyzed with new perspectives, keeping in mind the heave plate designs of WEC geometries.

Thus, it is required that relationship between state variables and hydrodynamic forces should include variables like relative height, relative velocity and relative acceleration rather than fluid free surface, fluid velocity and fluid acceleration. The effect of fluid coupling due to radiation from oscillating geometries and scattering from irregular wave field should be simultaneously captured. This relationship should be the foundation on which mathematical complexity is added to simulate phenomenon like memory effect and causality/non-causality. An approach to use the data from a diverse set of representative tests and development of a model which would predict the systems response in a border set of environmental conditions is required. The *estimation/training* data used should provide a *true description* of the test case, *i.e* the data should be generated from high fidelity numerical modelling or physical experiments.

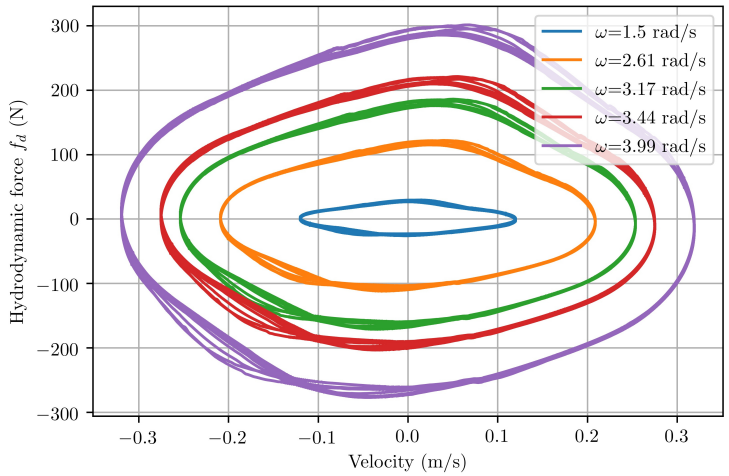

(a) Hysteretic relationship between hydrodynamic force and spar velocity

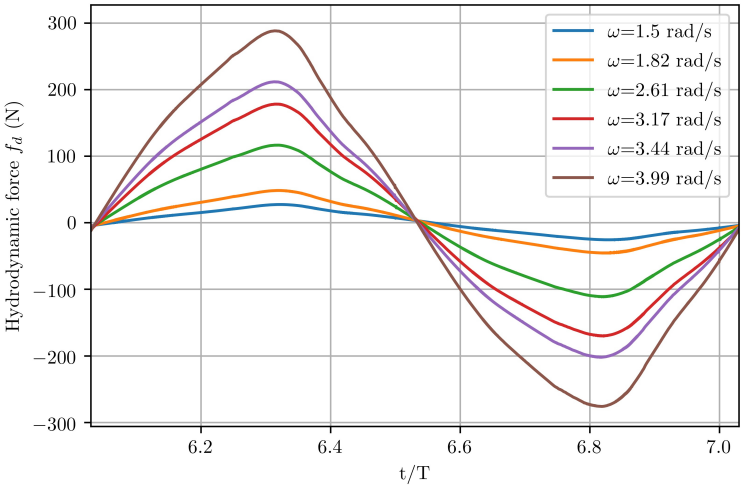

(b) Hydrodynamic force on spar in transient simulation

Figure 2.8: CFD calculated hydrodynamic force on WEC with heave plate oscillating with an amplitude of 0.08 m

Chapter 3

Data-driven hydrodynamic modelling of WECs

In the previous chapters it has been shown that, even though potential theory and mesh-based CFD methods are popular for modeling WECs, they have inherent limitations. Potential flow theory assumes that the fluids are inviscid and irrotational and can only model simple hull structures and small amplitude motions. Similarly in the finite volume based CFD codes it is difficult to treat large deformation and displacement of the fluids and structures and the complex fluid-structure interactions like over topping, wave breaking etc. Thus, new numerical models are necessary to solve these problems and to model SPARs more accurately.

The modelling approach presented in this Chapter and validated in Chapter 5 is that of system identification, where models are constructed from input/output data measured from the system under study. These models are used across a range of engineering fields to produce dynamic models of various systems as discussed in the literature review in Chapter 2. There are three main components to data-driven modelling, the input/output data, parametric model structure, and the identification process. These components are analysed in this chapter. A brief overview of the system identification, in general and specific to hydrodynamic modelling, along with a review of previous work is presented in Section 3.1. The characteristics of the input signal and advantages of numerical wave tank utilized for data generation is described in Section 3.2. Section 3.4 details the general classification of model structures based on the modelling issues that a system identification model should resolve, along with the specific characteristics of the blocks involved in block oriented models used in

this thesis. Section 3.3 describes the models used in this thesis. These models are subdivided into blocks with specific input, output and process. The block division facilitates parameter identification, which has been discussed in Section 3.5. The validation of models is discussed in Section 3.6. The chapter ends with a summary of various candidate models in Section 3.7.

3.1 System identification for hydrodynamic application

For hydrodynamic applications described in Chapter 2, a mathematical model is required which could reduce the errors associated with superposition of forces from different experiments, yet be able to capture the important nonlinearities of the real system in real time. The above requirements suggest that data models (black box), or a combination of data and physics model (grey box) could be a good alternative to a purely physics model (white box). A general discussion on the colour coded classification is presented in Chapter 1, with emphasis on the the characteristics of grey box model used in this and Chapter 5.

3.1.1 Overview and classification

In this chapter the complexity of the physical system is captured using limited CFD tests and the data thus generated is used to train the model to operate on various realizations of input condition. Several other applications of such models in wave energy conversion field (Bacelli et al., 2017; Cho and Coe, 2018) suggest that with sufficiently informative input data for the identification of nonlinear system, convergence with experimental or numerical data is obtained. Based on the above model categories, the building blocks of this work have been applied successfully to simple hull geometries heaving in water in Giorgi et al. (2016a,b) and Ringwood et al. (2016). In previous studies the focus was to construct a model structure to find a relationship between free surface and total hydrodynamic force for 2D; square, circular and triangular cylinders. The hydrodynamic force for these geometries were predicted from the model trained by CFD tests and performance of four discrete time models *viz.* Autoregressive with exogenous input (ARX), Nonlinear autoregressive with exogenous input (NARX), Artificial neural network (ANN) and Kolmogorov-Gabor polynomial (KGP) were compared. Though these models were able to predict the

hydrodynamic forces for simple hull shapes, these were limited to static non-linearity and did not include rate dependent input-output relationships. It is expected that the model structures employed in this thesis to simulate the hydrodynamics of more realistic WEC geometries like heave plates, should have capability to include larger degree of nonlinearity. The performance of the models employed in this thesis have been evaluated in Chapter 5.

3.1.2 Steps in system identification

The expectations from a system identification model is that it should be capable of describing the real system accurately, thus the objective of system identification is illustrated with the help of Figure 3.1. Assuming that the process or CFD tests produces only a single output, it is expected that the model will also do so and represent the behaviour of a process as closely as possible. The quality of model is measured in terms of the error between the process output and model output. This error should be utilized to tune and optimize the parameters of the model.

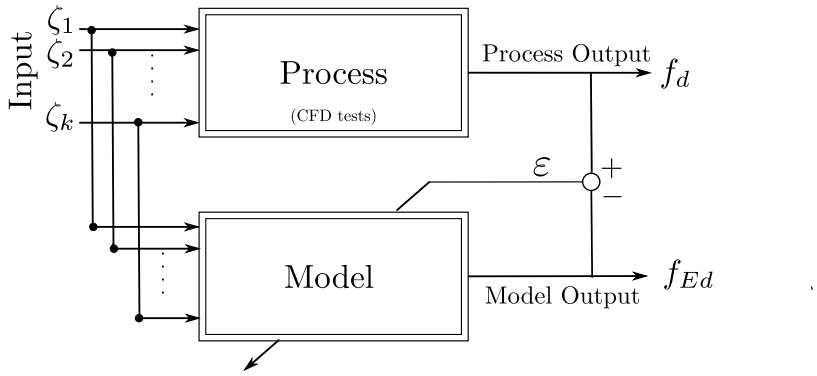

Figure 3.1: Working principle of system identification

In order to understand the data based modelling methodology, the procedure can be divided into various steps (Nelles, 2001; Isermann and Münchhof, 2011). The general order in which these steps are sequenced in this chapter and Chapter 5 is presented in Figure 3.2. The complexity and requirement of prior knowledge typically decreases as we move from step 1 to step 5. Each step in the procedure involves some decision making and can be intervened. The decisions involved in this thesis are enumerated as below and discussed in detail in Sections 3.2-3.6

1. Choice of model input

2. Choice of excitation signal
3. Choice of model structure and complexity
4. Choice of model parameters
5. Evaluation of above choices (Validation)

Based on the five steps mentioned above the purpose of system identification is to identify parameters that minimize the difference in the model output and process output. The model utilizes these parameters and predicts the output with different set of input data.

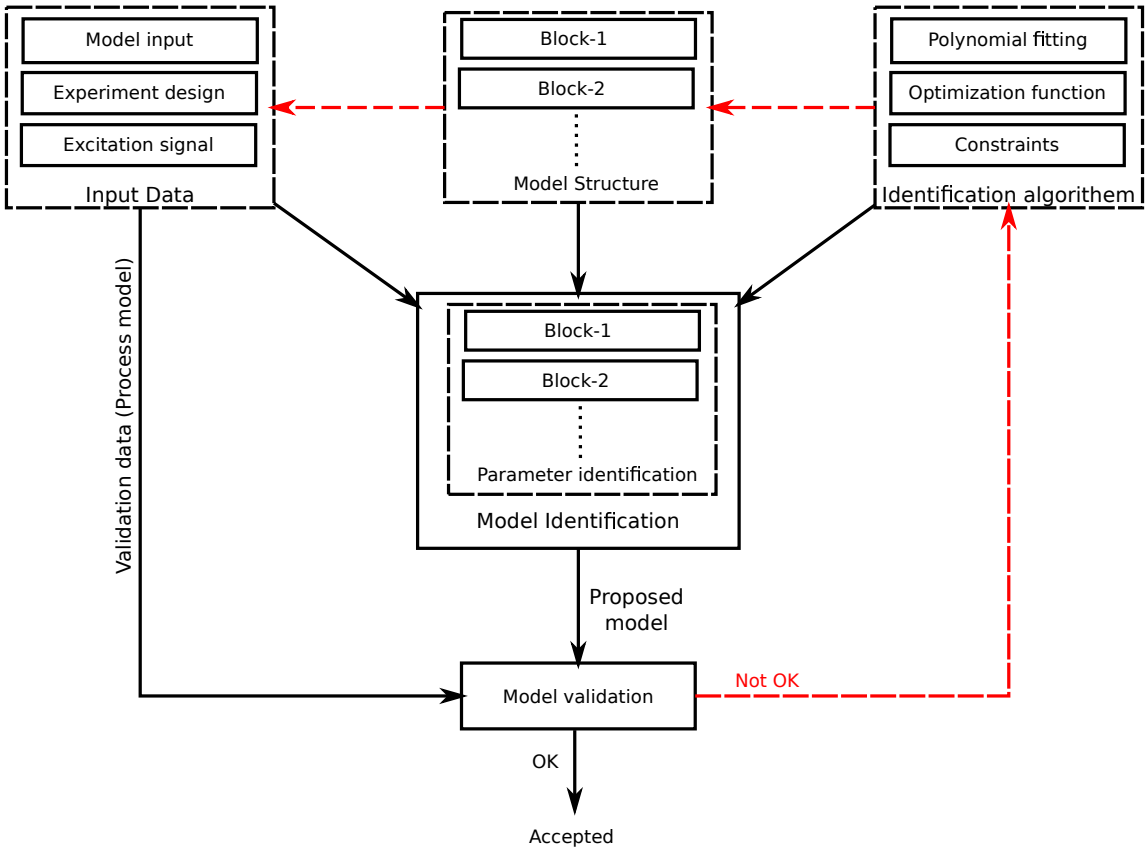

Figure 3.2: Block diagram representing sequence of steps in system identification

3.2 Input data

The primary requirement in system identification is ensuring that the experimental design used to generate data and the input-output data pair used to determine the

model is sufficiently representative of the system dynamics. Data generation process for the system identification can be subdivided into three main components as discussed below.

3.2.1 Choice of model input

As discussed in Chapter 2, the general procedure in wave tank testing is to either control the body oscillation or the free surface (radiation is modelled by forcing the device in the absence of waves and excitation by locking the device and measuring the force excreted by the waves). However, it has been well established in literature and previous chapter that the nonlinear effects are not captured because of this simplification. A better approximation of the nonlinear effects can be obtained by including both the inputs in the model as well as in the experiment design. Thus in this thesis, the model input encapsulates the free surface height (η) and the relative position of spar and float by a superimposed relative height (ζ) time series. This relative height represents the dynamic position of the spar with respect to free surface height. The main advantages of forcing both the inputs at the same time rather than single inputs are

1. Broader representation of operating conditions
2. Reduced signal to noise ratio

Once a model input, capable of reproducing the desired phenomenon to be modelled in an actual process is selected, the next step is to come up with the design of experiment. A brief outline on the modes of experiments for WEC, highlighting the benefits of one over the other is presented below in Section 3.2.2. The CFD experiments utilized in this thesis for data generation will be discussed in Section 4.1.

3.2.2 Design of experiments

In the case of WEC, there are three possible modes for data generation for populating a system identification model, *viz.* open ocean, physical wave tanks and numerical wave tanks. In this thesis the input data considered for the system modelling are generated using Numerical Wave Tanks (NWTs).

NWTs are used primarily for modelling nonlinear free surface waves, hydrodynamic forces and floating body motions, these are generalized virtual simulators with

first principles application of fluid dynamics. Current day computing power allows the implementation of NWTs using CFD. A comparison between various numerical tank software can be found in (Windt et al., 2019). In this thesis NWT has been introduced in Section 4.1.1 and the testing procedure will be detail in Sections 4.2 and 4.3 from data generation perspective for system identification application.

Using a CFD based NWT to generate data for WEC model identification has the following advantages:

- A wide variety of excitation signals, including incident waves and forces directly applied to the device.
- Low run time if 2D WEC geometries are simulated.
- Control on temporal resolution of measurement.
- Signals can be passively measured without requiring physical sensor devices, which can alter the device or fluid dynamics and are subjected to measurement error.
- In addition to the significant cost, physical wave tank experiments need physical prototyping.
- Tank wall reflections in physical tank may limit the range and duration of viable tests. The tank reflection have been discussed in several literature like (Beatty et al., 2019). In NWT these reflections can be controlled at initial level of tank design or by implementing appropriate boundary condition.
- A range of excitation signals is not likely to be available in the open ocean (at least not in a reasonably short time frame) and there are difficulties in exactly enumerating the excitation experienced by the device as there is no external control of the excitation
- NWT allows measurement of free surface at the location of WEC due to repeatability of exact simulation conditions in the absence of WEC.
- Do not require physical sensor devices, which are typical sources of random and systematic errors in the measurements (Giorgi et al., 2016b,a; Ringwood et al., 2016).

- One of the primary advantages of CFD is that once complete all the flow field variables are accessible and this can be used to develop improved white and grey models.

3.2.3 Choice of excitation signal

The signal used to excite the system during the experiment plays an important role in system identification. Input signals directly influence the identification process, as they affect the quality of the models, data processing and experimentation time. The characteristic of the signal is mostly dictated by the purpose of the model, required model input and design of experiment. If the presence of system nonlinearity is anticipated, it is important to properly excite the system in order to observe the system's response over the full range of interest. The experiment for data generation can be designed if the mathematical model structure utilised to model the process is available forehand. Ideally, the objective is to excite the system as much as possible, in the shortest possible time, in order to obtain all the required identification information.

In this thesis a multisine signal is used as input freesurface height and the WEC is oscillated with a periodic signal. The multisine signal allows strong control over the spectral content, with free choice for the maximum amplitude of each harmonic. For a multisine signal there is flexibility in the amplitude distribution, indeed the amplitude distribution is determined by the phases of the harmonic components. This leads to control over the amplitude content, through phase optimisation techniques (Schoukens et al., 1998; Pintelon and Schoukens, 2012). Typically, the crest factor for a multisine signal is 1.7. Other useful signals that can be use in system identification are random and pseudo-random binary signals, random amplitude random period signals and chirp signals (Isermann and Münchhof, 2011).

For a WEC, the input excitation signal ranges should be bounded between a maximum and minimum level, either because of survivability issues of the WEC, or because the WEC is intentionally designed to work in a specific ranges as discussed in Sections. 2.3.2 and 2.3.3. In the identification experiment design, it is important to restrict the input and output amplitude to the ranges at which the system is supposed to normally operate. Indeed, it is not advantageous to introduce unnecessary complexity in the model structure, just in order to describe the system behaviour, in conditions which are not of interest, from a practical point of view. For example, in the case of WEC modelling for power production, the objective is to obtain

a model able to describe the WEC dynamic in power production mode, and not in extreme sea conditions when the WEC switches to survival mode. The survivability conditions translate to situation of latched float and spar which is not important to simulate. This condition occurs mostly during storm and are associated with overtopping. Thus in current study it is made sure by means of bounds of input signal that such situation is never encountered.

3.3 Block Oriented Models (BOM)

In this thesis, the nonlinear system identification models used in (Giorgi et al., 2016a,b), have been extended to include a nonlinear rate dependent block, so that the additional nonlinearities can be modelled and the input free surface data can be transformed into more accurate hydrodynamic force data. As with the introduction of the nonlinear static block, the black box ARX model becomes a grey box Hammerstein model. Similarly, it can be said that after inclusion of a nonlinear rate dependent block the modified Hammerstein model takes a lighter shade of grey. This model will be hereafter referred as a rate dependent Hammerstein model. Another nonlinear model that has been discussed in this chapter and in Chapter 4, is rate dependent Kolmogorov-Gabor Polynomial model (KGP), which has been built by introducing rate dependent block in the KGP model. The Hammerstein model is discussed in Section 3.3.1 and the rate dependent Hammerstein and KGP models are discussed in Sections 3.3.2 and 3.3.3, respectively.

3.3.1 Hammerstein model

The model chosen for the prediction of hydrodynamic force is expected to exploit the relationship between the relative position of the spar and the hydrostatic force along with the excitation force values obtained from hydrodynamic CFD tests. A model with a cascade connection of several individual blocks, performing specific functions is simple to understand and easy to implement computationally. One such model, which finds wide application in engineering is the Hammerstein model (Eskinat et al., 1991).

Hammerstein model assumes a separation between the nonlinearity and the dynamics of the process. Hammerstein model has been previously used to predict hydrodynamic force on simple spars geometries by exploiting the relationship between

freesurface with hydrostatic force (Giorgi et al., 2015, 2016a,b). In this work similar methodology has been adopted and discussed to predict hydrodynamic force on simple hull shapes and widely used spars fitted with heave plates. It was found that though the model accurately predicted hydrodynamic forces on simple geometries it failed to do so for Heave Plate cylinder (HP cylinder).

The Hammerstein model can be represented by a static block with linear or nonlinear relationship between the input $\zeta(k)$ and output variables $f_{ES} = s(k)$ followed by a dynamic block (ARX model) with linear dependence between input $s(k)$ and estimated output $f_{Ed}(k)$ as shown in Figure 3.3. It implies that the general structure of the model should be represented by the following equation:

$$\begin{aligned} s(k) &= r(\zeta(k)) \\ &= f_{Es}(k) \end{aligned} \tag{3.1a}$$

$$\begin{aligned} f_{Ed}(k) &= b_1 s(k-1) + b_2 s(k-2) + ... + b_m s(k-m) \\ &\quad - a_1 f_{Ed}(k-1) - a_2 f_{Ed}(k-2) - ... - a_m f_{Ed}(k-m) \end{aligned} \tag{3.1b}$$

where ζ is the input relative height, s is an inaccessible intermediate variable, $r\ (\cdot\ )$ is the function which describes the static function, f_{Ed} is the output estimated hydrodynamic force, $a_1,\ a_2\ ....\ a_m$ and $b_1,\ b_2\ ....\ b_m$ are the coefficient values of output and intermediate variables. The estimated current value of the output $f_{Ed}(k)$ is dependent on the previous values of input $s(k-i)$ and output $f_{Ed}(k-i)$, where $i = 1, 2 \ldots m$.

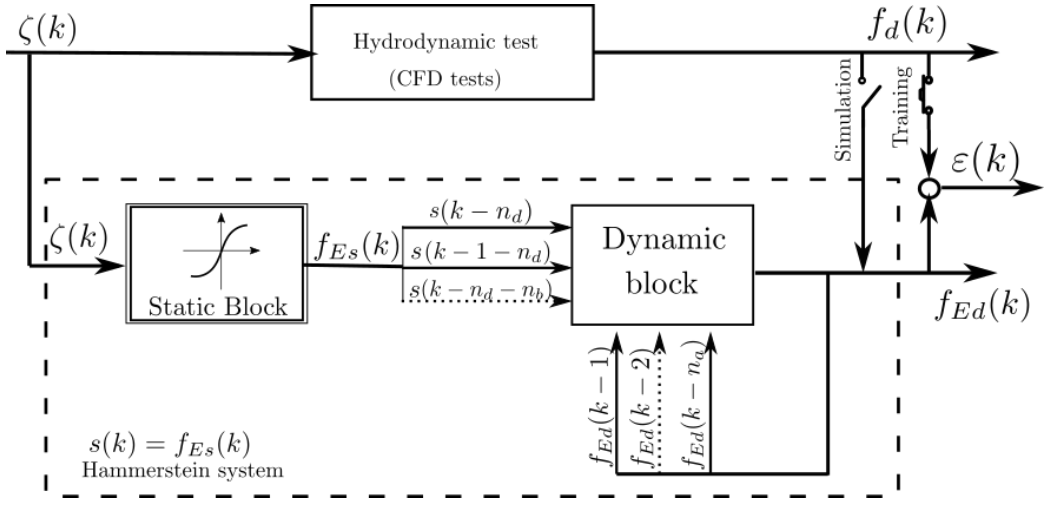

Figure 3.3: Block diagram representing Hammerstein model

Yu and Falnes (1995) found that the relationship between input freesurface height

η and output excitation force f_e is causal. Therefore, it is expected that the system identification model should include causality in the formulation. Since the current value of hydrodynamic force $f_{Ed}(k)$ is dependent on various values of two variables $f_{Ed}(k-i)$ and $s(k-i)$, it is expected that m is specific to these variables. In a discrete time model, the value of m can be determined by reducing the error between the value of estimated hydrodynamic force f_{Ed} and those generated by CFD f_d. In Figure 3.3, this is represented by the training circuit with closed switch. Let n_a be the weighted factor to determine the contribution of hydrodynamic force. The dynamical order of model is represented by n_a and n_b. They can be correlated to the stiffness of the model. Higher orders make the model more representative of complex behaviour at the expense of generalization on new data. By introducing n_b and n_d the effect of relative position on the dynamic force can be quantified. n_d will be referred as the time delay constant. Thus, by including the dynamic order and time delay constants Eq. (3.1) can be written as:

$$f_{Ed}(k) = \sum_{i=1}^{n_a} a_i f_{Ed}(k-i) + \sum_{i=0}^{n_b} b_i r(\zeta(k-n_d-i)) \tag{3.2}$$

For a causal system, $n_d \geq 0$ implies that the variable at any instant only depends on the variable at previous times, otherwise if $n_d < 0$ the system is non-causal and the present value is influenced by future variable values as shown in Figure 3.5. Though the Hammerstein model is linear in a_i and b_i, depending on the function r $(\cdot)$ it can be characterized to have a linear or nonlinear input-output relationship. Most previous works on Hammerstein model and identification have focused on the case of memoryless nonlinearities. In general, the static nonlinear block of Hammerstein model can be carried out using polynomial form, neural network (Lawrynczuk, 2011), spline functions (Chan et al., 2006) and LS-SVM (Falck et al., 2009) etc. In terms of wave energy application Giorgi et al. (2015, 2016a,b) have compared the effect of linear/nonlinear static function for various geometrical shapes like straight walled (rectangular cylinder, triangular cylinder) and curved wall (circular cylinder). For a generalized nonlinear system, a Hammerstein based model is discussed in terms of WEC applications and procedure to identify the model parameters of the hydrostatic model and linear dynamic ARX model are established in Sections 3.5.2 and 3.5.4.

3.3.2 Rate dependent Hammerstein model

Even though the classical Hammerstein model can accurately model a simple physical system with linear/nonlinear static block and linear dynamic block, it fails when the output of the real system is effected by memory from previous times. Memory dependent nonlinear behaviour have often been described by hysteresis. In WEC applications it implies that the hydrodynamic force is not only dependent on instantaneous or past values of forces and positions of spar but also on the relative velocity and relative acceleration of of spar. This hysteretic behaviour is also encountered in oscillation of damper plates as shown in Chapter 2, where the hydrodynamic force on the plate is dependent not only on the instantaneous position of the plate but also on the previous positions with respect to the free surface. Thus if the fluid memory effects, dominates the hydrodynamic forces on the plate, a component of hydrodynamic force is represented by hysteresis loop. It has been shown that the shape of hysteresis component of hydrodynamic force depends on the applied frequency of the input (Wang et al., 2012). Such a hysteresis is called rate-dependent or dynamic hysteresis. This can be verified for analyzing hydrodynamic force when WEC is subjected to monochromatic waves of different characteristics. In this thesis only panchromatic input waves are used for calculating the hydrodynamic force.

A Hammerstein model for rate-dependent hysteresis in WEC application is proposed in this thesis. The block diagram of the Hammerstein model with rate-dependent characteristics for a WEC can be constructed as shown in Figure 3.4, which is similar to a classic Hammerstein model, except that a new block with higher order state dependence and a hysteresis function is added. A survey of mathematical models for hysteresis can be found in (Mayergoyz, 1993). In this thesis the Bouc-Wen model (see Section3.4.2) is employed to model the hysteresis effect.

3.3.3 Rate dependent Kolmogorov-Gabor polynimial model

The Kolmogorov-Gabor polynimial (KGP) model represents a nonlinear model with output feedback and utilizes polynomial nonlinearity to describe the system dynamics (Nelles, 2001; Bacelli et al., 2017). Like the ARX model described in Section 3.4.3, KGP is also a block box model linear in model parameters, but unlike ARX, KGP can model a nonlinear input/output relationship. The block diagram for KGP model is same as Figure 3.3, except that the dynamic block can model a nonlinear relationship

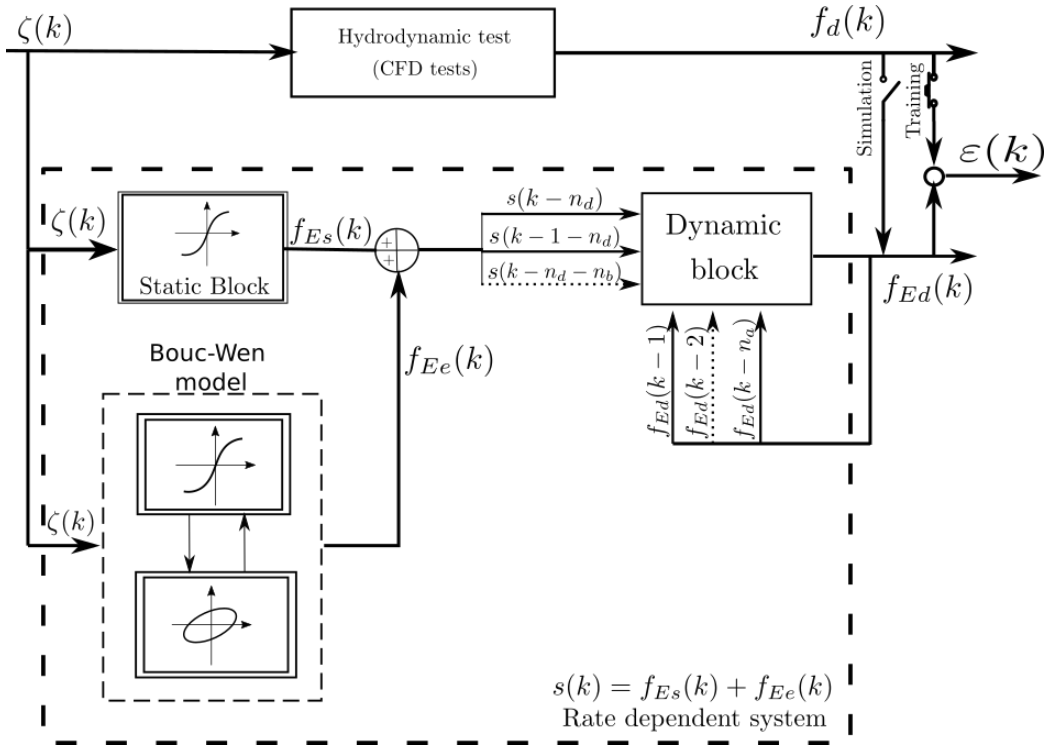

Figure 3.4: Block diagram of modified nonlinear system identification model with rate dependent block (*i.e.* Bouc-Wen model)

between the input and output. KGP model is described by the following equation:

$$\begin{aligned} f_{Ed}(k) = & \sum_{i=1}^{n_a} a_{i1} f_{Ed}(k-i) + \sum_{i=0}^{n_b} b_{i1} r(\zeta(k-n_d-i)) \\ & + \sum_{i=1}^{n_a} a_{i2} f_{Ed}^2(k-i) + \sum_{i=0}^{n_b} b_{i2} r(\zeta^2(k-n_d-i)) \\ & + \ldots \\ & + \sum_{i=1}^{n_a} a_{ip} f_{Ed}^{n_p}(k-i) + \sum_{i=0}^{n_b} b_{ip} r(\zeta^{n_p}(k-n_d-i)) \\ & + \ldots \\ & + \sum_{i=1}^{n_a} \sum_{j=0}^{n_b} c_{ij} f_{Ed}(k-i) r(\zeta(k-n_d-i)) \\ & + \ldots (\text{other cross-product terms}) \end{aligned} \tag{3.3}$$

where ζ is the input relative height, $r\ (\cdot)$ is the function which describes the static function, f_{Ed} is the output dynamic force, $a_{ij},\ b_{ij}$ and c_{ij} are the model parameters. The number of parameters required for identification can be obtained by modifying the equation in (Nelles, 2001) into following equation

$$N_{par} = \frac{((n_a + n_b + 1) + n_p)!}{(n_a + n_b + 1)!\ n_p!} \tag{3.4}$$

The number of regressors increase strongly with an increase in polynomial order p, and dynamical order n_a, and n_b leading to instability issues. Even if the problem is stable, huge model complexity requires utilization of computationally intensive linear subset selection techniques. Thus, attempt should be made to reduce the model complexity by evaluating the relevance of each term. It was found that the presence of cross-terms cause stability issues (Alves et al., 2016), thus neglecting the cross terms, Eq.(3.3.3) can be modified to:

$$f_{Ed}(k) = \sum_{j=1}^{n_p} \Big[\sum_{i=1}^{n_a} a_{ij} f_{Ed}^j(k-i) + \sum_{i=0}^{n_b} b_{ij} r(\zeta^j(k-n_d-i)) \Big] \tag{3.5}$$

In the absence of cross product terms, the number of terms to be estimated for the KGP model reduces substantially and is given by:

$$N_{par} = n_p(n_a + n_b + 1) \tag{3.6}$$

A rate dependent KGP model is proposed in this thesis. The block diagram for rate dependent KGP model is shown in Figure 3.4, which is similar to the rate dependent Hammerstein model except that the dynamic block can model a nonlinear relationship between the input s and output f_{Ed}. Performance of KGP models has been evaluated and compared with other models in Section 5.5.

3.4 Blocks of BOM

The choice of model architecture is the most subjectively influenced decision. The intended application of a model along with several other factors can often determine the most appropriate model architecture. The selection of model can be subdivided into the choices to be made in regards to the model structure, complexity, dynamic representation, model order and model parameters. Indeed, it is usual to describe a complex system as an interconnection of smaller sub-systems, each one having a specific input and output. Therefore, the experiments are designed to excite each sub-block, leading to the direct measurement of the input and output of each sub-system. This provides data for the identification of each sub-block. A similar approach has been utilized in this thesis. The details of the model presented in Section 3.3 reflect on the requirement of individual blocks with specific task of modelling independent components.

Thus keeping in mind the expectations from the model along with the detailed discussion on classification of models in Section 1.1, decision is made on the proposed model structure. Though the continuous time models are widely used in WEC modelling as discussed in Sections 2.1.2 and 2.1.3, discrete time models should be exploited primarily because of discrete nature of experimental results and easy computer implementation. It should be a nonlinear discrete time model capable of simulating dynamic and causal or noncausal behaviour. Considering the time domain discrete nature of the data from CFD, the system identification should be based on discrete time models. The model should exploit the relationship between the input and output data and use them to predict the required output for a new set of input

data (see Figure 3.2). These relationships are primarily freesurface/relative position with hydrostatic force, freesurface velocity/relative velocity with hydrodynamic force, freesurface accelaration/relative accelaration with hydrodynamic force and the coupling between various input parameters with the hydrodynamic force. Since most of the phenomenona are understood beforehand parametric curves can be utilized and external dynamics approach with feedback loops can exploit the data generated in open loop experiments. The individual components of the proposed architecture are discussed below in Sections 3.4.1, 3.4.2 and 3.4.3. The cascade of these individual components result in complete model structure, which has been discussed in the Section 3.3.

Another important factor to consider is the choice of model order; with external dynamics approach the choice of dynamic order of the model increases the dimensionality of the problem and hence the complexity. When using a low model order while simulating nonlinear dynamics it can be expected that a significant amount of dynamics goes unmodeled (Nelles, 2001). It has been shown that a significantly low order model is applicable while simulating the hydrodynamics of a simplified WEC geometry like a square cylinder (Giorgi et al., 2015). It is expected that the model order should be higher while simulating WECs with heave plate. Nonetheless, lower order models must suffice because often the modelling error is dominated by approximation error caused by an inaccurate description of the process nonlinearity.

3.4.1 Static block

In floating bodies the hydrostatic force due to the submergence of body in water is the dominating force. It is expected that the calculation of hydrostatic force will have a direct relationship with the water plane area. The model in any structural format should include this force which is a function of free surface. A simple way to model this is to assume a linear or nonlinear relationship between the input relative height, ζ, and the output hydrostatic force, f_s. The nature of this relationship can be described by following equation:

$$f_s(k) = r(\zeta(k)) \tag{3.7}$$

where ζ is the input variable, f_s is the hydrostatic force and $r\ (\cdot\ )$ is the function which describes the static function. Eq.(3.8) shows that, in the model, there is no memory effect; the output at the instant k depends only on the input at the same

instant k. The static function, r, can be approximated with a linear combination of basis functions; therefore Eq. (3.7), can be re-writtern as:

$$f_{Es}(k) = c_1\zeta(k) + c_2\zeta^2(k) + ... + c_{n_c}\zeta^{n_c}(k) \tag{3.8}$$

where ζ is the input variable, f_{Es} is the estimated value hydrostatic force, and $c_1, c_2, \ldots c_n$ are linear combination of coefficients

3.4.2 Rate dependent block

Bouc developed a hysteresis model for an inelastic SDOF system subjected to forced vibration (Bouc, 1967), which was further generalized by Wen (Wen, 1976). An approximate solution procedure for random vibrations was mathematically found. Later known as Bouc-Wen model, it has been extensively used as a mathematical model obtained by deterministic approach to represent systems with hysteresis and nonlinear behaviour. The Bouc-Wen model has been applied to model a wide class of hysteretic systems, like piezoelectric actuator (Wang et al., 2012), magnetorheological dampers (Kwok et al., 2007; Talatahari et al., 2012) and wood joints (Foliente, 1995). Though the literature suggests that this model has been successfully used to predict the behaviour of the physical hysteretic element and also for control purposes, the review of literature in this thesis have not found any application related to hydrodynamics of ocean WECs. Thus this thesis proposes modelling the nonlinear hysteretic hydrodynamic force encountered during oscillation of WEC under the influence of waves with a Bouc-Wen model independently, as well as in-line, with the system identification models like the Hammerstein and KGP models. The Bouc-Wen model is a set of differential equations describing the hysteretic characteristic of the excitation force on WEC as obtained from the hydrodynamic test mentioned in Section 4.3. In the context of WECs, the governing equation for Bouc-Wen model can be written as in Eq. (3.9). In this model, nonlinear restoring force is related to the system input through a first order nonlinear differential equation, as shown in Eq. (3.9b):

$$f_{Ee} = a\zeta + b\dot{\zeta} + c\ddot{\zeta} + h \tag{3.9a}$$

$$\dot{h} = \alpha\ \dot{\zeta} - \beta \mid \dot{\zeta} \mid h \mid h \mid^{n-1} - \gamma\ \dot{\zeta} \mid h \mid^{n} \tag{3.9b}$$

where f_{Ee} is the model calculated dynamic excitation force (*i.e.* to approximate residual of static force f_{Es} and CFD calculated dynamic force f_d) a, b and c are

the coefficients of relative position ζ, relative velocity $\dot{\zeta}$ and relative acceleration $\ddot{\zeta}$ respectively. The hysteretic nonlinear term is represented by static variable h. α controls the amplitude of the hysteretic loop, while the coefficients β and γ control the shape of the hysteresis loop. Though these range of unknown parameters (α, β, γ and n) are directly responsible for the shape of hysteresis, their physical meaning cannot be comprehended directly, but will be discussed later in Section 5.3. The response of the system depends on the values of these parameters.

3.4.3 Dynamic block

The dynamic block consists of an autoregressive with exogenous input (ARX) model, also known as the equation error model (Nelles, 2001). The dynamic block operates on the combined output of static and rate dependent block, who's combined output is termed as "internal force". The dynamic block therefore acts to reduce residual error of the prediction. The ARX model is the simplest linear discrete-time input/output model. This model can be easily extended to accommodate nonlinear relationship between input and output variables. In this thesis linear and nonlinear input/output relationship ARX models are utilized to describe the relationship between the estimated output hydrodynamic force f_{Ed} and input internal force s signal.

$$f_{Ed}(k) = \gamma[f_{Ed}(k-1), ... f_{Ed}(k-n_a), s(k-n_d), s(k-n_d-1), ... s(k-n_d-n_b)] \quad (3.10)$$

where, f_{Ed} and s are the output and input variables respectively, $\gamma[\cdot]$ is a linear or nonlinear function and $f_{Ed}(k)$ is the present value of output which depends on the past values of output $f_{Ed}(k-1), ... f_{Ed}(k-n_a)$ and input variables $s(k-n_d), s(k-n_d-1), ... s(k-n_d-n_b)$. The dynamic order of the model is represented by integers n_a and n_b. They can be correlated to the stiffness of the model. Higher orders make the model more representative of complex behaviour at the expense of generalization to new data. To account for nonlinearity, the model should be flexible and the model order should be optimal to avoid possible over fitting. The difference between a causal system and a noncausal system can be explained with the help of Figure 3.5. For a causal system, $n_d \geq 0$ implies that the variable at any instant only depends on the variable at previous times (see Figure 3.5a and Figure 3.5b), otherwise if $n_d < 0$ system is noncausal and present value is influenced by future variable values (see Figure 3.5c). From WEC prespective it would mean that for a causal system, the relative height information from past would be required inorder to predict the

current hydrodynamic force, where as for noncausal systems either only the future information or a combination of past and future information would be used. Since, the relative position at the centre of the spar is considered and so the wave elevation that is yet to arrive might be causing a vortex at the extreme leading edge of the heave plate. The parameters can be estimated by linear least square techniques. Parameter estimation of dynamic will be discussed in Section 3.5.4.

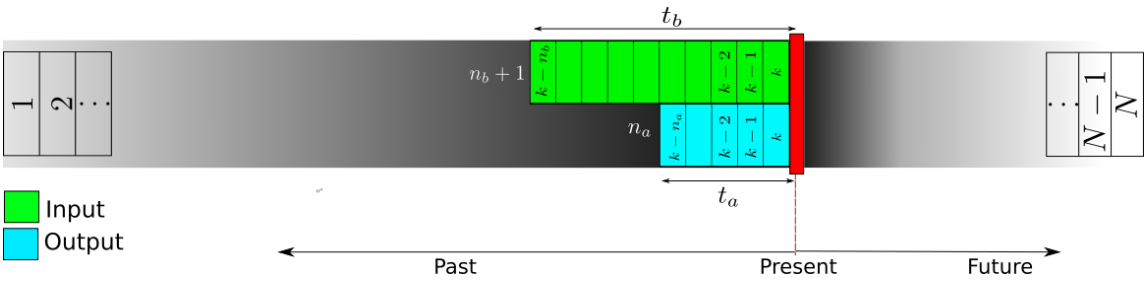

(a) Causal system with no time delay

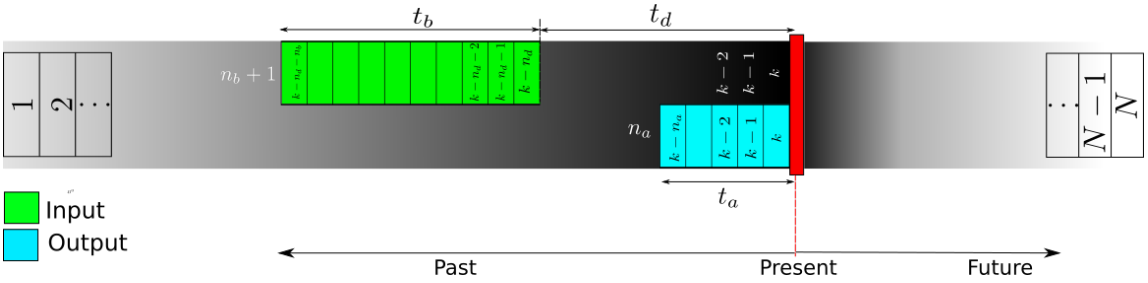

(b) Causal system with positive time delay

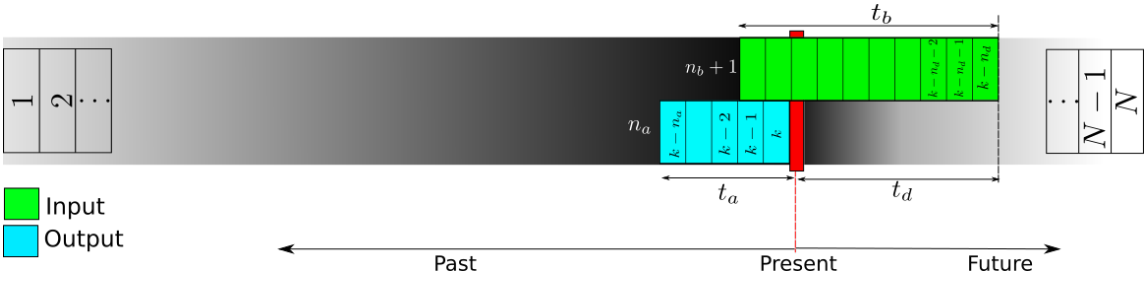

(c) Non-causal system

Figure 3.5: Possible scenarios in system identification describing causality, blocks represent discrete time steps

3.5 Parameter identification

Given a parametric model structure and the measured input-output data from an investigated process (*i.e.* CFD tank experiments), the objective of SI is to find the

values for the model parameters in order to obtain the 'best' model to describe the process. Therefore, it is necessary to select a quantifiable criteria to evaluate the performance of a model. In this thesis the quantifiable criteria is defined as error metric and a methodology for identification of parameters of individual blocks of models discussed in Sections. 3.3 is presented. The objective functions and the constraints of the optimization problem along with the mathematical techniques for parameter identification are also discussed. The identification procedure for parameter **C** of static block (see Eq. (3.8)), seven parameters of Bouc-Wen model (se Eq. (3.9)) and three parameters (see Eq. (3.10)) of the dynamic block is as mentioned in Sections 3.5.2, 3.5.3 and 3.5.4, respectively. These identification technique are implemented to case studies in Sections 5.2, 5.3 and 5.4 respectively.

3.5.1 Error metric

Error metrics measure the error between the output of a model and training or validation data. Several error metrics exist in literature and they can provide a way to quantitatively compare the performance of two models or case scenarios. In this thesis these metrics have been used to compare the performance of individual blocks, by comparing the input and output of that block as well as to compare the performance of entire model. These error metrics are also used to calculate the loss function in objective function during the optimization process. Two error metrics that are used in this thesis:

Mean absolute percentage error (MAPE) measures the average of errors, *i.e* the average difference between the estimated value and the actual value. Mathematically it can be writtern as:

$$MAPE = \frac{100}{N} \sum_{k=1}^{N} \frac{|y(k) - y_E(k)|}{|y(k)|} \tag{3.11}$$

where, $y(k)$ is the true value of the parameter or the process output and $y_E(k)$ is the estimated value, N is the total number of samples or total number of measurement at discrete time. Thus discrete time steps are represented by k, where $k = 1, 2 \ldots N$. The MAPE is a measure of the quality of an estimator it is always non-negative, and values closer to zero are better. Though this error metric is normalised with respect to true value $y(k)$, it fails to provide an accurate picture at $y(k) = 0$. In the context of wave energy, it is common

that values oscillates around the mean value, and the mean is often translated to zero. Therefore their is a possibility of obtaining a distorted picture of the error. Thus in this thesis whenever the error of nonperiodic and positive quantity is measured MAPE is used, particularly for evaluating the model performance in frequency domain. For oscillating variables or time domain results another error metric is used as discussed below.

Normalised root mean squared error (NRMSE) Another error metric that is widely used in this thesis is normalised root mean squared error, which has the advantage of being normalized as well as it presents an undistorted picture even for oscillating signals. Mathematically it can be written as:

$$NRMSE = \frac{\sqrt{\frac{1}{N}\sum_{k=1}^{N}|y(k) - y_E(k)|^2}}{\sqrt{\frac{1}{N}\sum_{k=1}^{N}|y|^2}} \tag{3.12}$$

This metric has been used extensively for error measurement between input and output signal across blocks. For example, refer to Eqs.(3.15), (3.23) and (3.18) for its application in static, rate dependent and dynamic blocks respectively. In these equations, $y(k)$ has been replaced with the respective force signals and notation "ε" has been used to represent NRMSE. For training and blind cases, NRMSE has been used as loss function in the objective function.

3.5.2 Static block identification

Considering the model structure of the Hammerstein model, rate dependent Hammerstein model and rate dependent KGP model discussed in Sections 3.3.1, 3.3.2 and 3.3.3 respectively, the static block is a common feature in all the models. Static block in all the models is exploited to transform the relative height ζ into a static force f_{Es}. Thus, the first step in the identification of any one of the three system identification models used in this thesis is to identify the nonlinear static block. Linear regression can be utilized for identification, if the static function in Figure 3.3 and Figure 3.4 is approximated with a linear combination of polynomials. The relationship between input $\zeta(k)$ and output f_{Es} of the nonlinear static block can be represented by:

$$f_{Es}(k) = c_1\zeta(k) + c_2\zeta^2(k) + ... + c_{n_c}\zeta^{n_c}(k) + \varepsilon(k) \tag{3.13}$$

where c_i $(i = 1, 2, 3 \ldots n_c)$ are the unknown parameters. The input ζ and output f_s of the hydrostatic experiment (see Section 4.2) can also be approximated by a polynomial fit. Therefore the estimated hydrostatic force f_{Es} can be equated to the linear combination of coefficients and relative displacements by a polynomial fit:

$$f_s(k) = c_1\zeta(k) + c_2\zeta^2(k) + ... + c_{n_c}\zeta^{n_c}(k) = \sum_{i=1}^{n_c} c_i\zeta^i(k) \tag{3.14}$$

Least squares method can be utilized to extract polynomial coefficients. The normalized root mean square error (NRMSE) is $\varepsilon(k) = f_s(k) - f_{Es}(k)$. In matrix notation:

$$\varepsilon = \frac{\|\mathbf{f_s} - \mathbf{f_{Es}}\|_2}{\|\mathbf{f_s}\|_2} = \frac{\sqrt{|\mathbf{f_s} - \mathbf{XC}|^2}}{\sqrt{|\mathbf{f_s}|^2}} \tag{3.15}$$

where for all the values of k:

$$\varepsilon = \begin{bmatrix} \varepsilon(1) & \varepsilon(2) & \cdots & \varepsilon(N) \end{bmatrix}^T \tag{3.16a}$$

$$\mathbf{f_s} = \begin{bmatrix} f_s(1) & f_s(2) & \cdots & f_s(N) \end{bmatrix}^T \tag{3.16b}$$

$$\mathbf{f_{Es}} = \begin{bmatrix} f_{Es}(1) & f_{Es}(2) & \cdots & f_{Es}(N) \end{bmatrix}^T \tag{3.16c}$$

$$\mathbf{X} = \begin{bmatrix} [\zeta(1)]^1 & [\zeta(1)]^2 & \cdots & [\zeta(1)]^{n_c} \\ [\zeta(2)]^1 & [\zeta(2)]^2 & \cdots & [\zeta(2)]^{n_c} \\ \vdots & \vdots & \ddots & \vdots \\ [\zeta(N)]^1 & [\zeta(N)]^2 & \cdots & [\zeta(N)]^{n_c} \end{bmatrix} \tag{3.16d}$$

$$\mathbf{C} = \begin{bmatrix} c_1 & c_2 & \cdots & c_{n_c} \end{bmatrix}^T \tag{3.16e}$$

$$\tag{3.16f}$$

The parameters that minimize the least squares error are given by

$$\mathbf{C} = (X^T X)^{-1} X^T \mathbf{f_s} \tag{3.17}$$

The minimization of the loss function in Eq. (3.15) is not computed directly using Eq. (3.17) because the use of $X^T X$ increases the possibility of obtaining an ill-conditioned problem. Instead, a QR factorization method is implemented, which computes the LS solution directly from X, without forming $X^T X$ (Golub and Or-

tega, 1991). The parameter vector $\mathbf{C}$ is calculated for different values of n_c using the optimization function in Eq. (3.15). The smallest n_c, with the ε value less than 5% is chosen as the order of the polynomial fit.

3.5.3 Rate dependent block identification

In this section the rate dependent models with hysteresis nonlinearity are discussed in terms of WEC applications and procedure to identify the parameters of the the Bouc-Wen model are established. The model parameters to be identified are $a,\ b,\ c,\ \alpha,\ \beta, \gamma$ and n (see Eq.(3.9)). In linear potential theory a is known as the stiffness coefficient, b the viscous coefficient and c as the addedmass coefficient. The parameter α affects the rate-of-change of the hysteresis through the product with the velocity, *i.e.*, the term $\alpha\dot{\zeta}$. Its effect is negligible when the velocity is small. It is more noticeable at large velocities and contributes to the slope of the hysteresis. Hence, a small value for α is anticipated. The model parameters β and γ affect the hysteresis rate through the expressions $\beta \mid \dot{\zeta} \mid h \mid h \mid^{n-1}$ and $\gamma \mid \dot{\zeta} \mid h \mid^{n}$.

The parameters of Bouc-Wen model to be identified will have a coupling effect on the hysteresis and are subject to severe non-linearities. In general, conventional or gradient based system identification methods may not be appropriate as they require more parameters to be identified at a given accuracy or more computational resources for a given model. Thus in this study the Particle swarm optimization (PSO) algorithm discussed in Section 3.5.3 is utilized for identification of hysteresis block parameters.

Once the optimization technique to decided and the limits of optimal values for the parameters of Bouc-Wen model is known, an appropriate objective function must be minimized through optimization procedure. In current section minimization of normalized root mean square error (NRMSE) between the excitation force f_e values from CFD and those estimated from Bouc-Wen model f_{Ee} is used as objective function. The estimated excitation force f_{Ee} and the estimated static force f_{Es} constitute internal signal (s). In order to determine the objective function, Eq. (3.15) in Section 3.5.2 can be modified to:

$$\varepsilon = \frac{\|\mathbf{f_e} - \mathbf{f_{Ee}}\|_2}{\|\mathbf{f_e}\|_2} = \frac{\sqrt{\frac{1}{N}\sum_{k=1}^{N} |f_e(k) - f_{Ee}(k)|^2}}{\sqrt{\frac{1}{N}\sum_{k=1}^{N} |f_e(k)|^2}} \tag{3.18}$$

Initial value of hysteresis

To integrate the rate of hysteretic variable $\dot{h}$ in Eq. (3.9b), the "*integrate.solve_*ivp" in python is utilized. This function numerically integrates a system of ordinary differential equations using explicit Runge-Kutta method of order 5(4) (Dormand and Prince, 1980), given an initial value. The initial value of the system is not known as this is an optimization problem with guessed initial values of parameters. Therefore the initial values are obtained heuristically by finding the values of $f_{Ee}(k) - h(k) = a\zeta(k) + b\dot{\zeta}(k) + c\ddot{\zeta}(k)$ in Eq. (3.9a), and subtracting them to the CFD calculated values of $f_e(k)$. The mean of calculated value of $(f_e - (f_{Ee} - h))(k)$ is stored and the process is repeated again for $k = 1, 2 \ldots 10$. The minimum thus obtained is considered the initial value of the hysteresis component of force (h_0)

Particle swarm optimization

The parameters of the Bouc-Wen model that need to be identified will have a coupling effect on the hysteresis and are subject to severe non-linearities. In this regard literature points out to several computational techniques, like adaptive estimation approach (Chassiakos et al., 1998), genetic algorithm (Kwok et al., 2007) and evolutionary algorithm like PSO (Wang et al., 2012). The PSO technique is one of the powerful and widely used method for solving unconstrained and constrained global optimization problems. Thus in this study, PSO algorithm is utilized for identification of hysterisis block parameters.

In the PSO algorithm, the position of each particle in the swarm represents a possible solution to a problem in a g-dimensional space. Their are three main attributes of each particle, current position x_j , current velocity v_j and past best position p_{best_j}, for particles in the search space. Each particle in the swarm is iteratively updated according to the aforementioned attributes. Particles flocking optimizes a certain objective function in a PSO. Each particle knows its best value p_{best_j} so far and its position. This information has analogy to personal experiences of each particle. Moreover, each particle knows the best value so far in the group g_{best_j} among all p_{best} positions. The PSO algorithm targets to changing the velocity of each particle towards its p_{best_j} and g_{best_j} locations. In the algorithm, each particle moves to a new position according to new velocity and the previous positions of the particle. This is compared with the best position generated by previous particles in the fitness function, and the best one is kept; so that each particle accelerates in the direction of not

only the local best solution but also the global best position. If a particle discovers a new probable solution, other particles will move closer to it to explore the region in the process more completely. After several iterations, the swarm converges to the best particle position, which represent the best solution.

Applying the algorithm to obtain Bouc-Wen model coefficients results in the best particle position, which is the best value of seven model parameters that describe the input time series to the model. Since, a static model block that describes the static or the buoyancy force already exist, the input to the Bouc-Wen model is the excitation force f_e time series obtained by subtracting the hydrodynamic force and the obtained static force before the training phase of the model $f_d - f_{Es}$. The obtained parameters are thereafter used in the training and simulation phase to obtain the ovearall model output f_{Ed}

Limits of parameters

Due to large number of unknown parameters in the optimization function, the computational overhead of the PSO algorithm will be very high when compared to rest of the identification process. Thus inorder to bring down the computational time of Bouc-Wen parameter identification, it is important to define the search space of the parameters. This is done by providing an initial guess to the maximum and minimum values of the parameters in Eqs. (3.9a) and (3.9b).

Let the hysteresis term in Eqs. (3.9a) set to "0". Then the excitation force can be approximated by the slope at the two ends of the hysteresis. This occurs when the relative velocity $\dot{\zeta}$ is at its extremes while the relative displacement ζ is crossing zero. Assuming that the hysteresis is symmetric about the zero velocity axes and about the force offset, then a slope can be defined as

$$b_{max} \leq \frac{\Delta f_{Ee}}{\Delta \dot{\zeta}} = \frac{(f_{Ee})_{max} - (f_{Ee})_{min}}{\dot{\zeta}_{max} - \dot{\zeta}_{min}} \tag{3.19a}$$

$$b_{min} \geq -b_{max} \tag{3.19b}$$

Based on the above argument the values of c_{max} and c_{min} can be determined by

following equation

$$c_{max} \leq \frac{\Delta f_{Ee}}{\Delta \ddot{\zeta}} = \frac{(f_{Ee})_{max} - (f_{Ee})_{min}}{\ddot{\zeta}_{max} - \ddot{\zeta}_{min}} \tag{3.20a}$$

$$c_{min} \geq -c_{max} \tag{3.20b}$$

Similarly, when the relative velocity and relative acceleration is zero, the relative displacement attains its maximum and minimum values. Due to severe non-linearity, an empirical approximation to a is bounded by

$$a_{max} \leq \frac{\Delta f_{Ee}}{\Delta \zeta} = \frac{(f_{Ee})_{max} - (f_{Ee})_{min}}{\zeta_{max} - \zeta_{min}} \tag{3.21a}$$

$$a_{min} \geq -a_{max} \tag{3.21b}$$

The remaining model parameters $\alpha,\ \beta$ and γ, are directly responsible for the shape of the hysteresis and it is not straightforward to comprehend their physical meanings. Since n determines the order of terms in the Eq. (3.9b), it is necessary to have a positive value of the order, thus lower limit of n is set to 2. Higher orders are limited by limiting the upper bound of n to 5. However some analytical and experimental trial and error provides an insight on their effects on the shape of the hysteresis. For example in order to initialize the value of α, we can utilize the values of $a,\ b$ and c, determined above and calculate the value of $(f_{Ee} - h)$ in Eq. (3.9a).

$$\alpha_{max} \leq (f_e - (f_{Ee} - h))_{max} - (f_e - (f_{Ee} - h))_{min} \tag{3.22a}$$

$$\alpha_{min} \geq -\alpha_{max} \tag{3.22b}$$

The above equations only provide a guideline to determine the limits of parameter values in the search space for the optimization algorithm. The accuracy of these parameters for this purpose will also depend on the signal, the above equations are for monochromatic signal. As the objective of this work is to determine these parameters for multisine signal, the right hand side are multiplied by a factor unique for each equation. These factors were obtained by trial and error process and will differ with the signal under analysis. A point to be noted as shown in the block diagram in Figure 3.4 is that, the internal signal $s(k)$ is not same as f_{Es} as it was for the Hammerstein model, rather it is $s(k) = f_{Es}(k) + f_{Ee}(k)$.

3.5.4 Dynamic block identification

In this section the methodology to determine the parameters of dynamic block (ARX model) for all the three block oriented models is outlined. The knowledge of input and output signal to the dynamic block is required in order to identify the parameters. From the block diagram in Figure 3.3 and Figure 3.4 it can be seen that the internal signal s is the input to the dynamic block and the estimated hydrodynamic force f_{Ed} is the required output. For the purpose of identification the estimated value of hydrodynamic force f_{Ed} is to approximate the CFD calculated values of hydrodynamic force f_d.

Depending on the model the internal signals changes to acomodate details according to that model. For example internal signal is estimated static force f_{Es}, if basic Hammerstein model is used, or estimated values of static force along with estimated excitation force $(f_{Es} + f_{Ed})$ if either of the rate dependent models are used. Using the data from quasi-static and dynamic test discussed in Sections 4.2 and 4.3 respectively and the identification technique in Sections 3.5.2 and 3.5.3 the values of polynomial coefficients in $\mathbf{C}$, state dependent coefficients $(a,\ b,\ c)$ and hysteresis coefficients $(\alpha,\ \beta,\ \gamma,\ n)$ are known and it is possible to calculate the internal signal s.

Once the internal signal $s(k)$ is known, an appropriate objective function must be minimized through optimization procedure. In current section minimization of normalized root mean square error (NRMSE) between the hydrodynamic force f_d from CFD and those estimated f_{Ed} by the Hammerstein/rate dependent Hammerstein model (see Eq. (3.2)) or rate dependent KGP model (see Eq. (3.5)) is used as objective function. In order to determine the objective function, Eq. (3.15) in Section 3.5.2 can be modified to:

$$\varepsilon = \frac{\|\mathbf{f_d} - \mathbf{f_{Ed}}\|_2}{\|\mathbf{f_d}\|_2} = \frac{\sqrt{\frac{1}{N}\sum_{k=1}^{N} |f_d(k) - f_{Ed}(k)|^2}}{\sqrt{\frac{1}{N}\sum_{k=1}^{N} |f_d(k)|^2}} \tag{3.23}$$

The values of total hydrodynamic force f_d from the dynamic test described in Section 4.3 should ideally be the output of the ARX block for training case (provided ε in Eq. (3.23) $= 0$). So, it can be said that both the input and output of ARX block is known.

It can be seen from Eq. (3.2) that the estimate of hydrodynamic force is a function

of two variables. This implies that the parameters for linear optimization problem might be dependent on each other. Under such condition the parameters cannot be estimated directly by LS because the optimal parameters obtained by Eq. (3.17) for identification of nonlinear static block cannot be directly used. A constraint equation should be used and the least squares technique should accommodate for the constraint application. This constraint is shown in Eq. (3.24). It can be seen that the equation discribes the dependence of coefficients of output parameter and input parameter on each other and implies that the sum of the coefficients of output and input terms should be equal to 1.

$$\sum_{i=1}^{n_a} a_i + \sum_{i=0}^{n_b} b_i = 1 \tag{3.24}$$

where, a_i and b_i are coefficients of the output and input signals of ARX block, n_a and n_b are the number of terms of output and input signals influencing the current value of the estimate. The linear equality constraint is given by:

$$A\theta = d \tag{3.25}$$

where θ is $(N \times (n_a + n_b + 1))$ matrix, and each equation in the linear equation system represents an equality constraint. Eq. (3.25) can be solved by performing the constrained optimization with Lagrange multipliers, leading to following parameter estimate as mentioned in (Nelles, 2001):

$$\theta_{constr} = \theta_{unconstr} - H^{-1}A^T(AH^{-1}A^T)^{-1}(A\theta_{unconstr} - d) \tag{3.26a}$$

$$\theta_{unconstr} = (X^TX)^{-1}X^T\mathbf{f_{Ed}} \tag{3.26b}$$

where $\theta_{unconstr}$ is the unconstrained least square estimate obtained by QR factorization and $H^{-1} = X^TX$ is the inverse Hessian (Golub and Ortega, 1991), $A = \begin{bmatrix} -1 & -1 & \cdots & 1 & 1 \end{bmatrix}^T$ and $d = 1$.

$$k = \begin{cases} \tau + 1 & & \text{first model output} \\ \widetilde{N} \begin{cases} N & \text{if } n_d \geq 0 \\ N + n_d & \text{if } n_d < 0 \end{cases} & & \text{last model output} \end{cases} \tag{3.27}$$

where $\tau = max\{n_a, (n_b + n_d)\}$, τ values of data are used to initialize the system. In Eq. (3.27), first possible predicted model output is for $k = \tau + 1$ and the last predicted

model output is for $k = \widetilde{N} = N$ for causal system ($n_d \geq 0$) or $k = \widetilde{N} = N + n_d$ for non causal system ($n_d < 0$) (see Figure 3.5).

Thus in order to determine the NRMSE (see Eq. (3.23)), the error between the estimated $\mathbf{f_{Ed}}$ and CFD calculated $\mathbf{f_d}$ values of hydrodynamic forces, can be calculated using equations Eq. (3.28), Eq. (3.29) or Eq. (3.30) and Eq. (3.31). $\mathbf{X}$ can be written as Eq. (3.29) for Hammerstein model and Eq. (3.30) for KGP model (assuming $n_p = 2$).

$$\varepsilon = \begin{bmatrix} \varepsilon(1) & \varepsilon(2) & \cdots & \varepsilon(N) \end{bmatrix}^T \tag{3.28a}$$

$$\mathbf{f_d} = \begin{bmatrix} f_d(1) & f_d(2) & \cdots & f_d(N) \end{bmatrix}^T \tag{3.28b}$$

$$\mathbf{f_{Ed}} = \begin{bmatrix} f_{Ed}(\tau+1) & f_{Ed}(\tau+2) & \cdots & f_{Ed}(\widetilde{N}) \end{bmatrix}^T \tag{3.28c}$$

In Eqs. (3.29) and (3.30), $\underline{\underline{f_d(\tau)}} \cdots \underline{\underline{f_d(\tau+1-n_a)}}$ provides the initial guess values of the estimated dynamic forces, these values can be assumed "0" to avoid initial bias or can be taken from the training data. In order to obtain θ_{constr}, the parameters that minimize the least squares error are given by Eq. (3.31) after solving Eq 3.26.

$$\mathbf{X} = \begin{bmatrix} \underline{\underline{f_d(\tau)}} & \cdots & \underline{\underline{f_d(\tau+1-n_a)}} & s(\tau+1-n_d) & \cdots & s(\tau+1-n_d-n_b) \\ f_{Ed}(\tau+1) & \cdots & f_{Ed}(\tau+2-n_a) & s(\tau+2-n_d) & \cdots & s(\tau+2-n_d-n_b) \\ \vdots & \ddots & \vdots & \vdots & \ddots & \vdots \\ f_{Ed}(\widetilde{N}-1) & \cdots & f_{Ed}(\widetilde{N}-n_a) & s(N) & \cdots & s(N-n_b) \end{bmatrix} \tag{3.29}$$

$$\mathbf{X} = \begin{bmatrix} \underline{\underline{f_d(\tau)}} & \cdots & \underline{\underline{f_d(\tau+1-n_a)}} & f_d^2(\tau) & \cdots & f_d^2(\tau+1-n_a) & s(\tau+1-n_d) & \cdots & s(\tau+1-n_d-n_b)\dots \\ & & & & & & \dots s^2(\tau+1-n_d) & \cdots & s^2(\tau+1-n_d-n_b) \\ f_{Ed}(\tau+1) & \cdots & f_{Ed}(\tau+2-n_a) & f_{Ed}^2(\tau+1) & \cdots & f_{Ed}^2(\tau+2-n_a) & s(\tau+2-n_d) & \cdots & s(\tau+2-n_d-n_b)\dots \\ & & & & & & \dots s^2(\tau+2-n_d) & \cdots & s^2(\tau+2-n_d-n_b) \\ \vdots & \ddots & \vdots & \vdots & \ddots & \vdots & \vdots & \ddots & \vdots \\ f_{Ed}(\widetilde{N}-1) & \cdots & f_{Ed}(\widetilde{N}-n_a) & s(N) & \cdots & s(N-n_b) & f_{Ed}^2(\widetilde{N}-1) & \cdots & f_{Ed}^2(\widetilde{N}-n_a)\dots \\ & & & & & & \dots s^2(N) & \cdots & s^2(N-n_b) \end{bmatrix} \tag{3.30}$$

$$\theta_{constr} = \begin{bmatrix} a_1 & a_2 & \cdots & a_{n_p \times n_a} & b_0 & b_1 & \cdots & b_{n_p \times n_b} \end{bmatrix}^T \tag{3.31}$$

Dynamic order estimation

Based on the argument presented in Section. 3.3, that the current estimate of hydrodynamic force f_{Ed} is dependent on previous vaules of two variables (ζ and f_{Ed}), it is important to determine the weight of each variable. Being a discrete data model the weight can be attributed to the number of data points of each variable influencing the current value of the estimate. In Eq. (3.2), this is represented by the dynamical order of the equation n_a and n_b, implying that the f_{Ed} is a function of n_a number of outputs of f_{Ed} and $n_b + 1$ number of input of ζ values as shown in Figure 3.5. The flexiblity (ability to show complex behaviour) of the model increases with increase of the model order, where as very high orders limit the generalization on new data. Thus an ideal value of n_a and n_b should be determined. This ideal value is indicated by the fact that the model performance does not increase significantly by increasing the model order beyond that value (Isermann and Münchhof, 2011).

Time delay estimation

Another important paramerter to be determined is the one that indicates the phenomenone of causality. A system is causal if the output at current instant depends only on the present and past input where as in a noncausal system the output at current instant depends on the future input. Since the model is trained on the data obtained from physical system (training case), it is necessary to consider this effect when the physical system is not present (validation case). The presence of nonlinearity also influences this parameter. Hence the parameter n_d represents the input delay time and represents (for $n_d \geq 0$) the number of samples before the output reacts to the input (causal system). If $n_d < 0$ the system is noncausal and n_d represents the number of future input values, which influence the present value of the output (see Figure3.5).

The input delay time n_d and the dynamical order (n_a and n_b) are collectively estimated by measuring the error function from Eq. (3.23), by trial and error process on several ARX models. Ultimately, a combination of n_a, n_b and n_d is selected which results in lowest error in the estimate of ε.

3.6 Model Validation

In Section 3.1.2, it has been explained that model validation is the last and important step in the system identification process. This section highlights the process of model validation. Common methods utilised for model validation are prediction and simulation. In this section the difference between prediction and simulation is outlined with the help of Figure 3.6. Prediction is the process of forecasting a single value in future. For parameter identification, prediction steps are repeated multiple times with the knowledge of process input *e.g.* $\zeta(k-i)$ and process output *e.g.* $f_d(k-i)$. In simulation the model uses only the process input values (Nelles, 2001). When this prediction procedure is repeated for model identification, it is referred as training process.

In a case where the performance achieved using prediction on the training data is acceptable, a rigorous validation has to be done by testing the model on new data set. The model is validated by following a similar approach as prediction; but with a different set of input data, as the truth signal (output of CFD) is not utilized. This will be referred as simulation in this thesis. A nonlinear dynamic model can be used for the purpose of either prediction or simulation. The difference between training and simulation can be shown by following equations respectively:

$$f_{Ed}(k) = \gamma[f_d(k-1), \ldots f_d(k-n_a), s(k-n_d), s(k-n_d-1), \ldots. s(k-n_d-n_b)] \quad (3.32)$$

$$f_{Ed}(k) = \gamma[f_{Ed}(k-1), \ldots f_{Ed}(k-n_a), s(k-n_d), s(k-n_d-1), \ldots. s(k-n_d-n_b)] \quad (3.33)$$

In this thesis, the ultimate goal for the model is to perform simulation. The parameters required for simulation are obtained from the training, which requires repeated application of prediction algorithm. The results of simulation are validated against the process output for a different realization of process input. In the validation process the model has to predict the outcome of an experiment which was not used for the training. For doing so the model utilizes the simulation process shown in the diagram Figure 3.6. Even if the performance achieved on the training data is acceptable, without testing the model performance of new data the model cannot be accepted.

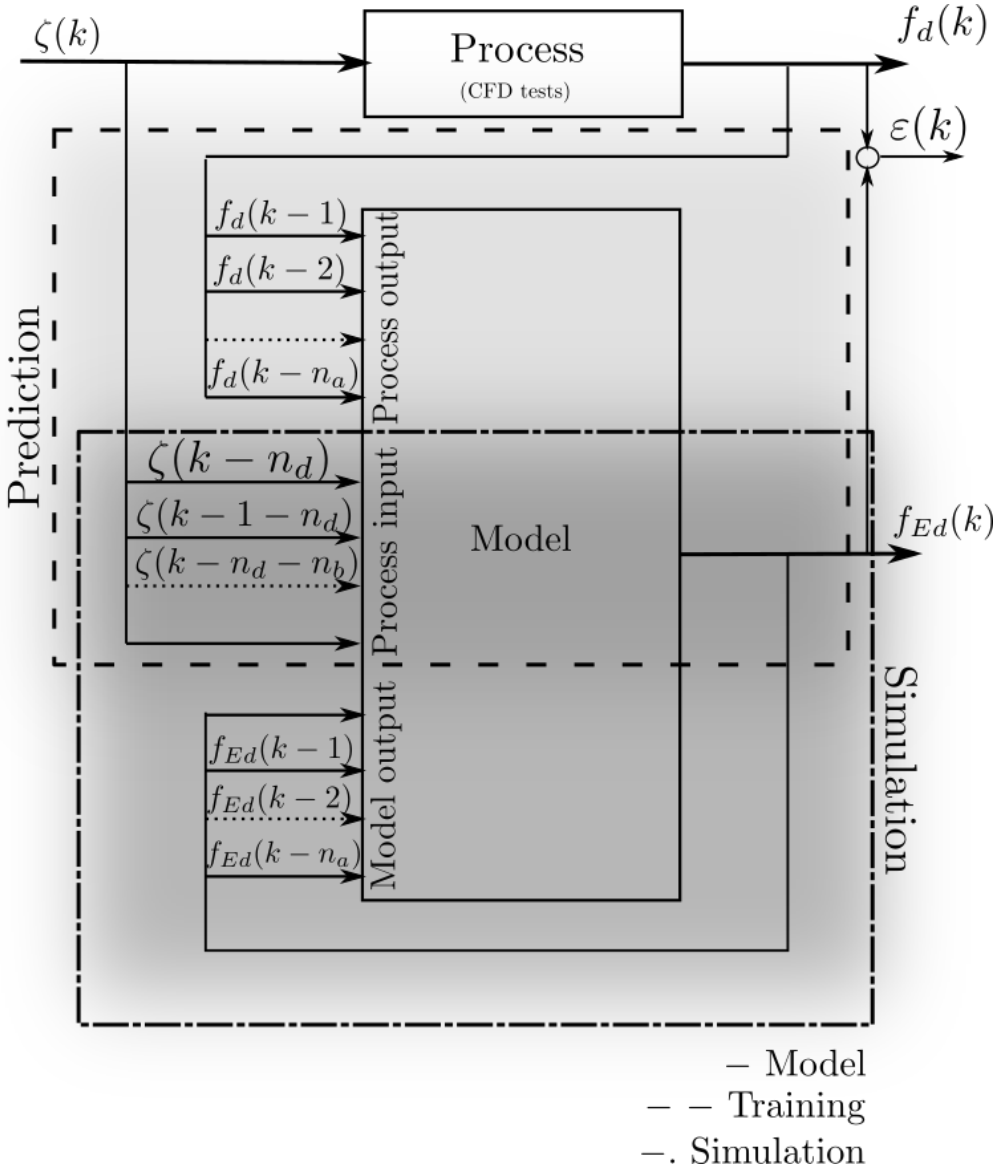

Figure 3.6: Process diagram representing difference between prediction and simulation. Basic difference between training and simulation is the input and output variables of the model. When a single value in the future is predicted using only the process input and output values it is prediction process, when this procedure is repeated for model identification, it is referred as training process but when model output is used instead of process output it is possible to predict multiple steps and this is referred as simulation.

3.7 Summary of the various candidate Data-driven models.

In this chapter, a new methodology for hydrodynamic parametric model identification is presented, which is based on the use of CFD-NWT data. The major improvement compared to previous work is the introduction of nonlinear hysteretic model as a stand alone model and also in the data-driven modelling frame work. Another more general improvement is increased modelling accuracy over linear potential theory models which are based on strong assumptions of absence of hydrodynamic nonlinear effects, such as viscosity, nonlinear restoring force and vortex shedding.

Table 3.1: Summary of input and output of each block

	Model	Static block		Rate dep. block		Dynamic block	
		Input	Output	Input	Output	Input	Output
State dep.	Hydrostatic	ζ	$f_{Es} = f_{Ed}$	–	–	–	–
	Hydrostatic + Bouc-Wen	ζ	f_{Es}	$\zeta,\ \dot{\zeta},\ \ddot{\zeta}$	$f_{Ee} = f_{Ed}$	–	–
Training needed	Hammerstein	ζ	f_{Es}	–	–	f_{Es}	f_{Ed}
	Rate dep. Hammerstein	ζ	f_{Es}	$\zeta,\ \dot{\zeta},\ \ddot{\zeta}$	f_{Ee}	$f_{Es} + f_{Ee}$	f_{Ed}
	Rate dep. KGP	ζ	f_{Es}	$\zeta,\ \dot{\zeta},\ \ddot{\zeta}$	f_{Ee}	$f_{Es} + f_{Ee}$	f_{Ed}

A summary of the models used in this chapter and analyzed in Chapter 4 is presented in Table 3.1. The input and output of individual blocks employed in these models is also compared. The identification of the entire block oriented framework is divided into identification of the parameters required in individual block. Each block will require a set of data, which should excite the system inorder to obtain all the required information. Thus a diverse set of data should be used.

Chapter 4

Numerical wave tank trials

The use of a NWT to replicate physical tank experiments was discussed in detail in Chapter 2 and it was illustrated that NWT qualifies as a means to generate data that can be used in data-driven models. Another important conclusion was that the heave plate on WEC B caused a nonlinear relationship between input state variables and output hydrodynamic force, which was not seen for WEC A. These NWT trials were performed either by using monochromatic waves or quiescent fluid as discussed in Sections. 2.3.2 and 2.3.3 respectively. The hydrodynamic forces thus obtained were validated against the results obtained from physical tank tests utilizing the same strategy. Since the validation process increased confidence in CFD experiment design, this approach can be extended to generate data for data driven models.

This chapter presents the experiment design and data generation process, which will be utilized for identification of the model parameters for the block oriented models discussed in Chapter 3. A brief outline of NWT trial involved in data generation is provided Section 4.1. The WEC and domain details along with the input wave characteristics are also discussed in the same section. The details of the NWT trials involved in data generation are discussed in Sections 4.2 and 4.3. The characteristics of the flow field in hydrodynamic trials are discussed in Section 4.4.

4.1 NWT trials for data generation

NWT trials in this thesis are used to identify different types of model components and are classified based on the environmental and input-output conditions as represented in Figure 4.1 and Table 4.1. This classification criterion leads to primarily two types of

NWT trial, *viz.* hydrostatic and hydrodynamic NWT trial. NWT trials provide data that can be used to determine the relationship between freesurface and hydrostatic force can be achieved by displacing the spar in a quasi-static manner and recording the force on it for discrete draft values. This experiment will be here-after refereed as hydrostatic NWT trial. A hydrodynamic NWT trial is done in the presence of transient input waves to establish a relationship between the state variables and the dynamic force experienced by the spar. These state variables are either the position, velocity and acceleration of the freesurface for stationary spar or relative values of position, velocity and acceleration for moving spars.

Assuming that the hydrodynamic force f_d thus obtained has a component of static contribution, the effects of which have been identified in the hydrostatic test, it can be substracted from the measured hydrodynamic force. This component of force will be referred as excitation force f_e (*i.e.* $f_e = f_d - f_s$).

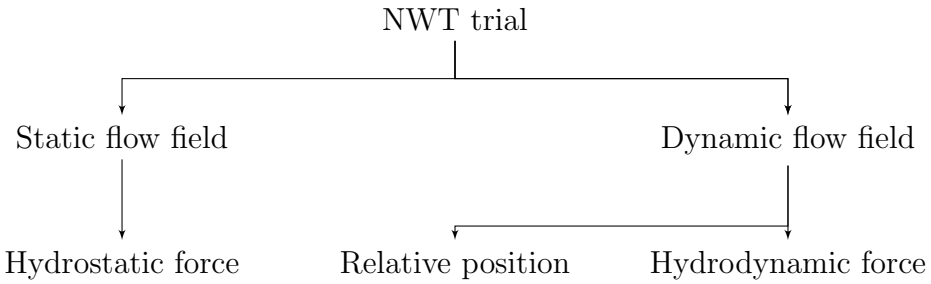

Figure 4.1: Classification of experiments for data generation. The input and output of these experiments are tabulated in Table 4.1

Table 4.1: Characteristics of various NWT simulations used for data generation

Flow field	Static	Dynamic	
Exp. type	Hydrostatic	Hydrodynamic	
Input	$\zeta_{max} > z > \zeta_{min}$	H_s, T_p	H_s, T_p, z
Output	f_s	η	ζ, f_d

While most models of WEC (Bacelli et al., 2017; Giorgi et al., 2015, 2016b) use a formulation with surface elevation as input, in this study the model uses relative position of spar (*w.r.t* free surface) for broader representation of operating conditions. The NWT trials required for the identification of various parameters and the

resulting parameters of these experiments are shown in Figure 4.1. The input to the experiments and the obtained output for the subsequent identification experiments are tabulated in Table 4.1.

4.1.1 Spar geometry and CFD domain details

Geometries of some hydrodynamic significance to wave energy conversion have been considered in this study. As it has been discussed in Chapter 2 that a 3D CFD simulations at wave tank scale is beyond practical implementation, a 2D analysis should be adopted. 2D geometry provides the characteristics in the hydrodynamic force that were seen for the 3D geometry. This implies that the geometry chosen is such that the flow field developed during the operation of the device is similar to that developed by the operation of 3D SRPA with heave plate. Thus in the current work infinitely long cylinder having vertical cross-sections of a heave plate at the end of rectangular cylinder (shape of an inverted T), hereafter known as Heave Plate (HP) cylinder will be considered. In order to establish the importance of rate dependent block (Bouc-Wen model) in the context of the HP cylinder and to compare the performance of the basic model structure on which the proposed model is build, a simpler 2D square cylinder is also considered. The sketch and dimensions of the spars used are as shown in Figure 4.2.

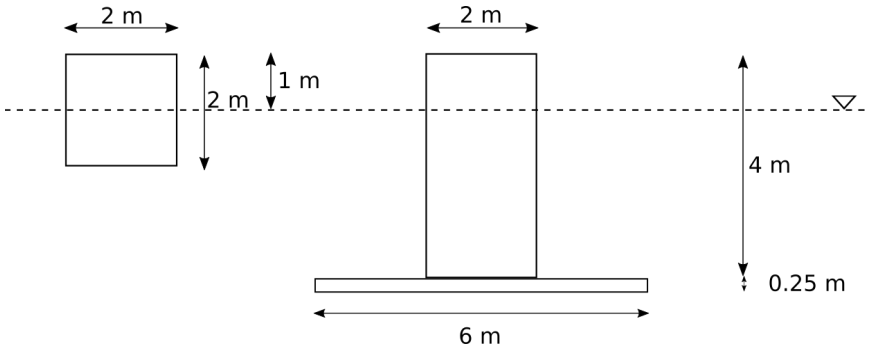

Figure 4.2: Schematics of 2D prismatic test geometries: a square cylinder and a Heave Plate (HP) cylinder

Though only 2D geometries with single Degrees of Freedom (DOF) were considered in this study, this methodology can be easily extended to 3D geometries. In the current study, the effect of fluid motion in only the plane of oscillation (xy plane) affects the results.

The setup of 2D numerical tank requires cells of unit thickness in the third dimension and a symmetry boundary condition is imposed on the the cell faces in xz plane. The domain dimensions and the associated structured mesh around the WEC is shown in Figure 4.3. Two different domains and mesh were considered for the hydrostatic and hydrodynamic experiments. The dimensions of the tank are based on the requirement of the wave absorption at the tail end of NWT and previous work of Giorgi et al. (2015, 2016a).

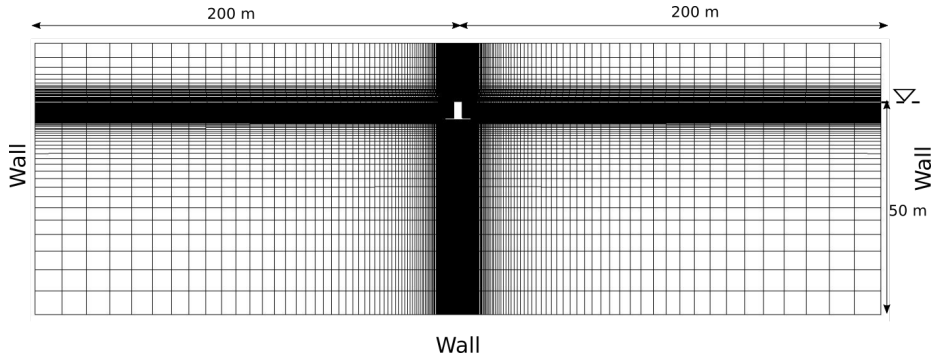

(a) Mesh and domain for hydrostatic experiment

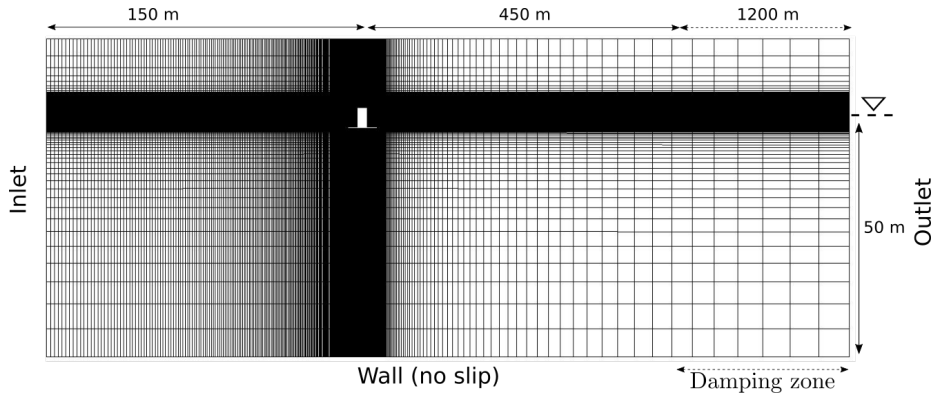

(b) Mesh and domain for hydrodynamic experiment

Figure 4.3: Domain dimensions and mesh for NWT trials. The WEC was placed equidistant from tank walls for hydrostatic test. Due to the requirement of wave damping zone at the tail end of the NWT the WEC was placed closer to the wall in the upstream than in the downstream in hydrodynamic test

The spar is placed at 100 m, equidistant from both the ends (*i.e.* max and min x coordinate) for the hydrostatic test. Since hydrostatic experiments are a quasi-static process: body is moved very slowly so as not to generate surface waves. For the case of hydrodynamic test the spar is placed at 150 m from inlet and 450 m from outlet to allow wave generation and absorption. In all the experiments, the numerical tank

is 50 m deep. The discussed in Section 2.2, one of the advantages of NWT is that reflections from tank walls can be controlled in multiple ways. In this work the tank dimensions are chosen such that the walls are far away from the WEC and numerical damping is applied at the tail end of the tank, to ensure no wave are not reflected.

4.1.2 Grid sensitivity analysis

A uniform grid with square cells in the entire domain is not desirable, due to the high cell count. It was decided to reduce the number of required cells by using different refinement levels and cell size grading for the discretisation of the NWT. Eight meshes with the same layouts but varying degree of resolution were considered. The layout is shown in Figure 4.4. The cells with largest size are situated next to the bottom of the tank in the transverse direction and at the far field damping region next to the outlet boundary in the longitudinal direction. The size of the largest cell height is represented by Δ. The smallest cells $\Delta/2^4$ are placed close to the free surface. With increasing cell sizes in the order of 2^n where $n = 3, 2, 1$ away from the free surface. Each layer has a thickness of wave height $H/2$, above and below the mean free surface. A gradient of 0.87 is used to decrease the size of cells away from the bottom towards the freesurface and, a gradient of 0.91 was applied in the direction from the outlet to the simulation zone. The details of the mesh and results of the sensitivity test are tabulated in Table 4.2. The details of the convergence metrics chosen for the sensitivity study and the mathematical formulation of the three error metrics used in the study can be found in Appendix A. The three metrics are *viz* Metric-1 is grid

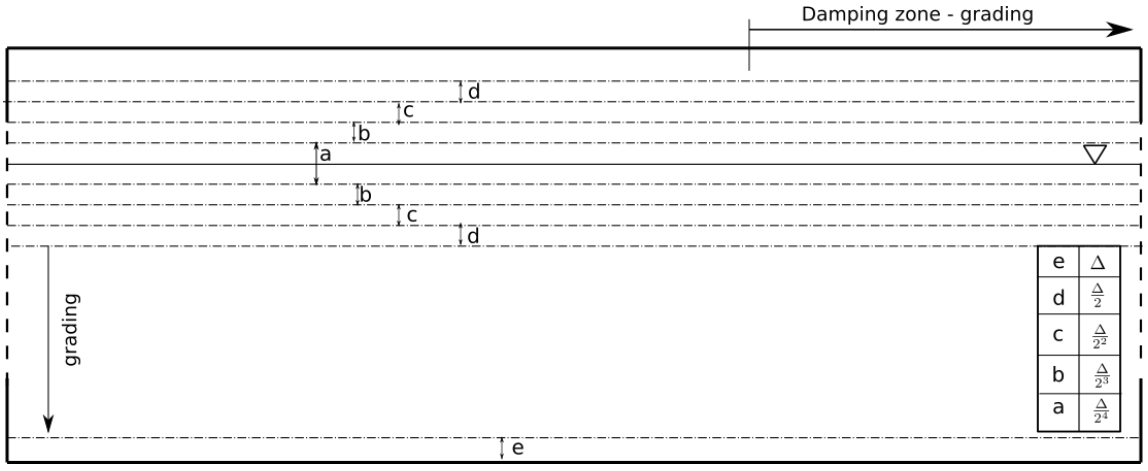

Figure 4.4: Schematic of mesh sizes used in the sensitivity study. Δ represents the largest cell size along the depth of the NWT

Table 4.2: Grid independence study on 2D NWT. Monochromatic waves of wave height $H = 5\ m$and wave length $\lambda = 300\ m$ were used for 700 s of simulation. Mesh-c has the coarsest resolution and Mesh-f has the finest resolution

Mesh Index	Division^{+}		Total no. of cells	No. of cells		Convergence	(%)	
	x	y		CPH$^{\&}$	CPL*		U	$d\bar{H}$
c	50	30	12723	11	120	–	–	–
1	55	35	16360	13	140	Monotone	−1.035	−0.688
2	67	28	14928	15	28	Oscillatory	11.4	3.61
3	67	40	14512	15	40	Oscillatory	10.9	2.97
4	67	40	21904	15	160	Monotone	−1.58	−1.05
5	80	45	30395	18	180	Monotone	−6.24	−4.08
6	90	55	40210	20	220	Oscillatory	14.1	7.12
f	105	60	51170	24	240	–	–	–

Number of divisions before refinement
No of cells per wave height at the free surface
No of cells per wave length at the free surface

uncertainty. Metric-2 is the relative deviation of the phase averaged wave height for various meshes with respect to the mean wave height of the finest mesh. Metric-3 is the mean error and standard deviation of the measured phase averaged wave height. From Table 4.2, it can be seen that the values of U (Metric-1) and $d\bar{H}$ (Metric-2) are higher by an order of magnitude for Mesh-2, Mesh-3 and Mesh-6 when compared to Mesh-1, Mesh-4 and Mesh-5 for which monotonic convergence is obtained. Thus, the meshes for which oscillatory convergence is obtained are not analyzed further. In order to decide the final grid distribution Mesh-1, Mesh-4 and Mesh-5 are further analyzed by evaluating the wave damping in NWT for these meshes.

The capability of absorbing waves travelling from the generation boundary towards the far field boundary is crucial for an efficient NWT. The far field boundary must absorb the outgoing waves to prevent undesired reflections back into the NWT simulation zone, contaminating the generated wave field. Metric-3 is used to evaluate the consistency of the wave field along the length of the NWT. Table 4.3 shows the relative error at two different locations $x/\lambda = 1$ and $x/\lambda = 1.5$ in the tank. A consistent value of error at both the locations is desired. It is also expected that under ideal condition the upper and lower bounds of errors are equal. From Table 4.3, it can be seen that the values of errors are higher for the coarsest and the finest mesh. The inconsistency in the error values at both the locations for Mesh-1 is evident along

Table 4.3: Relative error $\epsilon_{\bar{H}}$ between target and resulting wave height $\pm$ standard deviation at $x/\lambda = 1$ and $x/\lambda = 1.5$ in the tank. Mesh-c has the coarsest resolution and Mesh-f has the finest resolution

Mesh Index	$x/\lambda = 1$		$x/\lambda = 1.5$	
	$\epsilon_{\bar{H}^+}$	$\epsilon_{\bar{H}^-}$	$\epsilon_{\bar{H}^+}$	$\epsilon_{\bar{H}^-}$
c	-7.7	-9.4	-3.7	-5.25
1	3.3	2.0	-0.09	-2.0
4	3.4	1.2	2.6	-0.5
5	0.44	-2.1	0.72	-4.0
f	4.1	2.7	1.6	0.34

with positive and negative bias. The error values for Mesh-5 are smaller compared to the errors for Mesh-4.

Considering the values of Metric-1, Metric-2 and Metric-3 for Mesh-1, Mesh-4 and Mesh-5 and keeping in mind the computational expense, it was decided to use the grid parameters corresponding to Mesh-4 for further analysis.

4.1.3 Input signal characteristics (Sea state)

For the NWT hydrodynamic trial a list of wave characteristics are provided as input to OpenFOAM code. The provided characteristics are wave model, wave length, amplitude, phase and angle. The characteristics have been generated using an Matlab script developed in-house, which utilizes the Wave Analysis for Fatigue and Oceanography (WAFO) toolbox. WAFO is a toolbox of Matlab routines for statistical analysis and simulation of random waves and random loads. The characteristics of sea state in terms of $H_s$and T_p are specified to this script, and it generates OpenFOAM readable file with a list of required parameters (wave model, wave length, amplitude, phase and angle). The input sea state used in this paper has a JONSWAP spectra characterized by $H_s = 0.5\ m$ and $T_p = 10\ s$. The sea state has been obtained as multisine signal selecting random phases. An example of the spectral content used in thesis is shown in Figure 4.5. For each oscillation characteristics three different realizations have been generated and utilized with each geometry, they will be referred as $R1$, $R2$ and $R3$.

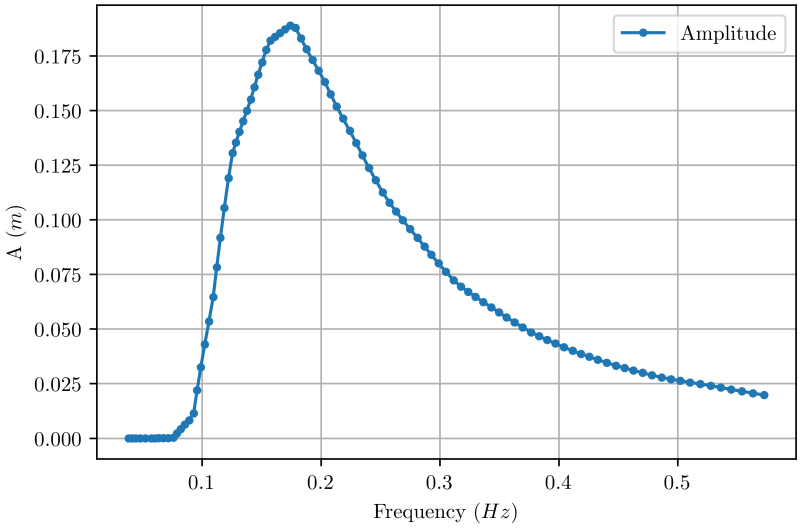

(a) Amplitude-frequency distribution

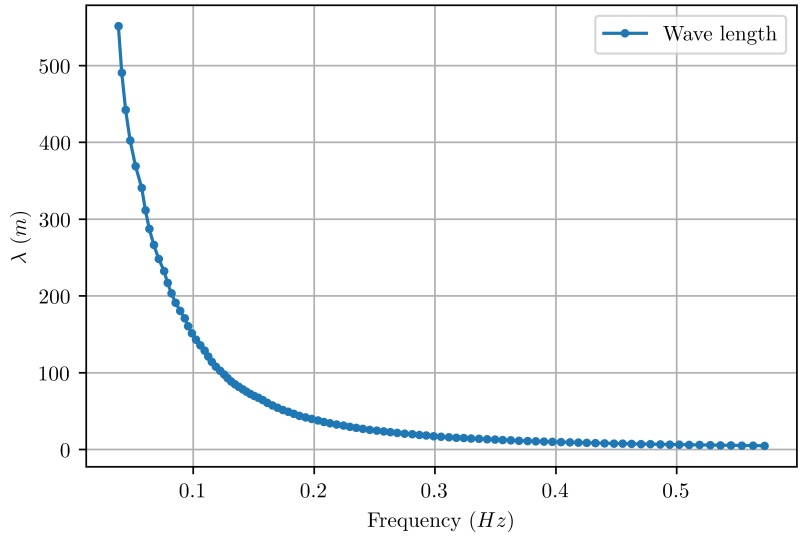

(b) Wavelength-frequency distribution

Figure 4.5: Distribution of characteristics of input signal for $H_s = 0.5\ m$ and $T_p = 10\ s$

4.2 Hydrostatic NWT Trail

The objective of hydrostatic experiment is to determine the parameters governing the relationship between the input and output of static block. This is represented by function $r(\cdot)$ in Eq. (3.7). In this experiment, the spar is submerged in a nearly static flow field condition such that no dynamic effects are present. The spar initialized to oscillate at a frequency of 8×10^{-4} Hz and amplitude of 20 m, but the simulation was stopped in 20 s. The details of hydrostatic experiments are also tabulated in Table 4.4. In this time the spar moved by 2 m distance in the direction of submergence. Two vectors are produced by this experiment one containing the hydrostatic force f_s on the spar and another position of centroid of spar with respect to water surface The change in the hydrostatic force with respect to relative height measured from the centroid of the square and HP cylinder is in Figure 4.6. In this experiment, the forces on spar were recorded at an interval of 0.002 s, thus during submergence each value of time corresponds to a unique value of relative height. The x-axis of the plot shows mapped values of relative height ζ for the corresponding value of time. The identification procedure of this test is discussed in Section 3.5.2, and the case study explaining the process is discussed in Section 5.2

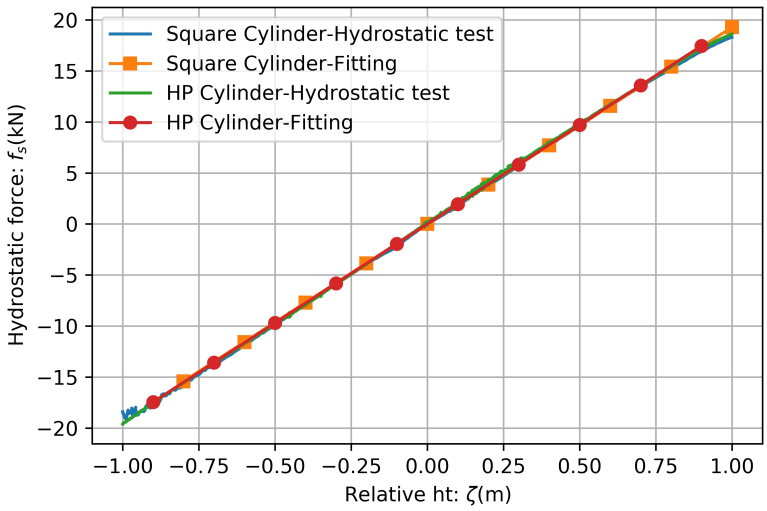

Figure 4.6: Results from the hydrostatic test and fitting of the static curve. The section of curve shown here $\zeta = -1, 1$ represents the spar length that was submerged in this experiment

For geometries with straight wall the hydrostatic curve can be obtained from

Archimedes' principle without the requirement of expensive CFD simulations. However, the purpose of this exercise is to lay out a general methodology for determination of the hydrostatic curve for SRPAs with wall of arbitrary shapes.

4.3 Hydrodynamic NWT Trail

The hydrodynamic force f_d and the excitation force f_e corresponding to the relative position ζ on WEC is calculated from the hydrodynamic experiment. The results from this experiment are used for parameter identification of rate dependent block (refer Section 3.5.3) and the dynamic block (refer Section 3.5.4).

In order to determine ζ the wave height η has to be determined first. One way to find the wave height in a transient CFD simulation is by placing probes around the spar in dynamic test and interpolating the wave heights. The values of wave heights thus obtained will be influenced by diffraction, scattering as well as radiation, particularly when the spar has a damper plate placed close to the free surface. Thus in order to avoid the effect of above mentioned phenomenon and since repeatability of the environmental conditions is ensured in a numerical tank, this thesis proposes performing the hydrodynamic experiment with a wave probe placed at the location of spar. The time series of signal that are generated from the hydrodynamic experiments are enumerated below.

1. The wave probe provides the time series TS-1 of wave elevation at the location of spar. This time series is presented in Figure 4.7a

2. The position signal generated by monochromatic oscillation of HP cylinder is referred as TS-2 signal, this signal is a sinusoid of amplitude and frequency presented in Table 4.4.

3. The superposition of TS-1 and TS-2 produces TS-3, which is the time series of relative position ζ of spar. This signal is shown in Figure 4.7b.

The relative position is thus extracted from a difference of two signals gathered independently. In the current study, HP spar is forced to oscillate with frequency of $\omega = 1.25\ rad/s$ and with three different amplitudes 0.25 m, 0.15 m, and 0.05 m. Fourth case with a stationary spar is also analyzed. The details of various NWT trials and test cases analyzed are tabulated in Table 4.4. The relative position of the

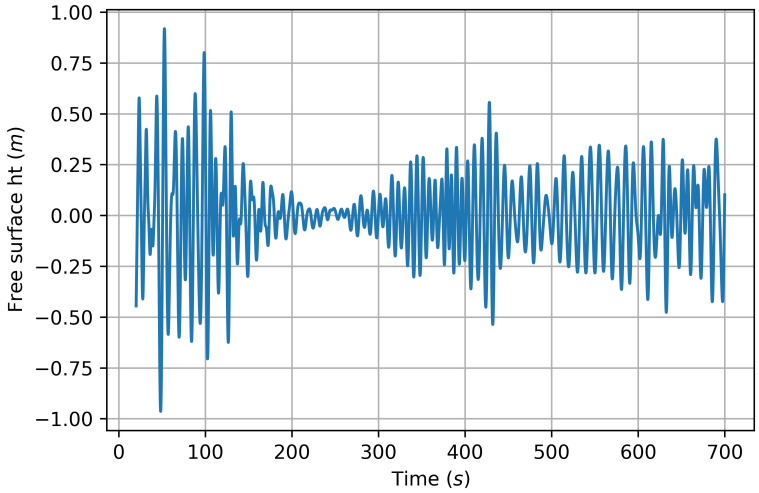

(a) Freesurface height at spar location (TS-1)

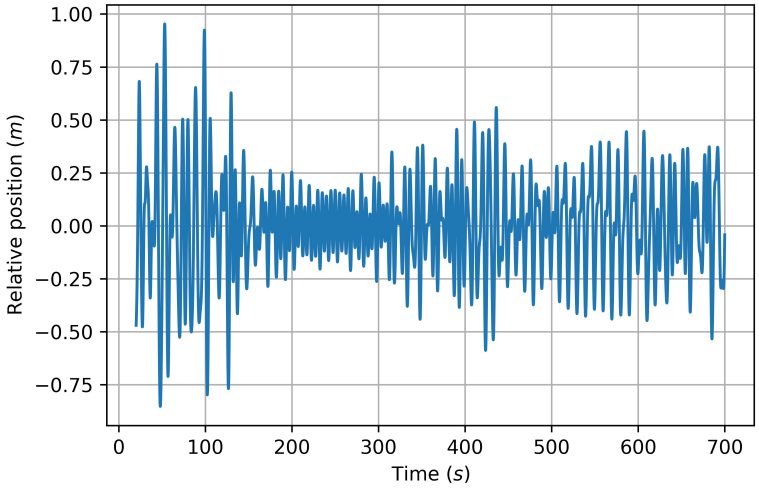

(b) Relative height at spar location (TS-3)

Figure 4.7: Free surface height (η) and relative height (ζ) from dynamic test for $R2$ realization for HP oscillating at 0.15 m and 1.25 rad/s

spar is same as the wave elevation TS-1 if the spar is stationary, otherwise relative position is the time series TS-3.

Once the relative position of the spar is determined the CFD hydrodynamic experiment is repeated with spar at the location of the wave probe. Spar is either forced to oscillate periodically at the amplitude and frequency tabulated in Table 4.4 or remain stationary in a dynamic flow field depending on the case under study. The excitation force f_e is also calculated from this test by subtracting the hydrostatic force f_s from the total measured hydrodynamic force f_d. The hydrostatic force is obtained by the knowledge of function $r(\cdot)$ obtained from identification of static block (refer Sections 3.5.2 and 5.2). The hydrostatic force corresponds to the relative position of the body with respect to the free surface in the presence of waves.

As the hydrostatic force is obtained from a quasi-static experiment, the excitation force is inclusive of all the nonlinear forces due to oscillation of heave plate and the viscosity of water. The identification of the rate dependent block utilizes the excitation force, and the procedure to obtain the constants in Bouc-Wen model are described in Section 3.5.3 and demonstrated in Section 5.3, respectively.

Table 4.4: Characteristics NWT trials of various test cases used for data generation. All the hydrodynamic experiments have been conducted for 700 s in order to capture several cycles of the lowest frequency waves in the spectrum.

<table>
<tr><th rowspan="2">Experiment type</th><th colspan="2">Spar oscillation</th><th colspan="2">Sea state^{+}</th><th rowspan="2">Duration</th></tr>
<tr><th>amp
(m)</th><th>ω
(rad/s)</th><th>H_s
(m)</th><th>T_p
(s)</th></tr>
<tr><td>Hydrostatic</td><td>20</td><td>0.005</td><td colspan="2">-</td><td>20</td></tr>
<tr><td rowspan="5">Hydrodynamic$^{\&}$</td><td colspan="2">0.0</td><td rowspan="5">0.5</td><td rowspan="5">10</td><td rowspan="5">700</td></tr>
<tr><td>0.05</td><td rowspan="3">1.25</td></tr>
<tr><td>0.15</td></tr>
<tr><td>0.25</td></tr>
<tr><td>Hydrodynamic*</td><td colspan="2">Fixed wave probe</td></tr>
</table>

$^{+}$ 3 hydrodynamic CFD simulations for 3 sea state realizations $R1$, $R2$ and $R3$
* panchromatic free surface height at the location of wave probe generates TS-1 signal
$^{\&}$ the position signal generated by monochromatic oscillation of HP cylinder generate TS-2 signal

The HP cylinder discussed in this chapter is a 2D simplification of the 3D WEC B discussed in Chapter 2. It is expected that the flow fields around the HP cylinder and WEC B are similar in characteristics.

4.4 Characteristics of the 2D WEC Fluid Structure Interaction

The characteristics of the flow field in hydrodynamic trials are analyzed to find similarity with the characteristics in the wave force that were seen for the 3D WEC B geometry. Figure 4.8 shows the process of vortex generation around the HP cylinder oscillating at $amp = 0.25\ m$ and $amp = 0.05\ m$, and common frequency $= 1.25\ rad/s$ in a panchromatic wave field for realization $R1$ during one cycle of oscillation. The images corresponds to instants of time that are 1/4 period of the HP oscillation. Figure 4.8a, 4.8b show that when the cylinder reaches the top dead centre and starts moving down the plate tries to displace the water below it, which quickly fills up the vacuum created above the plate from the previous cycle (shown by the direction of velocity vector). The asymmetry in the pressure field is the result of the dynamic wave field, and the low pressure region on the left of the cylinder is due to the wave trough. On the right of the cylinder's central axis a rolled up vortex ring, which was formed below the plate's bottom edge during the previous ascent, is fully developed has moved upwards. The vortex developed on the right of the cylinder shown in Figure 4.8a has diffused in Figure 4.8c and the small eddy at the edge of plate on the left has developed into a larger eddy forming a pair with existing vortex. This is not true for the HP cylinder oscillating at lower amplitude as the pair of vortices on the right of cylinder in Figure 4.8b has developed into three vortex in Figure 4.8d. The pair of vortices in the left of HP cylinder in Figure 4.8c develop into three vortices system on the early upward stroke of HP cylinder, as shown in Figure 4.8e, whereas the three vortex system in Figure 4.8d develops into four vortices in Figure 4.8f. These vortices move close to the free surface as shown in Figure 4.8g when compared to those in Figure 4.8h, as the incoming crest increases the hydrostatic pressure on the left side of the cylinder. Figure 4.8 shows that there are clearly changes in the pressure distribution that manifest due to past motions.

Earlier studies and visualizations on shedding of vortices from isolated oscillating sharp edges showed that vortices shed at each half cycle formed pairs that convected away from the edge (Graham, 1980). Another study on oscillating spar columns (Tao et al., 2000), showed that the first vortex formed in an up stroke depleted its strength rapidly due to diffusion, and was not able to convect away from the edge. Unlike the current analysis, these previous studies were done in a quiescent fluid condition and it is expected that the presence of panchromatic wave field will show unique

vortex behaviour on each cycle of spar oscillation. It is difficult to generalize the vortex shedding characteristic, due to combination of spar oscillations along with the panchromatic wave field.

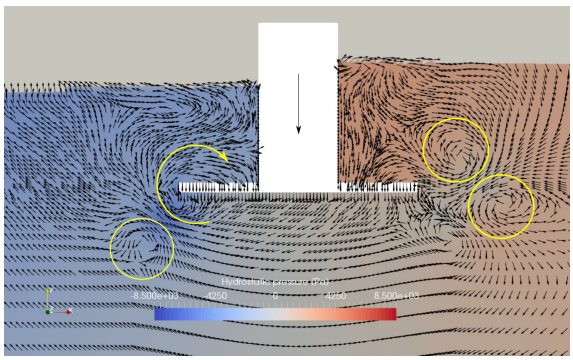

(a) $amp = 0.25 : \ 100 + \frac{T}{4} \ (s)$

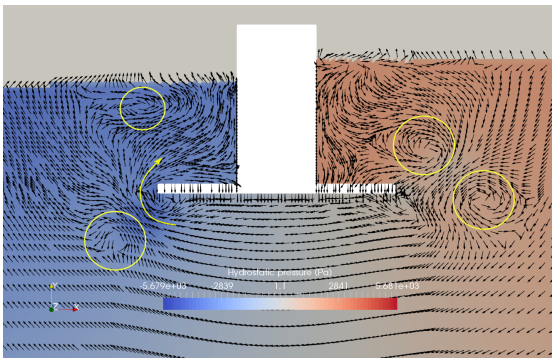

(b) $amp = 0.05 : \ 100 + \frac{T}{4} \ (s)$

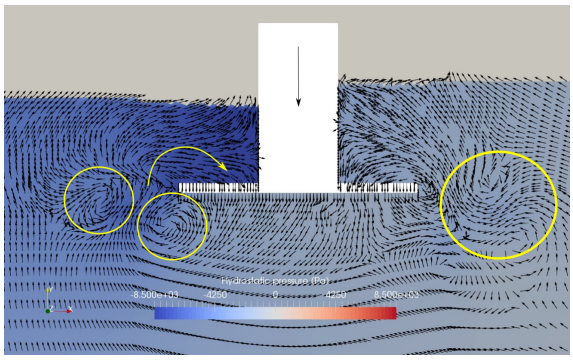

(c) $amp = 0.25 : \ 100 + \frac{T}{2} \ (s)$

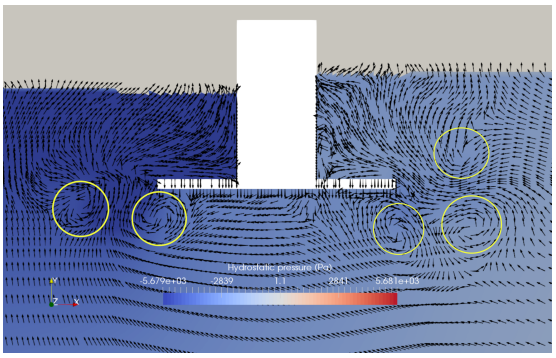

(d) $amp = 0.05 : \ 100 + \frac{T}{4} \ (s)$

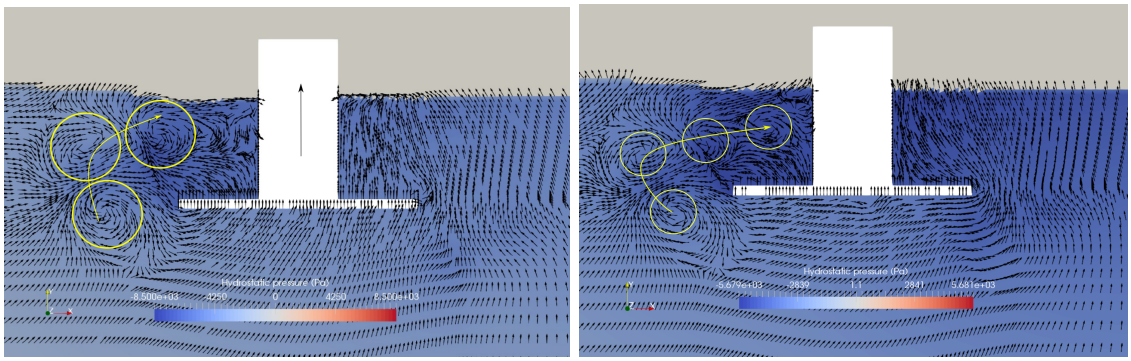

(e) $amp = 0.25 :\ 100 + \frac{3T}{4}\ (s)$ (f) $amp = 0.05 :\ 100 + \frac{3T}{4}\ (s)$

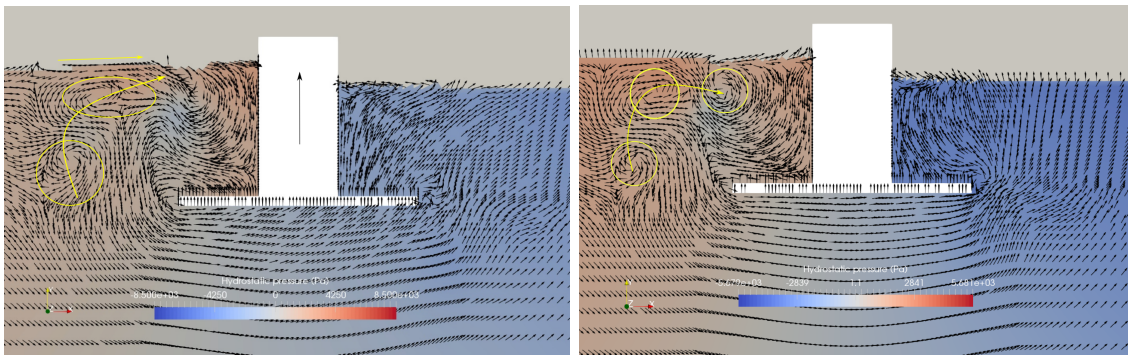

(g) $amp = 0.25 :\ 100 + T\ (s)$ (h) $amp = 0.05 :\ 100 + T\ (s)$

Figure 4.8: Flow field around HP cylinder oscillating at 0.25 m and 1.25 rad/s for $R1$ realization of sea state

Chapter 5

Identification of data driven models for Heave Plate (HP) Spar geometry in irregular waves

In Chapter 3, the framework for the data driven modelling technique was discussed in detail. The current chapter demonstrates application of the approach using CFD based Numerical Wave Tank (NWT) discussed in Chapter 4 as the source of data for identifying model parameters and for the training procedure. The identification procedures for the block oriented models were discussed in Section 3.5. These procedures are explained for each test case in Sections 5.2, 5.3 and 5.4. The results are discussed in Section 5.5.

5.1 Overview

A summary of parameters that must be obtained from the identification of sub-models is tabulated in Table 5.1. Three different linear and nonlinear discrete time, data-driven models *viz.* Hammerstein, rate dependent Hammerstein and rate dependent KGP model are compared in this work.

The structure of each model is based on combination of two or three different blocks. Each block is either based on some physical structure or are purely data-driven. A static block consisting of hydrostatic model and a dynamic block consisting of black-box ARX model is common to all data-driven models analyzed. This model is known as Hammerstein model. An additional block consisting of Bouc-Wen

Table 5.1: Summary of identification procedure, identified parameters, input variables required and composition of internal signal

	Model	Identified block			Validation	Internal signal s	Test cases[+*]
		Static	Rate dep.	Dynamic	Input sea state $R3$ (TS-3)[$]		
		Identified parameters					
		$\mathbf{C}$	$a,\ b,\ c$ $\alpha,\ \beta,\ \gamma$	$n_a,\ n_b,$ n_d			
		Sea state realizations[&] used					
		-	$R2$	$R1$			
State dep.	Hydrostatic	✓	-	-	ζ	-	HP
	Hydrostatic + Bouc-Wen	✓	✓	-	$\zeta,\ \dot{\zeta},\ \ddot{\zeta}$	-	HP
Training needed	Hammerstein	✓	-	✓	ζ	f_{Es}	HP Square
	Rate dep. Hammerstein	✓	✓	✓	$\zeta,\ \dot{\zeta},\ \ddot{\zeta}$	$f_{Es} + f_{Ee}$	HP
	Rate dep. KGP	✓	✓	✓	$\zeta,\ \dot{\zeta},\ \ddot{\zeta}$	$f_{Es} + f_{Ee}$	HP

[+] For HP cylinder 1 test case for fixed cylinder and 3 cases for oscillating cylinder at $\omega = 1.25\ rad/s$ and amplitude $= 0.05\ m,\ 0.15\ m,\ 0.25\ m$ were analyzed

[*] For square cylinder 1 test case for fixed cylinder was analyzed

[&] $R1,\ R2$ are used for identification and $R3$ is used for validation

[$] TS-3 is time series of relative position generated by superposition of TS-1 and TS-2, which are time series of freesurface ht and spar oscillation respectively

model is applied to the basic Hammerstein model resulting in two rate dependent data driven models known as rate dependent Hammerstein and rate dependent KGP model. These models differ in the structure of dynamic block as the rate dependent KGP model uses the nonlinear input-output relationship in the dynamic block. The dynamic block (ARX or KGP) is tasked with making up the difference observed in the internal signal and CFD generated hydrodynamic force. Two additional models which are dependent on the state are also assessed.

These models have been compared on their validation capabilities of hydrodynamic forces on four cases of fixed and oscillating HP cylinders. The proposed rate dependent models have been built on the foundation of existing Hammerstein model. By providing a comparison between hydrodynamic force on fixed square cylinder and fixed HP cylinder predicted by Hammerstein model, the requirement of rate dependent models to model HP spars will be firmly established. Since the purpose of using square cylinder was only to validate and compare the accuracy of the code developed to already published result, only Hammerstein model was analyzed for fixed square cylinder. Whereas for the HP cylinder all the three models were considered.

5.2 Static block identification

The identification of static block has been discussed in detail in Section 3.5.2. The current section demonstrates the methodology to determine the hydrostatic coefficients $\mathbf{C}$ in Eq. (3.15) for a square cylinder and a HP cylinder. These coefficients are determined from the results of hydrostatic experiment discussed in Section 4.2. The value of the static block parameter n_c is 1, and the values of the fitting coefficients $\mathbf{C}$ for the square cylinder and the heave plate cylinder are 19.28 kN/m and 19.4 kN/m, respectively. The hydrostatic coefficients are dependent on the geometry, and will be same for all the cases pertaining to a particular geometry. From the shape of spar and corresponding test results, it can be concluded that the value of $n_c = 1$ is expected due to the straight walls of spar and therefore linear increment in the hydrostatic force. Once the parameter n_c has been determined based on Section 3.5.2, the estimated value of static force $f_{Es}(k)$ can be calculated with the knowledge of relative height $\zeta(k)$. Though the value of $n_c = 1$ indicates that a linear model is sufficient, a nonlinear model is also developed for geometries which do not have straight walls at the interface.

5.3 Rate dependent block identification

As shown in Table 5.1, the rate dependent block consists of the Bouc-Wen model that is used only for analyzing test cases with HP spar. Utilizing the test results from the hydrodynamic tests described in Section 4.3 and the strategy outlined in Section 3.5.3, the identification of parameters of the rate dependent block are performed using the PSO algorithm (refer Section 3.5.3). The hydrodynamic force f_d obtained from the hydrodynamic experiment using sea state realization $R2$ and the values of hydrostatic coefficients $\mathbf{C}$ obtained from identification of static block are used inorder to determine the excitation force f_e, ($f_e = f_d - f_{Es}$). f_{Es} is estimated hydrostatic force on spar for sea state realization $R2$. The excitation force f_e is used to calculate the seven parameters of the Bouc-Wen model using Eq. (3.9), and the PSO optimization algorithm.

The cost function is defined as the difference between the estimated value to the excitation force f_{Ee} and the CFD obtained value f_e (refer Eq. 3.18). The values of the coefficients thus obtained for for the HP cylinder oscillating with a frequency of 1.25 rad/s and amplitudes of 0.0 m, 0.05 m, 0.15 m and 0.25 m for sea state realization $R2$ are tabulated in Table 5.2.

The values of parameters thus obtained were substituted in Eq. (3.9) along with the time series of ζ, $\dot{\zeta}$ and $\ddot{\zeta}$. The values of excitation force $f_{Ee}(k)$ were determined for training signal $R1$, but the parameters of rate dependent block were identified using realization $R2$. The estimated values of the excitation force for the oscillating HP cylinder are plotted along with the CFD generated values in Figure 5.1a and the comparison between the amplitude spectrum of estimated excitation force signal and CFD generated excitation force signal is shown in Figure 5.1b. The NRMSE between the excitation forces and MAPE between the signals of amplitude spectrum for the entire signal of 600 s is shown in respective plots.

The excitation force is expected to have a nonlinear force relationship with the relative velocity $\dot{\zeta}$. It is also expected that this nonlinear force relationship can be expressed by hysteresis plot. To verify this, the true excitation force obtained *via* the NWT is plotted with respect to relative position and relative velocity for the entire 700 s signal and shown in Figure 5.2. These plots are for the realization $R1$ when the HP cylinder is oscillating with $amp = 0.05$ m. It can be seen that the excitation force and relative velocity relationship follows a hysteresis curve implying that the maximum relative velocity does not correspond to the maximum excitation force on

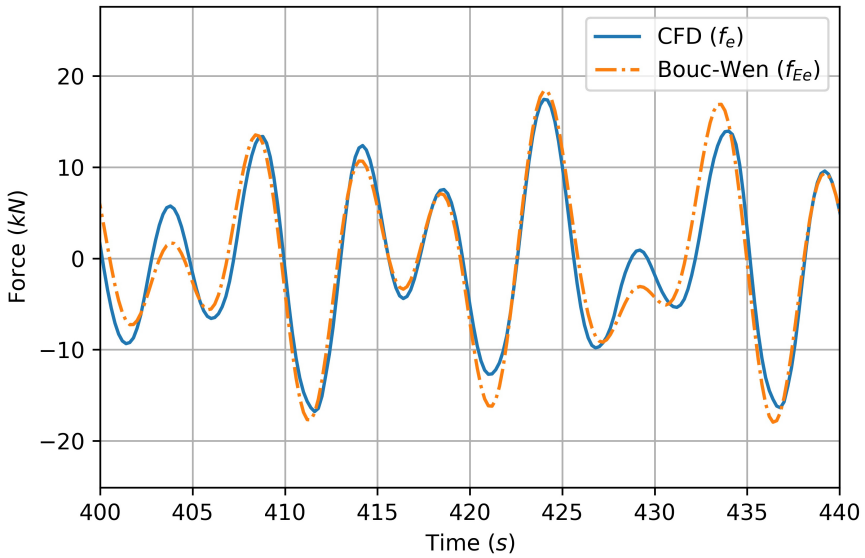

(a) Comparison between time series of excitation force f_e from CFD experiment and estimated excitation force from Bouc-Wen model f_{Ee} (only 40 s of the 600 s segment are plotted) (NRMSE = 0.25)

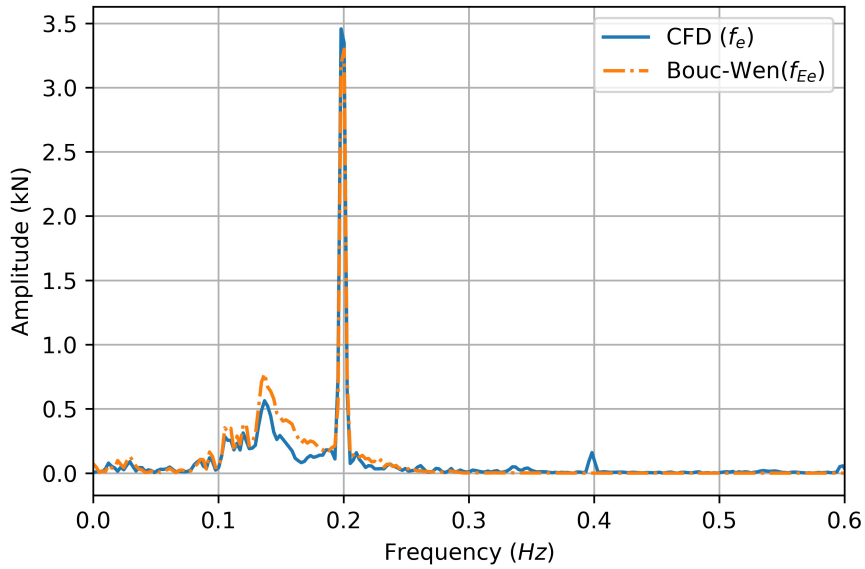

(b) Comparison between amplitude spectrum of excitation force obtained from CFD experiment and that estimated using Bouc-Wen model from (MAPE = $3.8 \times (10^{-2})$)

Figure 5.1: Comparison between CFD calculated and Bouc-Wen model calculated excitation force f_{Ee} on HP cylinder oscillating with $amp = 0.25\ m$ and $\omega = 1.25\ rad/s$ for realization $R1$. Coefficients are obtained from excitation force time series for sea state realization $R2$

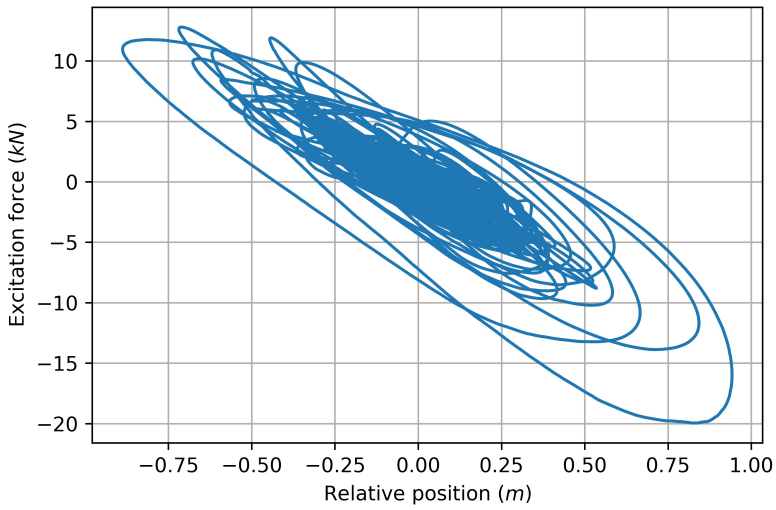

(a) $f_e - \zeta$

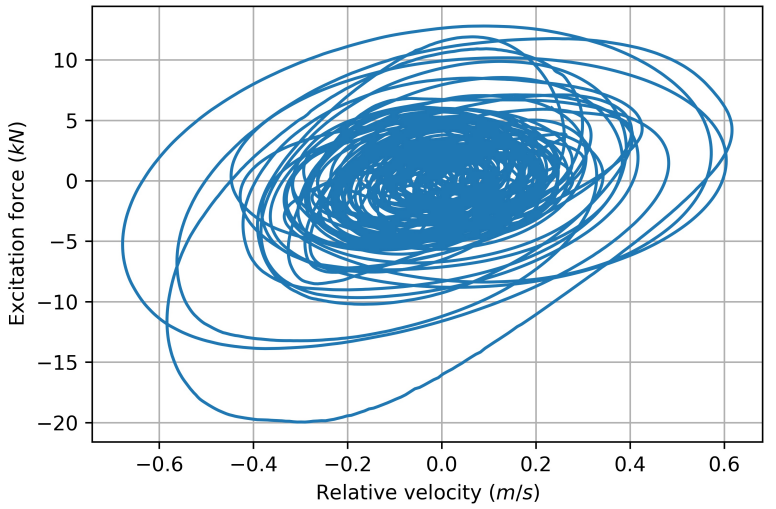

(b) $f_e - \dot{\zeta}$

Figure 5.2: Excitation force $f_e = f_d - f_{Es}$ on oscillating HP cylinder ($amp = 0.05\ m$) for realization $R1$ with relative position and velocity. The hydrodynamic force f_d is obtained from the hydrodynamic experiment in CFD and the estimated static force f_Es is calculated from the static block coefficient $\mathbf{C}$ and the time series of relative height ζ of the spar

Table 5.2: Values of parameters of Bouc-Wen equation, obtained from PSO for $R2$

amp (m)	a (kN/m)	b (kNs/m)	c (kNs^2/m)	α (kNs/m)	β (m^{-1})	γ (m^{-1})	n
0	1.1×10^{-4}	5.134	7.352	-8.99	-3641.57	-71959	2.54
0.05	1.6×10^{-3}	3.17	13.25	-5.25	-2392.2	-46566	2.2
0.15	1.18×10^{-2}	6.35	18.72	-3.47	-1515.24	-43014	2.3
0.25	1.86×10^{-2}	13.84	13.97	-11.62	-3542.61	-69835	2.0

the HP spar.

Based on the nature of input and output relationship as shown in Figure 2.8 for regular waves input and Figure 5.2 for irregular wave input, it is necessary that data driven models should accommodate hysteresis relationship. Another important conclusion that can be drawn from these images is the asymmetry in excitation force values during up and down strokes. It can be seen from Figure 5.2a that the force magnitude in upstroke (positive values of ζ and negative values of f_e) is higher for most of the oscillation cycle. A similar observation was made in (Brown et al., 2017); the authors found that the added mass and drag coefficients were different for up and down stroke of WEC oscillation for spar fitted with various heave plate designs, including flat plate.

5.4 Dynamic block identification

The dynamic block generalizes the overall model therefore the parameters of dynamic block have been identified from the experiment using sea state realization $R1$ whereas $R2$ is used only to identify the parameters of rate dependent block. Once the parameters of the rate dependent block are identified; ζ, $\dot{\zeta}$, $\ddot{\zeta}$ from $R1$ are used to calculate the estimated excitation force f_{Ee} and it is compared with the hydrodynamic force obtained from hydrodynamic experiment using $R1$. The comparison between these signals are plotted in Figure 5.1a. The state dependent model at this stage is referred as Hysteresis model (Hydrostatic+Bouc-wen) in Table 5.1. This stage is intermediate for the rate dependent models and the dynamic block has not been added to the model structure. In this section the procedure to identify the dynamic block coefficients is outlined for the HP and the square cylinder.

The composition of internal signal which is the input to dynamic block for various models is tabulated in Table 5.1. In the Hammerstain model the internal signal only consists of estimated values of hydrostatic forces f_{Es} whereas for rate dependent models the internal signal includes the estimated values of excitation force f_{Ee} through the addition of the Bouc-Wen model. Identification of the dynamic block utilizes the results of the experiments in which the spar was made to oscillate at amplitudes of $0.25\ m,\ 0.15\ m,\ 0.05\ m$ and frequency $\omega = 1.25\ rad/s$ for 700 s. Two different ranges of model order and time delay $n_a,\ n_b$ and n_d as described in Eq. (3.2), are analyzed to find an optimal combination these parameters in each range.

- Range 1 refers to the lower values of model orders in which substantial drop in the NRMSE is observed.
- Range 2 refers to the combination of model order values higher than Range 1, where second substantial drop in the NRMSE is observed.
- For both the ranges the step size was kept same at 0.2 s.
- $t_a = n_a \times 0.2$ represents the previous transient information of f_{Ed} that influence the current value of f_{Ed}, similarly $t_b = n_b \times 0.2$ represents the previous transient information of internal signal that influence the current value of f_{Ed} (refer Figure 3.5).

5.4.1 Choice of Range 1 model order and time delay

The identification of the dynamic block is done based on the procedures outlined in Section 3.5.3. It has been found by Giorgi et al. (2016a) that this procedure is very effective for simple geometries like square, triangular and circular cylinders. That procedure is based on the iteratively changing the values of $n_a,\ n_b$ and n_d with an objective of determining a smallest value of NRMSE between the estimated values of hydrodynamic force f_{Ed} and the CFD calculated hydrodynamic force f_d. For a linear model, the dynamic order of the model should be kept as small as possible to reduce dimensionality of the problem and hence complexity. Based on the above arguments, $2 \leq\ n_a \leq\ 9,\ 15 \leq\ n_b \leq\ 30$ and $-20 \leq\ n_d \leq\ 5$ were chosen as possible combinations for the ARX structure. This range of values will be referred as Range 1. This leads to identification of around 735 ARX structures for Range 1 for square cylinder and 4500 for HP cylinder for each case study. Range 1 is used for 1 case of

fixed square cylinder, 1 case of fixed HP cylinder and 1 cases each for HP cylinder oscillating at 0.05 m, 0.15 m and 0.25 m.

This process has been very effective for 2D square cylinder when the order of the ARX model is low ($2 \leq \ n_a \leq \ 9$ and $2 \leq \ n_b \leq \ 9$ has been used in Giorgi et al. (2016a) for a Hammerstein model). It has also been utilized in this thesis for the square and HP cylinder cases. For the following reasons the effect of higher ranges of model order are also considered for the oscillating HP cylinder cases.

1. In this thesis the HP cylinder is forced to oscillate at high frequency and amplitude, compared to the input spectrum of the sea.

2. The Bouc-Wen modelling approach to resolve hysteresis dependent phenomenon is used with Hammerstein model and KGP model. Since additional physics based model is used the accuracy of internal signal which is input to dynamic block is expected to increase.

3. In the proposed models the nonlinear rate dependent block is used with the dynamic block. Since the dynamic block utilizes a linear (used in Rate dependent Hammerstein) or a nonlinear model (used in Rate dependent KGP) to model the input f_{Ee} and output f_d of the dynamic block, a possibility exists that the significant dynamics remain unmodelled if lower order approximations to the internal signal are adopted.

Based on the above hypothesis, Range 2 will be considered for all the data-driven models and accuracy of the model in both the ranges will be analyzed before any conclusion is drawn on the requirement of higher order models.

5.4.2 Choice of Range 2 model order

Based on the discussion in Section. 3.4.3 and Figure 3.5, n_a represents the number of values of estimated hydrodynamic force f_{Ed} in the past and $n_b + 1$ represents the number of values of the internal signal that influence the current value of estimated hydrodynamic force f_{Ed}. Since in the training f_{Ed} is compared to f_d. The values of f_d and f_{Ee} can provide an indication on the range of values of n_a and n_b that should be investigated in order to find the optimal value. The amplitude spectrum of the hydrodynamic force generated by NWT experiment is plotted in Figure 5.3. It can be seen that the peak value of hydrodynamic force for oscillating HP cylinder occurs

around 0.2 Hz, which is the oscillation frequency of the HP cylinder. The same peak can be seen from the amplitude spectrum of the internal signal for the cases of with and without Bouc-Wen model in Figure 5.4a and Figure 5.4b respectively. From these plots we can see that for all the cases of HP oscillation, the high amplitude values of hydrodynamic force and internal signal are concentrated between 0.09 Hz and 0.25 Hz. From Figure 5.4b it can be concluded that t_a and hence n_a should correspond to the oscillation frequency between 0.09-0.15 Hz. The corresponding t_a and n_a values are 7-11 s and 35-55 respectively. Similarly, the initial values of n_b should correspond in the range of 0.05-0.04 Hz or 20-25 s.

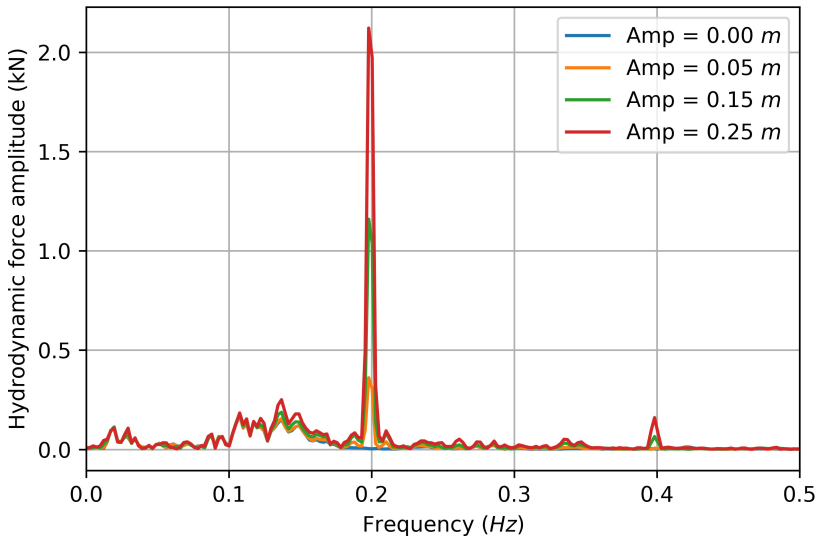

Figure 5.3: Amplitude spectrum of CFD calculated hydrodynamic force on HP cylinder oscillating at $\omega = 1.25\ rad/s$ for realization $R1$

5.4.3 Choice of Range 2 time delay

The time delay between the current estimated value of hydrodynamic force and the last value of internal signal that influences the calculation is represented by t_d. An observation here is that t_d represents the time shift between the output of the dynamic block and the input to the dynamic block-$i.e$ the internal signal. From Figure 5.3 and Figure 5.4, it can be said that the peak values of amplitudes of hydrodynamic force and internal signal are close, and hence the requirement of a large time delay is unlikely. Thus, a relatively small range of delays is considered: $-2\ s \leq\ t_d \leq\ 1\ s$. Based on the above arguments, for the case of HP cylinder another set of values as $35 \leq\ n_a \leq\ 55$, $100 \leq\ n_b \leq\ 125$ and $-10 \leq\ n_d \leq\ 5$ were chosen as possible

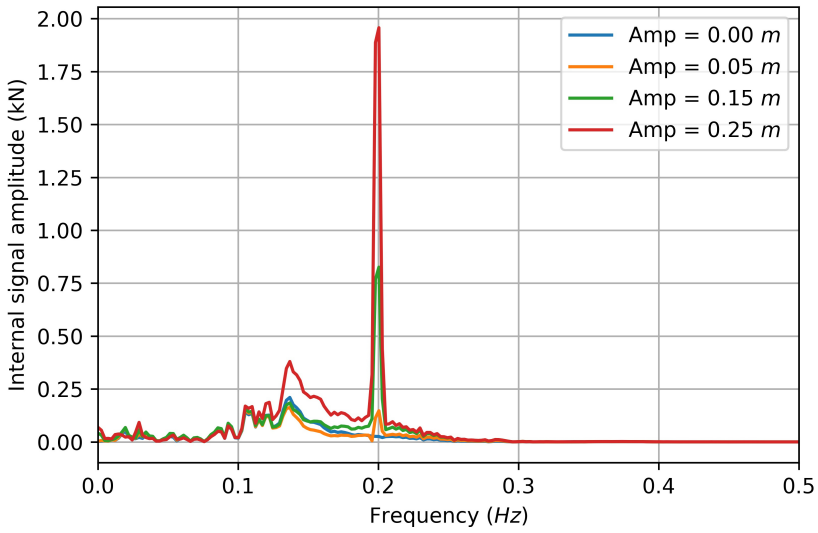

(a) Amplitude spectrum of estimated excitation force/internal force signal for rate dependent models ($s = f_{Es} + f_{Ee}$)

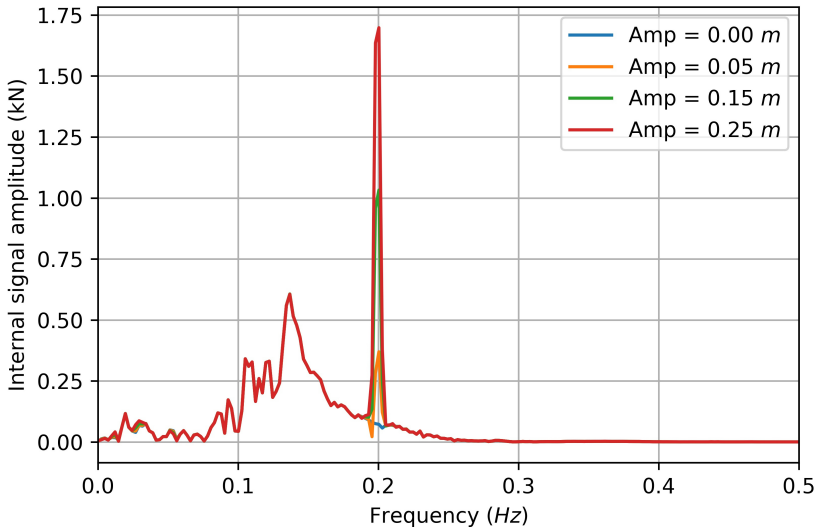

(b) Amplitude spectrum of estimated hydrostatic force/internal force signal for Hammerstein model ($s = f_{Es}$)

Figure 5.4: Comparison of amplitude spectrum internal signal for different amplitude of spar oscillation for realization $R1$ and oscillating HP cylinder ($\omega = 1.25\ rad/s$)

combinations for the ARX structure. This range of values will be referred as Range 2.

After establishing the ranges which define the search space for the optimization problem, the next step is to determine the optimum values of $n_a,\ n_b$ and n_d by identifying different ARX structures. Each ARX structure is a specific combination of dynamical order of the equation Eq. (3.2) and delay parameter ($n_a,\ n_b$ and n_d) values. The training procedure involves application of steps discussed in Section 3.5.4, with various combination of $n_a,\ n_b,\ n_d$. This leads to identification of around 2340 ARX structure for Range 2 for HP cylinder for each case study. Range 2 are used only for 2 cases of HP cylinder oscillating at 0.25 m and 0.15 m. A summary of the ranges analyzed for various models and test cases is presented in Table 5.3.

5.4.4 Results of dynamic block identification

The value of NRMSE between the estimated values of the hydrodynamic force f_{Ed} and CFD calculated hydrodynamic force f_d are recorded for each ARX structure. Since n_a provides the number of poles of the system, it is the most important parameter to be determined. The optimal values of n_a for fixed square cylinder are determined for Range 1 from Figure 5.5a. The optimal value of n_a, is the values of n_a at which the value of NRMSE is sufficiently low and increasing n_a after that doesn't reduce the value of NRMSE, significantly. Thus it can be said that the reduction in the values of NRMSE for $n_a \geq 4$, is insignificant. Therefore the optimal n_a for Range 1 is 4. The values of n_b and n_d are determined by plotting NRMSE at $n_a = 4$ for all the values of n_b and n_d. In the current case, $2 \leq\ n_b \leq\ 9$ and $-10 \leq\ n_d \leq\ 5$ were chosen. From Figure 5.5b, it can be concluded that the NRMSE doesn't show significant improvement for $n_b > 5$ and $n_d < -4$ or $n_d > -4$.

Similarly for oscillating HP cylinder at $amp = 0.25\ m$ and $\omega = 1.25\ rad/s$ and for sea state realization $R1$ and using Hammerstein model; $n_a,\ n_b$ and n_d values are determined for Range 1 and Range 2 from Figure 5.6. The optimal value of n_a for each range, is the value of n_a at which the value of NRMSE is lowest. Thus from Figure 5.6a and Figure 5.6c it can be said that the reduction in the values of NRMSE for $n_a \geq 5$, or $n_a \geq 55$ is insignificant. Therefore the optimal n_a for Range 1 and Range 2 is 5 and 55 respectively.

Once n_a is selected, the next step is the estimation of n_b and n_d. By plotting the loss function against t_d, for each value of n_b, Figure 5.6b and Figure 5.6d show

.

Table 5.3: Ranges analyzed for various data-driven model and test cases. The figures and tables to be referenced for the combination of model, range and test case analyzed is tabulated

Model	Range	Square	HP			
		Oscillation amplitude (m)				
		Fixed	Fixed	0.05	0.15	0.25
		Reference plot (Figure No.)				
Hammerstein	1	5.5	C.5a, C.5b	C.4a, C.4b	C.2a, C.2b	5.6a, 5.6b
	2	-	-	-	C.3a, C.3b	5.6c, 5.6d
Rate dep. Hammerstein	1	-	C.5c, C.5d	C.4c, C.4d	C.2c, C.2d	C.1a, C.1b
	2	-	-	-	C.3c, C.3d	5.7a, 5.7b
Rate dep. KGP	1	-	C.5e, C.5f	C.4e, C.4f	C.2e, C.2f	C.1c, C.1d
	2	-	-	-	C.3e, C.3f	5.7c, 5.7d
Reference Table No.		5.8	5.7	5.6	5.5	5.4

Note: Click on the Figure No. and Table No. to refer.

that the minimum of the NRMSE occurs at different n_d, depending on the value of n_b. Figure 5.6b shows the NRMSE curves for the case of $n_a = 5$ and $15 \leq n_b \leq 29$, the minima of the curves stop decreasing at n_d equal to -9 and Figure 5.6d shows that at $n_a = 55$ and $110 \leq n_d \leq 124$ the minima of the curves stop decreasing for about n_d equal to -4. The objective is to obtain small values of NRMSE, and it is possible to see that their is no significant difference for $n_b \geq 27$ in Figure 5.6b and NRMSE is lowest for $n_b = 124$ in Figure 5.6d. This shows that $n_b = 27$ and $n_b = 124$ are the optimal value to obtain a parsimonious model structure. The optimal values of n_a, n_b and n_d corresponding to both the ranges are tabulated in Table 5.4. It can be seen from Figure 5.6 and Table 5.4 that a significant reduction in the values of NRMSE has been obtained for Range 2. The variation of NRMSE for rate dependent models in Range 2 are shown in Figure 5.7. The variation of NRMSE for rate dependent models in Range 1 for same test case are shown in Figure C.1. A summary of all the figures and tables corresponding to identification of dynamic block are provided in Table 5.3. A significant reduction in the values of NRMSE has also been obtained for Range 2

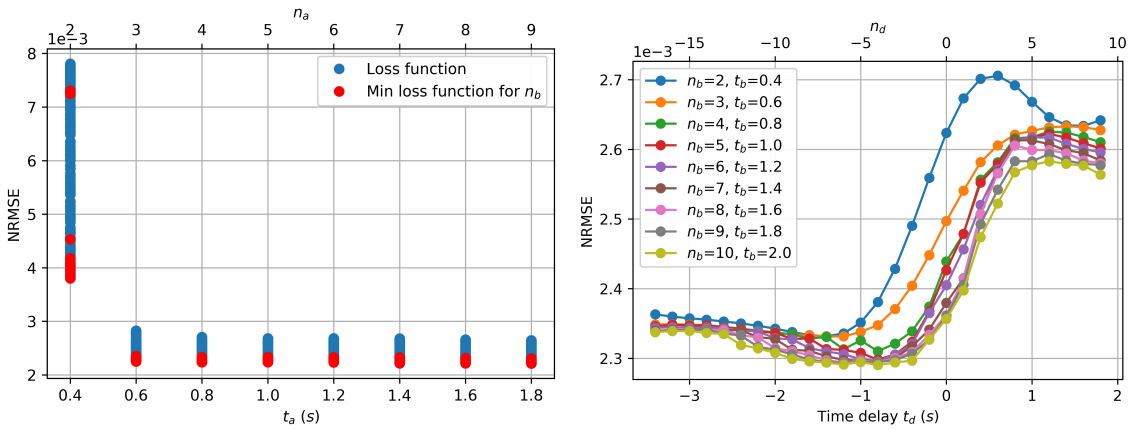

(a) NRMSE Vs n_a for Range 1

(b) NRMSE Vs n_d for Range 1

Figure 5.5: NRMSE for fixed square cylinder for realization $R1$, each vertical line in Figure 5.5a shows the range of loss function for a specific values of n_a and predetermined values of n_b and n_d, each line in Figure 5.5b shows the loss function for a specific values of n_b and all the values of n_d

for the test case of oscillating HP cylinder at $amp = 0.15\ m$ and $\omega = 1.25\ rad/s$. The variation of NRMSE against n_a and n_d for all the models used in this test case in Range 1 and Range 2 is shown in Figure C.2 and Figure C.3, respectively and the values are tabulated in Table 5.5. In order to confirm the observations, the FFT of the estimated values of hydrodynamic force are compared with the CFD generated

values. The MAPE for two ranges is also tabulated in Table 5.4 and Table 5.5 for oscillating HP cylinder at $amp = 0.25\ m$ and $amp = 0.15\ m$ respectively and it can be seen that MAPE for Range 2 is also lower when compared to Range 1.

In this work the need for a high dynamic order for HP oscillating at 0.25 m and 0.15 m is clearly evident based on the steep reduction in the NRMSE for Range 2. For cases of HP cylinder oscillating at 0.05 m and fixed HP cylinder, it was found that the drop in the NRMSE was gradual and insignificant in the window of Range 2, or any other window between Range 1 and Range 2. Therefore for these cases only results corresponding to Range 1 have been shown in Table 5.6 and Table 5.7 respectively. The plots for variation of NRMSE for HP cylinder oscillating at 0.05 m and 0.00 m for Range 1 is shown in Figure C.4 and Figure C.5 respectively.

Table 5.4: Optimal values of n_a, n_b and n_d for HP cylinder oscillating at $amp = 0.25\ m$ and $\omega = 1.25\ rad/s$ for realization $R1$

Model	Range	n_a	n_b	n_d	delay (s)	NRMSE (f_{Ed}, f_d)	MAPE FFT-(f_{Ed}, f_d)
Hammerstein	1	5	23	-4	-0.8	$1.62 \times (10^{-2})$	$7.66 \times (10^{-3})$
	2	55	122	-11	-2.2	$1.39 \times (10^{-2})$	$6.17 \times (10^{-3})$
Rate dep. Hammerstein	1	5	27	-9	-1.8	$1.6 \times (10^{-2})$	$7.52 \times (10^{-3})$
	2	59	124	-4	-0.8	$1.38 \times (10^{-2})$	$6.0 \times (10^{-3})$
Rate dep. KGP	1	5	29	-10	-2	$1.53 \times (10^{-2})$	$7.35 \times (10^{-3})$
	2	59	129	-10	-2	$1.2 \times (10^{-2})$	$5.6 \times (10^{-3})$

Since the input signal to the dynamic block in the case of rate dependent models has more state dependent system information compared to the Hammerstein model, it is expected that the accuracy of the rate dependent models will be higher than the Hammerstein model. It can be seen from Table 5.4, Table 5.5, Table 5.6 and Table 5.7 that the NRMSE decreases for both the rate dependent models in both the ranges. The accuracy of prediction improves by a minimum and maximum of 75 % and 88 % for maximum HP oscillation and 61 % and 67 % for fixed HP cylinder. Similarly the results predicted by rate dependent KGP model also show significant improvement in prediction of hydrodynamic forces. In rate dependent KGP model a nonlinear dynamic block is used along with the Bouc-Wen model. Thus it is the most expensive model in terms of computational cost, and the most accurate. It can

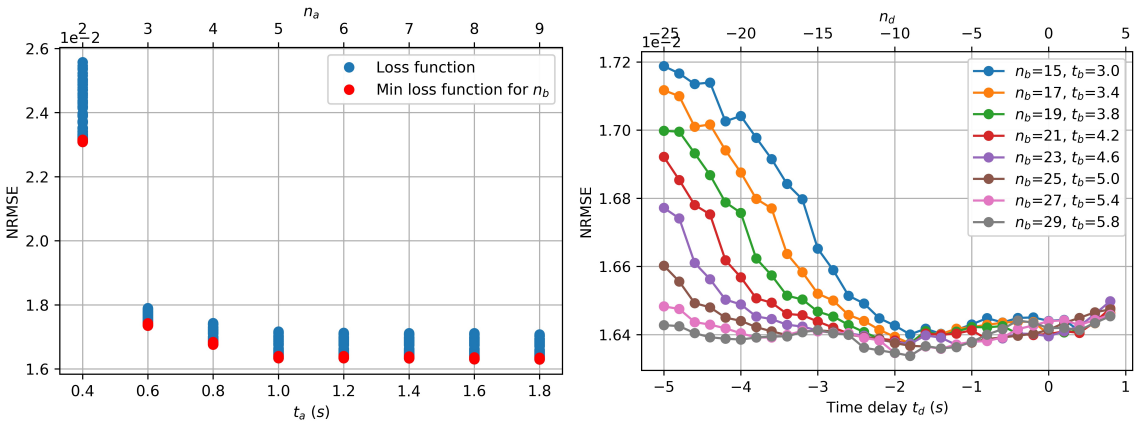

(a) NRMSE Vs n_a for Range 1

(b) NRMSE Vs n_d for Range 1

(c) NRMSE Vs n_a for Range 2

(d) NRMSE Vs n_d for Range 2

Figure 5.6: NRMSE for HP cylinder oscillating at $amp = 0.25\ m$ and $\omega = 1.25\ rad/s$ for realization $R1$ using Hammerstein model in the Range 1 and Range 2 is plotted against n_a or t_a values, each vertical line shows the range of loss function for a specific values of n_a and predetermined values of n_b and n_d

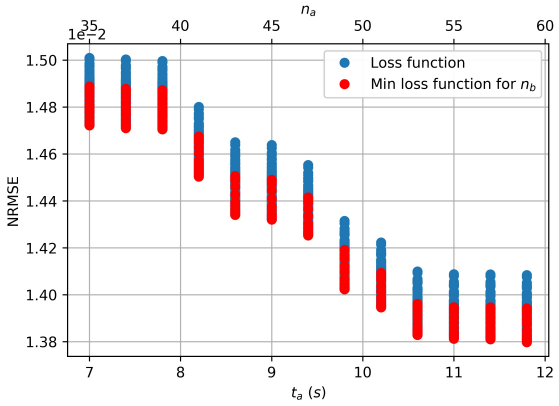

(a) NRMSE Vs n_a (Rate dependent Hammerstein model)

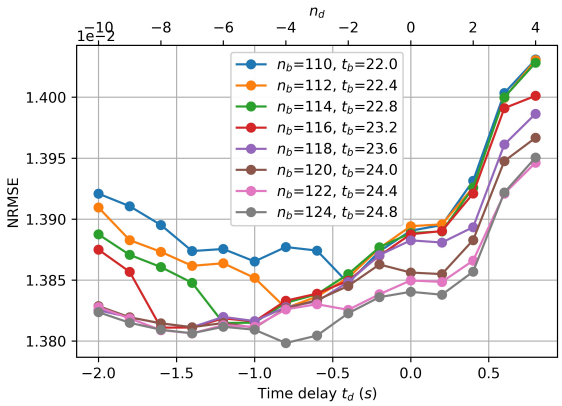

(b) NRMSE Vs n_d (Rate dependent Hammerstein model)

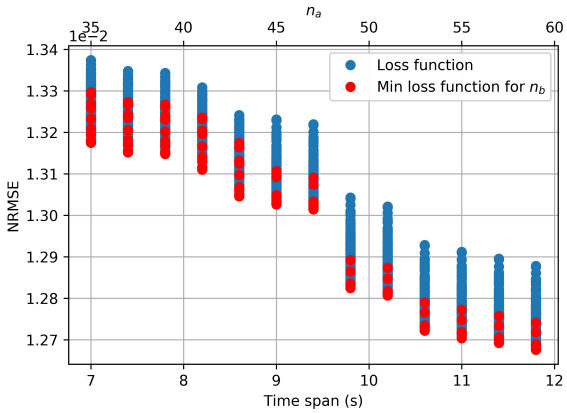

(c) NRMSE Vs n_a (Rate dependent KGP model)

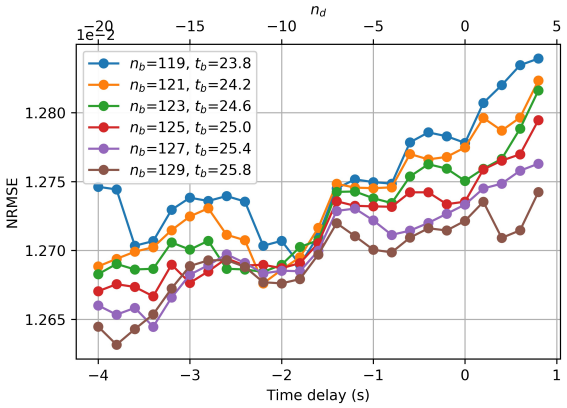

(d) NRMSE Vs n_d (Rate dependent KGP model)

Figure 5.7: NRMSE for HP cylinder oscillating at $amp = 0.25\ m$ and $\omega = 1.25\ rad/s$ for realization $R1$ and Range 2, illustrating a comparison between all the system identification models used in this thesis

Table 5.5: Optimal values of $n_a,\ n_b$ and n_d for HP cylinder oscillating at $amp = 0.15\ m$ and $\omega = 1.25\ rad/s$ for realization $R1$

Model	Range	n_a	n_b	n_d	delay (s)	NRMSE (f_{Ed}, f_d)	MAPE FFT-(f_{Ed}, f_d)
Hammerstein	1	5	23	-1	-0.2	$1.69 \times (10^{-2})$	$7.3 \times (10^{-3})$
	2	59	129	-6	1.2	$1.5 \times (10^{-2})$	$5.89 \times (10^{-3})$
Rate dep. Hammerstein	1	5	27	-4	-0.8	$1.65 \times (10^{-2})$	$7.0 \times (10^{-3})$
	2	59	116	-7	-1.4	$1.49 \times (10^{-2})$	$5.9 \times (10^{-3})$
Rate dep. KGP	1	6	29	0	0	$1.6 \times (10^{-2})$	$6.7 \times (10^{-3})$
	2	59	129	-7	-1.4	$1.36 \times (10^{-2})$	$5.0 \times (10^{-3})$

Table 5.6: Optimal values of $n_a,\ n_b$ and n_d HP cylinder oscillating at $amp = 0.05\ m$ and $\omega = 1.25\ rad/s$ for realization $R1$

Model	n_a	n_b	n_d	delay (s)	NRMSE (f_{Ed}, f_d)	MAPE FFT-(f_{Ed}, f_d)
Hammerstein	5	25	-6	-1.2	$1.65 \times (10^{-2})$	$7.0 \times (10^{-3})$
Rate dep. Hammerstein	5	27	-4	-0.8	$1.65 \times (10^{-2})$	$7.0 \times (10^{-3})$
Rate dep. KGP	5	27	-4	-0.8	$1.53 \times (10^{-2})$	$5.3 \times (10^{-3})$

also be concluded that the prediction accuracy with optimal parameters in Range 2 is higher compared to Range 1, this is expected as the model becomes more flexible. The effect of increasing the dynamical order of the model is be validated for validation case simulation in Section 5.5.

Table 5.7: Optimal values of $n_a,\ n_b$ and n_d fixed HP cylinder for realization $R1$

Model	n_a	n_b	n_d	delay (s)	NRMSE (f_{Ed}, f_d)	MAPE FFT-(f_{Ed}, f_d)
Hammerstein	6	29	-5	-1	$1.58 \times (10^{-2})$	$6.1 \times (10^{-3})$
Rate dependent Hammerstein	6	27	-7	-1.4	$1.53 \times (10^{-2})$	$5.8 \times (10^{-3})$
Rate dependent KGP	7	27	-9	-1.8	$1.43 \times (10^{-2})$	$4.9 \times (10^{-3})$

5.5 Validation

In the current study a different realization of sea state $R3$ is considered for validation. The dynamical order $(n_a,\ n_b)$ and the delay constant n_d were established using realization $R1$. These values were given in Table 5.8 for the square cylinder and Table 5.4, Table 5.5, Table 5.6 for values corresponding to cases studies of HP cylinder oscillating at $\omega = 1.25\ rad/s$ and $amp = 0.25\ m, 0.15\ m,\ 0.05\ m$ respectively and from Table 5.7 for the fixed HP cylinder.

Before comparing the model performance on the different cases of HP cylinder, a comparison between the hydrodynamic force on a fixed square cylinder and a fixed HP cylinder is to be done using the Hammerstein model. Under that conventional Hammerstein approach optimal values of $n_a = 3,\ n_b = 6$ and $n_d = -4$ and $n_a = 6,\ n_b = 29$ and $n_d = -5$ were determined for fixed square cylinder and fixed HP cylinder respectively. These values along with the values of NRMSE are tabulated in Table 5.8.

For the fixed square cylinder, the results of the simulation using the Hammerstein model are plotted in Figure 5.9a. This plot shows the time series of hydrodynamic force obtained from CFD and that estimated from the Hammerstein model. The plot of the amplitude spectrum of the hydrodynamic forces on the fixed square cylinder in shown in Figure 5.8. The values of NRMSE and MAPE are 0.15 and 0.014

Table 5.8: Optimal values of n_a, n_b and n_d fixed square cylinder and HP cylinder oscillating at $amp = 0.25\ m$ and $\omega = 1.25\ rad/s$ for realization $R1$

Spar	Range	n_a	n_b	n_d	delay (s)	NRMSE (f_{Ed}, f_d)	MAPE FFT-(f_{Ed}, f_d)
Square	1	3	6	-4	-0.8	$2.29 \times (10^{-3})$	$1.0 \times (10^{-3})$
HP	1	6	29	-5	-1	$1.58 \times (10^{-2})$	$6.1 \times (10^{-3})$

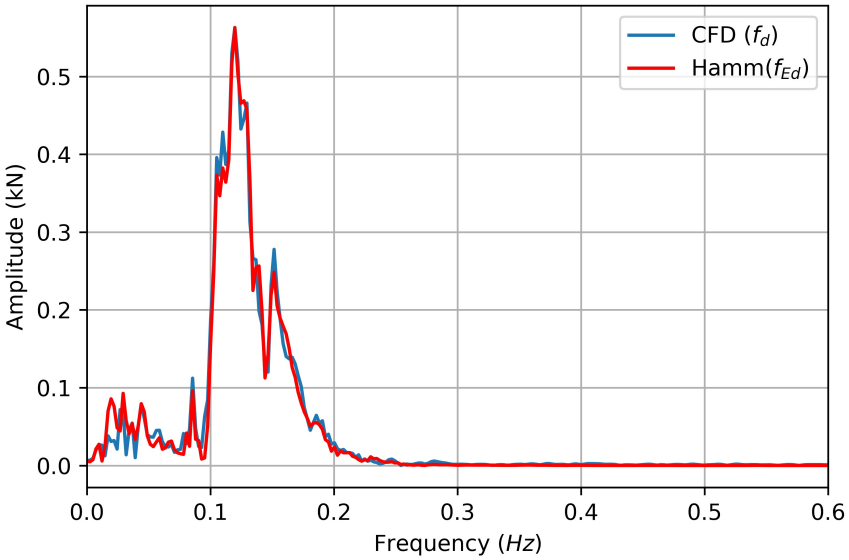

Figure 5.8: Comparison of amplitude spectrum of hydrodynamic force on square cylinder from CFD experiment and that estimated from Hammerstein model for training data-Range 1 (MAPE= 1.4×-2)

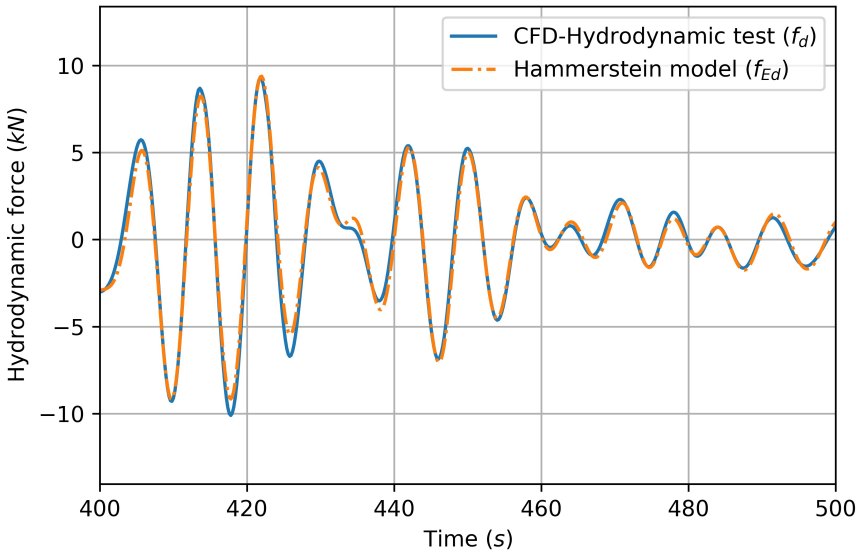

(a) Square cylinder

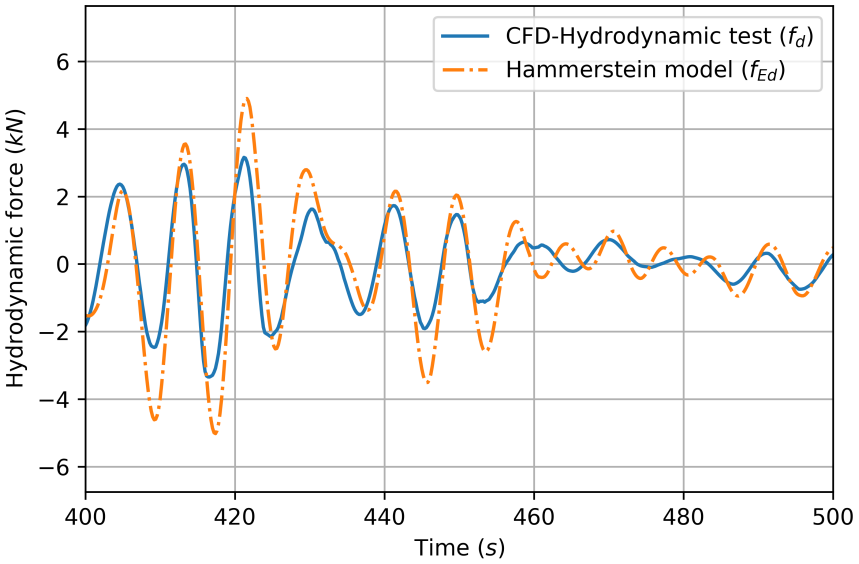

(b) HP Cylinder

Figure 5.9: Prediction of forces on fixed spar for $R3$ realization of sea state, based on the parameters identified form $R1$ realization of sea state. The system identification model utilizes data from 110 s to 700 s but only a portion of it is plotted for clarity.

respectively. The value of NRMSE reported in Giorgi et al. (2015) is 0.13. It can be seen that the model prediction based on training data accurately predicts the hydrodynamic force. The process is repeated for fixed HP cylinder in Range 1 and the predicted hydrodynamic forces along with the CFD generated values is shown in Figure 5.9b. The corresponding NRMSE for HP cylinder is 0.54.

Thus, based on the values of NRMSE and the plot of hydrodynamic force it can be concluded that the Hammerstein model in its conventional form cannot accurately predicts forces for the HP cylinder geometry, and the model has to be modified to account for the hysteresis between force and higher order parameters like velocity and acceleration.

Two additional models with stand-alone application of the static block and a combination of the state dependent Bouc-Wen model and static block were used. These models will be hereby referred as Hydrostatic model and Hysteresis model respectively. The characteristics of all the five models, composition of internal signals, the input parameter for each block and the output of each block is tabulated in Table 5.1. Though rate dependent block is used in the Hysteresis model, training will not be required as the final output of the model is estimated the hydrodynamic force f_{Ed}, rather than internal signal s.

Four cases of HP cylinder oscillation at a frequency of 1.25 rad/s and amplitudes of 0.25 m, 0.15 m,0.05 m and 0.0 m are used for the validation purpose. The values of the error metric for these cases have been tabulated in Table 5.9. The time series and the FFT plots of the HP cylinder oscillating at amplitude of 0.25 m and 0.15 m are plotted in Figure 5.10 and Figure 5.11 for Range 1 and Range 2 respectively. For 0.05 m and 0.0 m the plots corresponding to Range 1 are plotted in Figure 5.12. The model with the lowest error is mentioned in brackets in the corresponding caption. The hydrostatic model has not been plotted in these plot because the error metric are high and their tabulated values provide enough insight in their insignificance as an independent model.

In the hydrostatic model, it is expected that the accuracy will improve as the input signal to the static block approaches to the free surface height. From Table 5.9, this conclusion is affirmed as the value of NRMSE decreases as body oscillation approaches to fixed cylinder. At the same time increase in MAPE values indicated that, though the model's accuracy to predict the amplitude improves; there is a significant phase difference at lower amplitude of oscillation. The over all performance of Bouc-Wen model is significantly better compared to hydrostatic model. From the FFT plots

it can be concluded that the Bouc-Wen model's accuracy in predicting the force corresponding to amplitude of oscillation decreases with the decrease in oscillation as well as it over predicts low frequency components in the presence of high amplitude oscillation in the input signal (see Figure 5.10b and Figure 5.11b). This also indicates the lag is caused by vortex shedding due to body oscillating at high frequency and amplitude as due to vortices non-linearity between position of spar and hydrodynamic force develops. Similar conclusions can be drawn when the fixed WEC is subjected to low frequency waves (see Figure 5.12d).

Table 5.9: Error metric for all the cases of HP cylinder oscillation

	Model			NRMSE (f_{Ed}, f_d) Amplitude (m)				MAPE ($\times 10^{-2}$) (FFT-f_{Ed}, f_d) Amplitude (m)			
				0.25	0.15	0.05	0.0	0.25	0.15	0.05	0.0
State dep.	Hydrostatic			1.53	1.17	0.812	0.77	8.1	10.2	13.1	27.0
	Hydrostatic + Bouc-Wen			0.431	0.589	0.635	0.44	4.8	3.8	3.7	6.6
Training needed	Hammerstein	Range	1	0.243	0.353	0.432	0.54	3.71	3.95	3.94	6.69
			2	0.224	0.284	-	-	3.29	3.36	-	-
	Rate dep-Hammerstein		1	0.236	0.337	0.44	0.35	3.59	3.48	3.7	4.0
			2	0.217	0.261	-	-	3.25	3.26	-	-
	Rate dep-KGP		1	0.234	0.315	0.449	0.33	3.61	3.49	3.67	3.42
			2	0.228	0.26	-	-	3.37	3.23	-	-

The overall accuracy of Hammerstein model is lower when compared to the rate dependent models and it decreases with decrease in the oscillation amplitude. The presence of Bouc-Wen model along with the hydrostatic model shows that the improvement in the prediction when compared to only the hydrostatic model. When rate dependent block is augmented with linear dynamic block, further improvement in the accuracy by $20-50\%$ is observed for all the test cases except for fixed cylinder. The rate dependent models for these cases show almost 25% when compared to model without dynamic block and 38% when compared to Hammerstein model.

In all the cases corresponding to Range 1, Hammerstein model over-predicts the force especially in the low frequency range. This is the result of lower dynamical order values compared to those in Range 2. The high oscillation of force in low frequency

proves the point that by using Hammerstein model without hysteresis nonlinearity significant amount of dynamics goes unmodelled. The dynamic order of the model was increased in Range 2 for HP oscillating at 0.25 m and 0.15 m but not for other cases as no significant drop in error values was found. The low frequency oscillation were not found for higher orders for any of the models, and the rate dependent models were again found to be more accurate in this range.

Comparing the performance of rate dependent Hammerstein and rate dependent KGP models, it was found that KGP model was as accurate as the rate dependent Hammerstein model for the validation case, though the values of NRMSE were found to be significantly lower in the training case compared to any other data-driven model. The trend in the MAPE values was also same as NRMSE and hence it gives a confidence on the values of n_a, n_b and n_d selected for validation. It was found that the values of MAPE increases in Range 2 compared to values in Range 1 for test cases corresponding to 0.25 m oscillation amplitude. This is due to overfitting and as frequency component were introduced at 0.2 Hz. The improvement for HP cylinder oscillating at 0.15 m is noticeable but for other cases, particularly in Range 2, the rate dependent KGP model proves to be computationally expensive without improvement in accuracy. The difference between these two models, is the use of nonlinear input-output relationship in the dynamic block (ARX model) of rate dependent KGP model. This implies that higher order values of internal signal and hence the higher number of $n_b + 1$ coefficients were used in rate dependent KGP model.

The fitting error of an identified model is larger in validation than in training due to accumulation of numerical error in simulation procedure. It can be concluded from the values of NMRSE and MAPE that the performance of the models are best for high oscillation amplitude of HP cylinder in an irregular wave field. Though the overall trend of decrease in model accuracy towards lower oscillations amplitudes can be seen in all the candidate data-driven models, a reversal in this trend was observed for the rate dependent and Bouc-Wen models when the amplitude of oscillation was between 0.15 m and 0.05 m. It should be noted that at oscillation amplitude of 0.05 m the order of magnitude of hydrodynamic force at frequency of oscillation is comparable to the hydrodynamic force on a fixed spar. The linear model has difficulty in following peaks in the hydrodynamic force. The data utilised in the case studies show the presence of hydrodynamic nonlinearities, which the rate dependent or nonlinear model are able to describe. Though the HP cylinder has a linear restoring curve, it has a very flat bottom with sharp corners and a positive aspect ratio of the plate with the spar. The

heave plate is the source of important nonlinear effects due on viscosity and vortex shedding.

Other authors (Nelles, 2001; Giorgi et al., 2016b) have cautioned on the use of KGP models, due to its computational requirements and sensitivity with respect to noise. Though in this thesis KGP model has been used with Bouc-Wen model, the results reiterates on the points made by other authors and concludes that KGP models though accurate are expensive.

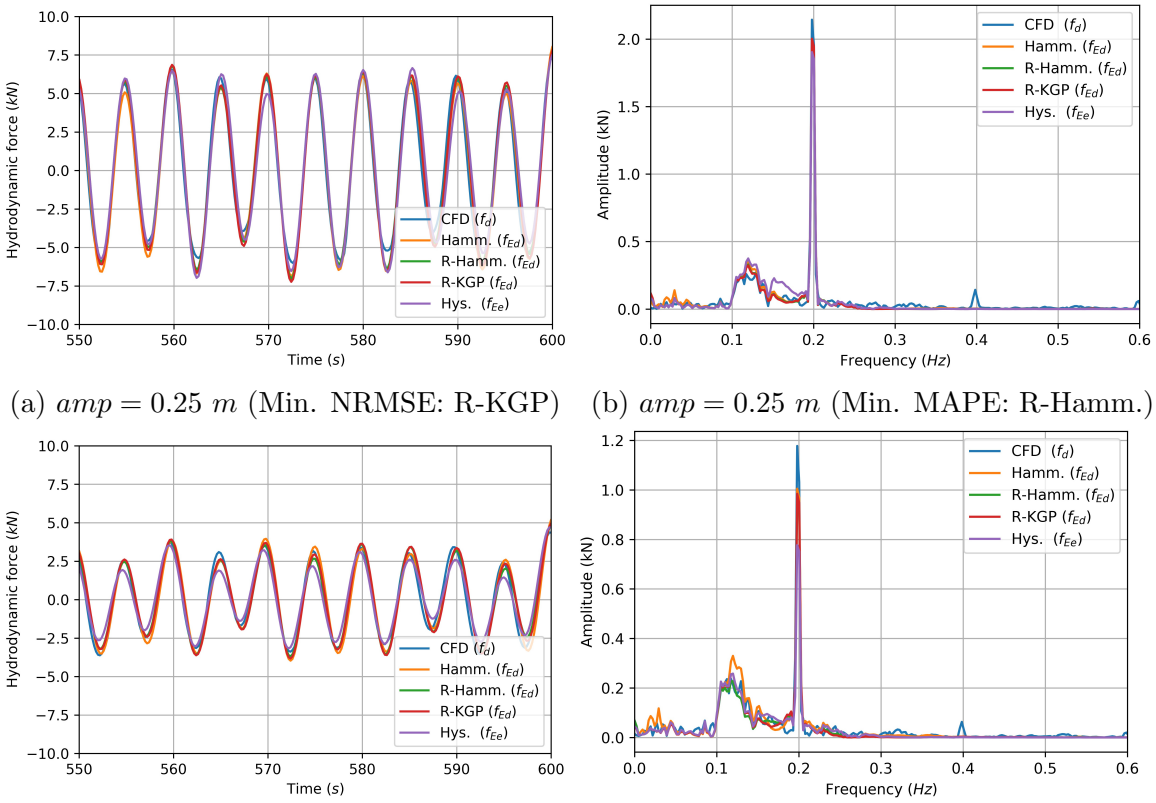

(a) $amp = 0.25\ m$ (Min. NRMSE: R-KGP) (b) $amp = 0.25\ m$ (Min. MAPE: R-Hamm.)

(c) $amp = 0.15\ m$ (Min. NRMSE: R-KGP) (d) $amp = 0.15\ m$ (Min. MAPE: R-Hamm.)

Figure 5.10: Hydrodynamic force on HP cylinder oscillating at $\omega = 1.25\ rad/s$ and amplitudes of 0.25and0.15 for realization $R3$ (Training data-Range 1)

The approximate time required in each step of data generation and SI process is consolidated in the Table 5.10. Though the high performance computing facility at Compute Canada was used in the CFD and training simulation, these clock times represent the wall clock time on a 4 core, x86_64 architecture Intel Xeon desktop computer. The parameters that are generated by each of these processes are also tabulated. It can be seen that the data generation process takes most of the time, particularly in the hydrodynamic test case, in which three simulations are required for

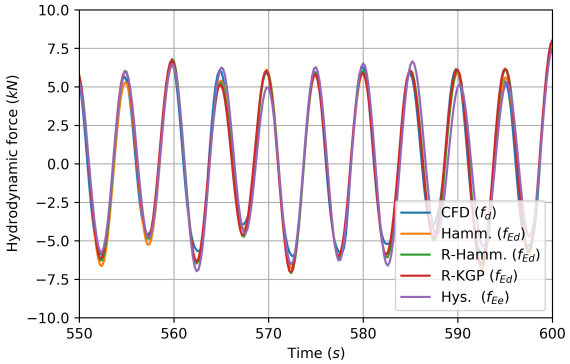

(a) $amp = 0.25\ m$ (Min. NRMSE: R-Hamm.)

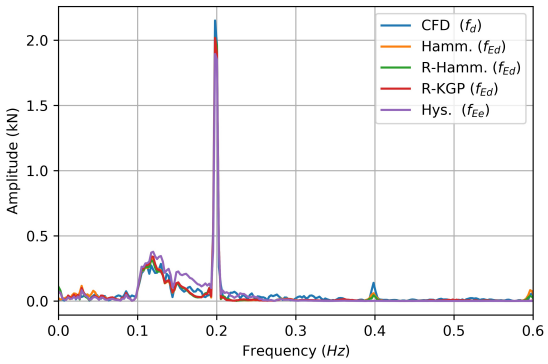

(b) $amp = 0.25\ m$ (Min. MAPE: R-Hamm.)

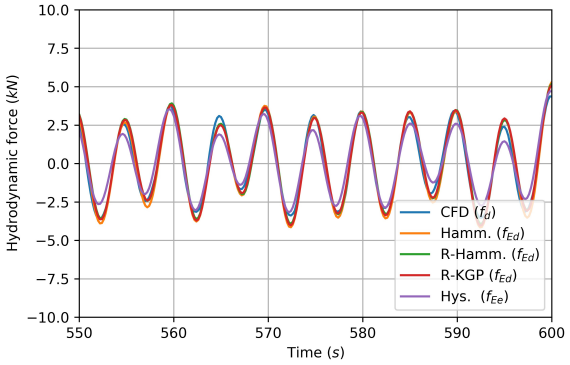

(c) $amp = 0.15\ m$ (Min. NRMSE: R-KGP)

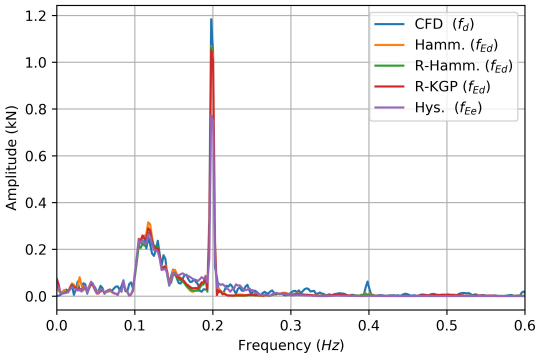

(d) $amp = 0.15\ m$ (Min. MAPE: R-KGP)

Figure 5.11: Hydrodynamic force on HP cylinder oscillating at $\omega = 1.25\ rad/s$ and various amplitudes for realization $R3$ (Training data-Range 2)

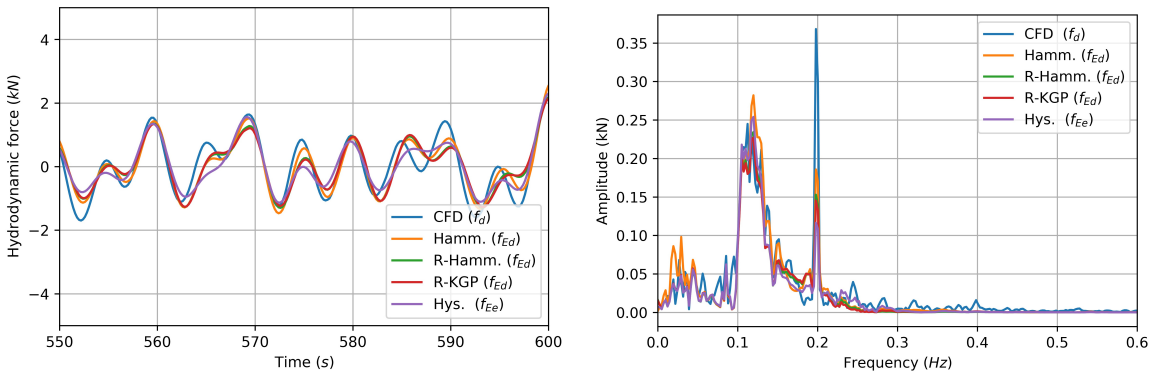

(a) $amp = 0.05\ m$ (Min. NRMSE: Hamm.)

(b) $amp = 0.05\ m$ (Min. MAPE: R-KGP)

(c) $amp = 0.0\ m$ (Min. NRMSE: R-KGP)

(d) $amp = 0.0\ m$ (Min. MAPE: R-KGP)

Figure 5.12: Hydrodynamic force on HP cylinder oscillating at $\omega = 1.25\ rad/s$ and amplitudes of 0.05 and fixed cylinder for realization $R3$ (Training data-Range 1)

each realization. The difference in the values of two cases of hydrodynamic simulation is because in the case of spar oscillation moving mesh algorithm is utilized.

The simulation time when moving mesh is involved is higher compared to fixed mesh cases. In addition to the CFD simulation time another huge portion of time which has not been tabulated is the geometry and mesh generation time, which is dependent on the skill of the analyst. The coefficients of Bouc-Wen equation Eq. (3.9) uses PSO algorithm and is computationally faster relative to compared to data generation or training depending on the values of initial guess of particle position, number of particles and number of iterations. A guideline on the selection of these values are provided in Section 3.5.3. Since two ranges have been analyzed in this thesis, the values corresponding to both of the ranges is tabulated and it can be seen that the time required for training and simulation for Range 2 is higher than Range 1 for all the models. This is due to the higher values of $n_a,\ n_b$ for Range 2. The clock times tabulated for training process are for 1 ARX structure, each ARX structure is a combination of $n_a,\ n_b$ and n_d values. The number of ARX structure used in particular cases are discussed in Section 5.4. It can be seen from the table that the time required by rate dependent KGP model is higher in all the cases when compared to rate dependent Hammerstein model. This is due to the use of second order polynomial in KGP model.

Table 5.10: Approximate clock time required in each step

Model	CFD tests (hrs)			PSO (hrs)			Training ($s/ARXstr$)[&]	Simulation (s)
	Hydro-static	Hydro-dynamic						
Identification Parameters	$\mathbf{C}$	f_d^+	ζ^*	$a,\ b,\ c$ $\alpha,\ \beta,\ \gamma$			$n_a,\ n_b$ n_d	f_{Es}
Hammerstein	8	16×3	12×3	2	Range	1	40	59
						2	72	66
Rate dep. Hammerstein						1	74	78
						2	80	80
Rate dep. KGP						1	76	79
						2	90	90

[+] 3 hydrodynamic CFD simulations to determine f_d for 3 sea state realizations ($R1,\ R2$ and $R3$)
[*] 3 hydrodynamic CFD simulations to determine ζ for 3 sea state realizations ($R1,\ R2$ and $R3$)
[&] Time taken by model to train 1 ARX structure

Chapter 6

Summary and conclusions

6.1 Summary

A data-driven modelling framework for numerical prediction of the hydrodynamic forces on geometries of significance to wave energy conversion is presented. Three time domain data-driven model structure have been proposed to model the hydrodynamic force on spar fitted with heave plate. Using CFD simulators to generate training data, the data driven model structure is subdivided into simpler blocks of physical importance. These blocks are a static block, a nonlinear hysteresis block and a linear or nonlinear dynamic block. The nonlinear hysteresis block is realized by a Bouc-Wen model to capture the rate-dependent effects of hysteresis. The nonlinear static block and the dynamic block are evaluated utilizing least squares estimation and ARX model. The Bouc-Wen model parameters are identified by PSO to identify the hysteresis properties. In order to evaluate the model performance, a fixed square cylinder and four cases with HP cylinder as spar were simulated, one with stationary spar and three cases of oscillating spar in an irregular wave field. Five meta-models were analyzed, two were state dependent models that do not require training while the other three required training to identify dynamic order or model equations.

In order to develop confidence in the data generation procedure, a high fidelity CFD modelling for numerical prediction of the hydrodynamic forces on scaled model of self-reacting point absorber Wave Energy Converter is presented and compared with experimental results. Two different test methodology were adapted, these are known as diffraction tests and radiation tests. In the diffraction test the WEC is subjected to incoming wave and the hydrodynamic force on the body is recorded

whereas in the radiation test the WEC spar is oscillated in a quiescent field. The component geometries are enclosed in two different fluid domains, each subjected to relative motion using a arbitrary mesh interface algorithm. The transfer of field variables across the domains is achieved through an arbitrary mesh interface. This unique methodology avoids cell deformation close to the component parts of the WEC, thus eliminating the errors in force calculation due to deformed cells. The continuity and momentum equations along with the free surface are solved separately in each domain. The validation of radiation force calculated from CFD is done by the experimental results for different heave oscillations test conditions.

6.2 Conclusions

Chapter 2 show the requirement of nonlinear hydrodynamic modelling of WECs, because of the presence of viscous drag and hysteric structure of state-dependent variables with the hydrodynamic force. If the projected area of either the float or spar changes at the free surface a nonlinear restoring force will also be introduced depending on the wave and oscillation amplitudes. Indeed, large body amplitudes increase the nonlinear dissipative effects. The ideal WEC modelling solution is a nonlinear parametric model, characterized by a good compromise between accuracy and computation time. This model should be able to describe the whole operating frequency region. In Chapter 2 several time domain CFD simulation were performed at discrete frequencies, the results hint at the presence of hydrodynamic nonlinearities, particularly at high amplitude oscillations. Multiple WEC configurations utilize the concept of harnessing energy by relative motion between different components. A methodology to simulate the heave motion between two closely placed annulus geometries has been presented. For SRPAs these geometries are float and spar. It has been pointed out in literature that, the moonpool can enhance the wave energy conversion in some frequency ranges or hinder the motion of the cylinder buoy in some other. For the case of WEC B, it was seen that the diffraction force magnitude obtained from CFD (which considered moonpool between float and spar) is higher compared to that from physical tank test and BEM results. One of the major improvements proposed by this thesis is the use of CFD-NWT instead of traditional BEM, for hydrodynamic model identification, since NWT data contain the full range of nonlinear hydrodynamic effects described by the Reynolds Averaged Navier-Stokes (RANS) equations. The wave generation (at inlet) and absorption (at outlet) is sen-

sitive to characteristics of the waves. Thus if NWTs are used, sensitivity studies are required prior to data generation for characterization of absorption coefficients with respect to incoming waves. For radiation tests a radial NWT with appropriate boundary condition and oscillating body at the centre of tank is required.

WECs with heave plates generate reaction forces that exhibit nonlinear relationships with single or multiple input parameters including free surface elevation, relative velocity and acceleration. Some of these input parameters show causal relationships with the output reaction force, while others show hysteric relationships with components of the output reaction forces. Earlier attempts to addressed the nonlinear and non-causal relationship between free surface and reaction force have been limited to simple hulls with heaving motion and did not include rate dependent nonlinearities that develop for heave plates.

In order to capture the full range of nonlinearities high fidelity models are used to calculate the hydrodynamic force on simple 2D geometries, particularly a 2D cylinder with heave plate. These meta-models are Hammerstein model, rate dependent Hammerstein model and rate dependent Kolmogorov-Gabor polynomial (KGP) model. The rate dependent models are models with a nonlinear static block, a hysteresis block (Bouc-Wen model) and a dynamic ARX block (Autoregressive with exogenous model). These meta-models are based on state dependent Bouc-Wen model. Performance of Bouc-Wen model has been evaluated independently and compared with the hydrostatic model. The hydrostatic model provides an input to the dynamic block. It was found that Bouc-Wen model independent of meta-model provides substantial improvement in accuracy of hydrodynamic force.

The comparison between various meta-models was done and it was found that the linear model had difficulty in following peaks in the hydrodynamic force. The data utilised in the case study show the presence of hydrodynamic nonlinearities, which the rate dependent or nonlinear model are able to describe. The HP cylinder has a linear restoring curve, but a very flat bottom with sharp corners and a positive aspect ratio of the plate with the spar can be the source of important nonlinear effects, based on viscosity and vortex shedding. The limitations Hydrostatic, Hysteresis and Hammerstein models, with respect to the nonlinear model are shown in the validation experiment.

The identified hysteresis block showed good performance in predicting the excitation force for all the cases, thereby improving the overall performance of rate dependent models. On the other hand use of nonlinear ARX block either showed

no improvement or reduced accuracy when higher dynamical orders were used. This model is computationally expensive compared to models with linear ARX block. The accuracy of each model depends on the characteristics of input data and a compromise between the accuracy and computational cost determines the choice of model.

6.3 Limitations

The limitations enumerated in this section present boundaries on the application of the developed framework, and also insight on the possible path that advancement in the framework should follow.

1. A major limitation of the modelling approach is that it can only be applied to bodies in single DOF heave only.

2. The modelling approach is limited to single sea spectrum. The model identification process applied to other wave conditions would yield different parameter values. Use of the model could thus be subject to switching between parameter sets between wave conditions.

3. The case studies in this thesis pertained to a characteristic 2D WECs with heave plate, for simplicity. Only cases of a single DoF prescribed heave motion were considered.

4. The assumption made in modelling the excitation force using Bouc-Wen model is that the shape of hysteresis is symmetrical about the force and velocity axis.

6.4 Future work

The elaborate hydrodynamic analysis summarized in this thesis provides an insight into possible and necessary future work. The recommendations presented in this section will advance the model developments for not only hydrodynamics but dynamics of WECs, control and power production assessments.

Multiple DoF analysis An expansion of the current simulation technique in CFD and modelling to include 3D multi-DoF motion is required. In Earlier studies (Tarrant and Meskell, 2016) have pointed out the importance of inclusion of parametrically excited pitch and/or roll motions into hydrodynamic model.

This can be achieved by allowing unrestrained 6-DoF motion of WEC in 3D CFD simulation in hydrodynamic tests. The response of the spar should be recorded and these tests should provide input data for system identification models. The hydrostatic tests should also be designed to determine hydrostatic coefficients when the WEC pitches in quiescent fluid.

Analysis of WEC components The system identification framework developed in this thesis was applied to hydrodynamic forces but the application can be extended to PTO and mooring system, which are essential for evaluation of WEC performance.

Alternate WEC designs Though, in this thesis, the models are identified to describe the hydrodynamics of SRPA geometry, the framework is not limited to SRAPs. Other WEC designs like oscillating surge/pitch converters, overtopping devices, oscillating water column converter *etc.* should be analyzied.

Asymmetric hydrodynamic coefficient The Morison equation with constant coefficient always produces symmetric solution, in which sinusoidal motion has symmetrical force variation in the up and down stroke. This is a limitation for heave plates with asymmetrical shapes. Alternate methods like instantaneous coefficients or phase dependent coefficients to account for asymmetry should be analyzed.

Static nonlinear block The static nonlinearity is approximated by a polynomial in the current work as the focus was straight walled geometries at the interface. But for the geometries that have curved shape at the interface, any other static appropriator can also be utilized. For an efficient identification it is recommended that a linearly parameterized appropriator is used.

Panchromatic spar oscillation One of the limitation in current analysis is that the oscillation of the spar is limited to monochromatic oscillation. This clearly alters the input signal to the system identification model, possible future expansion of current work is inclusion of response of the body to the panchromatic waves.

Recursive Least Squares The computational cost of the data driven model is governed primarily by the data generation process followed by the training algorithm depending on the number and order of ARX structure. Thus when a LS method is required to run online in real time, a new algorithem sould be

developed, since the conputational effort of LS method grows with the number of data sample collected. A recursive formulation of LS method with will reduce the required training time.

Subset selection Due to higher model complexity of KGP model even for moderately sized problems, linear subset selection techniques can be utilized. They allow construction of reduced polynomial model that contained only the most relevant regressors.

Bibliography

M. Afshar. *Numerical wave generation in 0penFOAM*. PhD thesis, Chalmars University of Technology, 2010.

E. B. Agamloh, A. K. Wallace, and A. von Jouanne. Application of fluid–structure interaction simulation of an ocean wave energy extraction device. *Renewable Energy*, 33(4):748 – 757, 2008. ISSN 0960-1481. doi: http://dx.doi.org/10.1016/j.renene.2007.04.010. URL http://www.sciencedirect.com/science/article/pii/S096014810700119X.

M. Alves, D. Causon, B. Child, J. Davidson, B. Elsäßer, C. Ferreira, C. Fitzgerald, M. Folley, D. Forehand, S. Giorgi, J. Kofoed, L. Kregting, C. Mingham, L. Qian, P. Ricci, J. Ringwood, V. Stratigaki, P. Troch, and S. Vaughan. Numerical modelling of wave energy converters. In M. Folley, editor, *Numerical Modelling of Wave Energy Converters*, page ix. Academic Press, 2016. ISBN 978-0-12-803210-7. doi: https://doi.org/10.1016/B978-0-12-803210-7.09995-3. URL http://www.sciencedirect.com/science/article/pii/B9780128032107099953.

M. Anbarsooz, M. Passandideh-Fard, and M. Moghiman. Fully nonlinear viscous wave generation in numerical wave tanks. *Ocean Engineering*, 59(0):73 – 85, 2013. ISSN 0029-8018. doi: http://dx.doi.org/10.1016/j.oceaneng.2012.11.011. URL http://www.sciencedirect.com/science/article/pii/S0029801812004374.

M. Anbarsooz, M. Passandideh-Fard, and M. Moghiman. Numerical simulation of a submerged cylindrical wave energy converter. *Renewable Energy*, 64(0):132 – 143, 2014a. ISSN 0960-1481. doi: http://dx.doi.org/10.1016/j.renene.2013.11.008. URL http://www.sciencedirect.com/science/article/pii/S0960148113005867.

M. Anbarsooz, M. Passandideh-Fard, and M. Moghiman. Numerical simulation of a submerged cylindrical wave energy converter. *Renewable Energy*, 64, 2014b.

doi: 10.1016/j.renene.2013.11.008. URL http://dx.doi.org/10.1016/j.renene.2013.11.008.

A. Babarit. A database of capture width ratio of wave energy converters. *Renewable Energy*, 80(0):610 – 628, 2015. ISSN 0960-1481.

A. Babarit, J. Hals, M. Muliawan, A. Kurniawan, T. Moan, and J. Krokstad. Numerical benchmarking study of a selection of wave energy converters. *Renewable Energy*, 41(0):44 – 63, 2012. ISSN 0960-1481. doi: http://dx.doi.org/10.1016/j.renene.2011.10.002. URL http://www.sciencedirect.com/science/article/pii/S0960148111005672.

G. Bacelli, R. G. Coe, D. Patterson, and D. Wilson. System identification of a heaving point absorber: Design of experiment and device modeling. *Energies*, 10 (4), 2017. ISSN 1996-1073. doi: 10.3390/en10040472. URL https://www.mdpi.com/1996-1073/10/4/472.

W. Bai, M. A. Hannan, and K. K. Ang. Numerical simulation of fully nonlinear wave interaction with submerged structures: Fixed or subjected to constrained motion. *Journal of Fluids and Structures*, 49:534 – 553, 2014. ISSN 0889-9746. doi: https://doi.org/10.1016/j.jfluidstructs.2014.05.011. URL http://www.sciencedirect.com/science/article/pii/S0889974614001170.

S. Beatty, M. Hall, B. Buckham, and P. Wild. Experimental comparison of self-reacting point absorber wec designs. In *10th European Wave and Tidal Conference, EWTEC, Aalborg, Denmark*, 2013.

S. J. Beatty. *Self-Reacting Point Absorber Wave Energy Converters*. PhD thesis, University of Victoria, 2015.

S. J. Beatty, M. Hall, B. J. Buckham, P. Wild, and B. Bocking. Experimental and numerical comparisons of self-reacting point absorber wave energy converters in regular waves. *Ocean Engineering*, 104(0):370 – 386, 2015. ISSN 0029-8018.

S. J. Beatty, B. Bocking, K. Bubbar, B. J. Buckham, and P. Wild. wave energy converters in irregular waves. *Ocean Engineering*, page 16, 2019.

M. A. Bhinder, A. Babarit, L. Gentaz, and P. Ferrant. Potential time domain model with viscous correction and CFD analysis of a generic surging floating wave energy

converter. *International Journal of Marine Energy*, 10:70–96, 2015. ISSN 2214-1669. doi: 10.1016/j.ijome.2015.01.005. URL http://www.sciencedirect.com/science/article/pii/S2214166915000090.

L. Bonfiglio, S. Brizzolara, and C. Chryssostomidis. Added mass and damping of oscillating bodies: a fully viscous numerical approach. In *Recent Advances in Fluid Mechanics, Heat and Mass Transfer and Biology*, 2011.

N. Booij, R. C. Ris, and L. H. Holthuijsen. A third-generation wave model for coastal regions: 1. model description and validation. *Journal of Geophysical Research: Oceans*, 104(C4):7649–7666, 1999. ISSN 2156-2202. doi: 10.1029/98JC02622. URL http://dx.doi.org/10.1029/98JC02622.

R. Bouc. Forced vibration of mechanical systems with hysteresis. 1967.

A. Brown, J. Thomson, and C. Rusch. Hydrodynamic coefficients of heave plates, with application to wave energy conversion. *IEEE Journal of Oceanic Engineering*, pages 1–14, 2017. ISSN 0364-9059, 1558-1691, 2373-7786. doi: 10.1109/JOE.2017.2762258. URL http://ieeexplore.ieee.org/document/8094941/.

K. H. Chan, J. Bao, and W. J. Whiten. Identification of MIMO hammerstein systems using cardinal spline functions. *Journal of Process Control*, 16(7):659 – 670, 2006. ISSN 0959-1524. doi: https://doi.org/10.1016/j.jprocont.2006.01.004. URL http://www.sciencedirect.com/science/article/pii/S0959152406000205.

A. G. Chassiakos, S. F. Masri, A. W. Smyth, and T. K. Caughey. On-Line Identification of Hysteretic Systems. *Journal of Applied Mechanics*, 65(1):194–203, 03 1998. ISSN 0021-8936. doi: 10.1115/1.2789025. URL https://doi.org/10.1115/1.2789025.

L. F. Chen, J. Zang, A. J. Hillis, G. C. J. Morgan, and A. R. Plummer. Numerical investigation of wave–structure interaction using OpenFOAM. *Ocean Engineering*, 88:91 – 109, 2014. ISSN 0029-8018. doi: https://doi.org/10.1016/j.oceaneng.2014.06.003. URL http://www.sciencedirect.com/science/article/pii/S0029801814002169.

B. Chenari, S. S. Saadatian, and A. D. Ferreira. Numerical Modelling of Regular Waves Propagation and Breaking Using Waves2Foam. *Journal of Clean Energy Technologies*, 3(4):276–281, 2015. ISSN 1793821X.

G. Cho, Bacelli and R. G. Coe. Linear and nonlinear system identification of a wave energy converter. In *6th Marine Energy Technology Symposium (METS), Washington, DC*, 2018.

L.-f. Cong and B. Teng. Hydrodynamic characteristics of square heaving plates with opening under forced oscillation. *China Ocean Engineering*, 33(6):637–648, Dec 2019.

R. Courant, K. Friedrichs, and H. Lewy. On the Partial Difference Equations of Mathematical Physics. *IBM J. Res. Dev.*, 11(2):215–234, Mar. 1967. ISSN 0018-8646. doi: 10.1147/rd.112.0215. URL http://dx.doi.org/10.1147/rd.112.0215.

W. Cummins. The impulse response function and ship motions, 1962.

J. R. Dormand and P. J. Prince. A family of embedded runge-kutta formulae. *Journal of Computational and Applied Mathematics*, 6(1):19 – 26, 1980. ISSN 0377-0427. doi: https://doi.org/10.1016/0771-050X(80)90013-3. URL http://www.sciencedirect.com/science/article/pii/0771050X80900133.

E. Eskinat, S. H. Johnson, and W. L. Luyben. Use of hammerstein models in identification of nonlinear systems. *AIChE Journal*, 37(2):255–268, 1991. doi: 10.1002/aic.690370211. URL https://aiche.onlinelibrary.wiley.com/doi/abs/10.1002/aic.690370211.

D. Evans. A theory for wave-power absorption by oscillating bodies. *Journal of Fluid Mechanics*, 1976.

D. Evans, D. Jeffrey, S. Salter, and J. Taylor. Submerged cylinder wave energy device: theory and experiment. *Applied Ocean Research*, 1:3–12, 1979.

T. Falck, K. Pelckmans, J. A. K. Suykens, and B. D. Moor. Identification of wiener-hammerstein systems using LS-SVMs. *IFAC Proceedings Volumes*, 42(10):820 – 825, 2009. ISSN 1474-6670. doi: https://doi.org/10.3182/20090706-3-FR-2004.00136. URL http://www.sciencedirect.com/science/article/pii/S147466701638750X.

A. F. d. O. Falcão. Wave energy utilization: A review of the technologies. *Renewable and Sustainable Energy Reviews*, 14(3):899–918, April 2010. URL https://ideas.repec.org/a/eee/rensus/v14y2010i3p899-918.html.

J. Falnes. A review of wave-energy extraction. *Marine Structures*, 20(4):185 – 201, 2007. ISSN 0951-8339. doi: https://doi.org/10.1016/j.marstruc.2007.09.001. URL http://www.sciencedirect.com/science/article/pii/S0951833907000482.

P. Farrell and J. Maddison. Conservative interpolation between volume meshes by local Galerkin projection. *Computer Methods in Applied Mechanics and Engineering*, 200:89–100, Jan. 2011. doi: 10.1016/j.cma.2010.07.015.

J. Fitzgerald. Position mooring of wave energy converters, 2009.

J. Fitzgerald and L. Bergdahl. Including moorings in the assessment of a generic offshore wave energy converter: A frequency domain approach. *Marine Structures*, 21(1):23 – 46, 2008. ISSN 0951-8339. doi: http://dx.doi.org/10.1016/j.marstruc.2007.09.004. URL http://www.sciencedirect.com/science/article/pii/S0951833907000500.

G. C. Foliente. Hysteresis modeling of wood joints and structural systems. *Journal of Structural Engineering*, 121(6):1013–1022, 1995. doi: 10.1061/(ASCE)0733-9445(1995)121:6(1013).

M. Folley, T. Whittaker, and M. Osterried. The oscillating wave surge converter. In *14th International Offshore and Polar Engineering Conference, Toulon,France*, 2004.

W. Frank. Oscillation of cylinders in or below the free-surface of deep fluids, 1967.

D. Garrett. Coupled analysis of floating production systems. *Ocean Engineering*, 32(7):802 – 816, 2005. ISSN 0029-8018. doi: http://dx.doi.org/10.1016/j.oceaneng.2004.10.010. URL http://www.sciencedirect.com/science/article/pii/S0029801804002094. Deepwater Mooring Systems; Design, Analysis and Materials Deepwater Mooring Systems.

A. Garrido-Mendoza, C., A. Souto-Iglesias, and K. Thiagarajan. Numerical simulation of hydrodynamics of a circular disk oscillating near a seabed. In *32nd International Conference on Ocean, Offshore and Arctic Engineering*, 2013.

S. Giorgi, J. Davidson, and J. Ringwood. Identification of nonlinear excitation force kernels using numerical wave tank experiments. *Proceedings of the 11th European Wave and Tidal Energy Conference*, 2015.

S. Giorgi, J. Davidson, and J. Ringwood. Identification of wave energy device models from numerical wave tank data—part 1: Numerical wave tank identification tests. *IEEE Transactions on Sustainable Energy*, 7(3):1012–1019, July 2016a. ISSN 1949-3037. doi: 10.1109/TSTE.2016.2515512.

S. Giorgi, J. Davidson, and J. Ringwood. Identification of wave energy device models from numerical wave tank data—part 2: Data-based model determination. *IEEE Transactions on Sustainable Energy*, 7(3):1020–1027, July 2016b. ISSN 1949-3037. doi: 10.1109/TSTE.2016.2515500.

G. H. Golub and J. M. Ortega. *Scientific Computing and Differential Equations: An Introduction to Numerical Methods*. Academic Press, Inc., USA, 1st edition, 1991. ISBN 0122892550.

J. M. R. Graham. The forces on sharp-edged cylinders in oscillatory flow at low Keulegan-Carpenter numbers. *Journal of Fluid Mechanics*, 97:331–346, Mar. 1980. doi: 10.1017/S0022112080002595.

C. Guedes, S. and A. Santos, T., editors. *Maritime Technology and Engineering*. CRC Pr I Llc, 2014. ISBN 978-1-138-02727-5.

R. Hansen, M. Kramer, and E. Vidal. Discrete displacement hydraulic power take-off system for the wavestar wave energy converter. *Energies*, 6(8):4001–4044, 2013. ISSN 1996-1073. doi: 10.3390/en6084001. URL `http://www.mdpi.com/1996-1073/6/8/4001`.

Hemida, H. OpenFOAM tutorial: Free surface tutorial using interfoam and rasinterfoam. Technical report, Chalmers University of Technology, April 2008.

P. Higuera, J. L. Lara, and I. J. Losada. Realistic wave generation and active wave absorption for Navier Stokes models: Application to OpenFOAM. *Coastal Engineering*, 71(0):102 – 118, 2013a. ISSN 0378-3839. doi: http://dx.doi.org/10.1016/j.coastaleng.2012.07.002. URL `http://www.sciencedirect.com/science/article/pii/S0378383912001354`.

P. Higuera, J. L. Lara, and I. J. Losada. Simulating coastal engineering processes with OpenFOAM. *Coastal Engineering*, 71(0):119 – 134, 2013b. ISSN 0378-3839. doi: http://dx.doi.org/10.1016/j.coastaleng.2012.06.002. URL `http://www.sciencedirect.com/science/article/pii/S0378383912001093`.

C. W. Hirt and B. D. Nichols. Volume of fluid (VOF) method for the dynamics of free boundaries. 39(1):201 – 225, 1981. ISSN 0021-9991. doi: https://doi.org/10.1016/0021-9991(81)90145-5. URL http://www.sciencedirect.com/science/article/pii/0021999181901455.

R. Isermann and M. Münchhof. *Identification of dynamic systems: an introduction with applications*. Springer, 2011. ISBN 978-3-540-78878-2 978-3-540-78879-9. OCLC: 845689930.

R. I. Issa. Solution of implicitly discretized fluid flow equations by operator-splitting. *Journal of Computational Physics*, 62:40–65, 1986.

N. Jacobsen, D. Fuhrman, and J. Fredsøe. A wave generation toolbox for the open source cfd library: OpenFoam. *International Journal for Numerical Methods in Fluids*, 70(9):1073–1088, 2012. ISSN 0271-2091. doi: 10.1002/fld.2726.

L. Johanning, G. H. Smith, and J. Wolfram. Measurements of static and dynamic mooring line damping and their importance for floating {WEC} devices. *Ocean Engineering*, 34(14–15):1918 – 1934, 2007. ISSN 0029-8018. doi: http://dx.doi.org/10.1016/j.oceaneng.2007.04.002. URL http://www.sciencedirect.com/science/article/pii/S0029801807001126.

H. G. Keulegan and C. H. Lloyd. Forces on cylinders and plates in an oscillating fluid. *Journal of Research of the National Bureau of Standards*, 41(5):423– 441, May 1958.

N. Kwok, Q. Ha, M. Nguyen, J. Li, and B. Samali. Bouc–wen model parameter identification for a MR fluid damper using computationally efficient GA. *ISA Transactions*, 46(2):167–179, 2007. ISSN 00190578. doi: 10.1016/j.isatra.2006.08.005. URL https://linkinghub.elsevier.com/retrieve/pii/S0019057807000237.

M. Lake, H. He, A. W. Troesch, M. Perlin, and K. P. Thiagarajan. Hydrodynamic Coefficient Estimation for TLP and Spar Structures . *Journal of Offshore Mechanics and Arctic Engineering*, 122(2):118–124, 12 1999.

L. Landweber and M. C. Macagno. Added masses of two dimensional forms by conformal mapping. *Journal of Ship Research*, 10:109–116, 1967.

M. Lawrynczuk. On-line set-point optimisation and predictive control using neural hammerstein models. *Chemical Engineering Journal*, 166(1):269 – 287, 2011. ISSN 1385-8947. doi: https://doi.org/10.1016/j.cej.2010.07.065. URL http://www.sciencedirect.com/science/article/pii/S1385894710006844.

M. Lewin. The effect of vertical barriers on progressing waves. *Journal of Mathematics and Physics*, 42(1-4):287–300, 1963. doi: 10.1002/sapm1963421287. URL https://onlinelibrary.wiley.com/doi/abs/10.1002/sapm1963421287.

J. Li, S. Liu, M. Zhao, and B. Teng. Experimental investigation of the hydrodynamic characteristics of heave plates using forced oscillation. *Ocean Engineering*, 66:82 – 91, 2013. ISSN 0029-8018. doi: https://doi.org/10.1016/j.oceaneng.2013.04.012. URL http://www.sciencedirect.com/science/article/pii/S0029801813001595.

Y. Li and M. Lin. Wave-body interactions for a surface-piercing body in water of finite depth. *Journal of Hydrodynamics, Ser. B*, 22(6):745–752, Dec. 2010. ISSN 1001-6058.

Y. Li and M. Lin. Regular and irregular wave impacts on floating body. *Ocean Engineering*, 42:93–101, Mar. 2012. ISSN 0029-8018.

H. Liu, F. Yan, F. Jing, J. Ao, Z. Han, and F. Kong. Numerical and experimental investigation on a moonpool-buoy wave energy converter. *Energies*, 13(9), 2020. ISSN 1996-1073. doi: 10.3390/en13092364. URL https://www.mdpi.com/1996-1073/13/9/2364.

P. A. Madsen. Higher-order boussinesq-type equations for surface gravity waves: derivation and analysis. *Philosophical Transactions of The Royal Society A: Mathematical, Physical and Engineering Sciences*, 356:3123–3181, 1998. doi: 10.1098/rsta.1998.0309.

S. Malenica, R. E. TAYLOR, and J. B. HUANG. Second-order water wave diffraction by an array of vertical cylinders. *Journal of Fluid Mechanics*, 390:349–373, 1999. doi: 10.1017/S0022112099005273.

D. S. Marquez. *An Extended Mixture Model for the Simultaneous Treatment of Short and Long Scale Interfaces*. PhD thesis, Facultad de Ingenieria y Ciencias Hidricas, Universidad Nacional del Litoral, 2013.

S. Mayer, A. Garapon, and L. S. Sorensen. A fractional step method for unsteady free-surface flow with applications to non-linear wave dynamics. *International Journal for Numerical Methods in Fluids*, 28(2):293–315, 1998. ISSN 1097-0363. doi: 10.1002/(SICI)1097-0363(19980815)28:2⟨293::AID-FLD719⟩3.0.CO;2-1.

I. D. Mayergoyz. *Mathematical models of hysteresis*. Springer-Verlag New York, 1993.

C. C. Mei. RADIATION AND SCATTERING OF TRANSIENT GRAVITY WAVES BY VERTICAL PLATES. *The Quarterly Journal of Mechanics and Applied Mathematics*, 19(4):417–440, 01 1966. ISSN 0033-5614. doi: 10.1093/qjmam/19.4.417. URL `https://doi.org/10.1093/qjmam/19.4.417`.

C. C. Mei. Numerical methods in water-wave diffraction and radiation. *Annual Review of Fluid Mechanics*, 10(1):393–416, 1978.

G. Morgan, J. Zang, D. Greaves, A. Heath, C. Whitlow, and J. Young. Using the rasinterfoam cfd model for wave transformation and coastal modelling. *Coastal Engineering Proceedings*, 1(32):23, 2011. ISSN 2156-1028. URL `https://icce-ojs-tamu.tdl.org/icce/index.php/icce/article/view/1240`.

J. R. Morison, M. P. O'Brain, J. J. W., and S. A. Schaaf. The force exerted by surface waves on piles. *Journal of Petroleum Technology*, 2:149–154, 1950. doi: 10.2118/950149-G.

O. Nelles. *Nonlinear System Identification: From Classical Approaches to Neural Networks and Fuzzy Models*. Springer, 2001.

J. Newman. The interaction of stationary vessels with regular waves. *Proc. 11th Sympossium of Naval Hydrodynamics*, 1976.

S. Osher and J. Sethian. Fronts propagation with curvature dependent speed: Algorithms based on hamilton jacobi formulations. *Journal of Computational Physics*, 79(12-49), 1988. URL `http://dx.doi.org/10.1016/0021-9991(88)90002-2`.

K. J. Paik. *Simulation of fluid-structure interaction for surface ships with linear/nonlinear deformations*. PhD thesis, The University of Iowa, 2010.

J. Palm, C. Eskilsson, G. Moura Paredes, and L. Bergdahl. Cfd simulation of a moored floating wave energy converter. In *10th European Wave and Tidal Energy Conference*, 2013.

S. Patankar. *Numerical Heat Transfer and fluid flow*. Series in computational and physical processes in mechanics and thermal sciences. Hemisphere Publishing Company, 1980.

M. Penalba, G. Giorgi, and J. V. Ringwood. Mathematical modelling of wave energy converters: A review of nonlinear approaches. *Renewable and Sustainable Energy Reviews*, 78:1188–1207, 2017a. ISSN 1364-0321. doi: 10.1016/j.rser.2016.11.137. URL http://www.sciencedirect.com/science/article/pii/S1364032116308784.

M. Penalba, A. Mérigaud, J.-C. Gilloteaux, and J. V. Ringwood. Influence of nonlinear froude–krylov forces on the performance of two wave energy points absorbers. *Journal of Ocean Engineering and Marine Energy*, 3(3):209–220, 2017b. ISSN 2198-6444, 2198-6452. doi: 10.1007/s40722-017-0082-x. URL http://link.springer.com/10.1007/s40722-017-0082-x.

R. Pintelon and J. Schoukens. System identification; a frequency domain approach, 2d ed.: [1]. *Reference and Research Book News*, 27(3), 06 2012. Copyright - Copyright Book News, Inc. Jun 2012; Last updated - 2013-07-02.

J. Ramos and C. Guedes Soares. On the assessment of hydrodynamic coefficients of cylinders in heaving. *Ocean Engineering*, 24(8):743–763, Aug. 1997. ISSN 0029-8018.

L. F. Richardson and J. A. Gaunt. Viii. the deferred approach to the limit. *Philosophical Transactions of the Royal Society of London. Series A, Containing Papers of a Mathematical or Physical Character*, 226(636-646):299–361, 1927. doi: 10.1098/rsta.1927.0008. URL https://royalsocietypublishing.org/doi/abs/10.1098/rsta.1927.0008.

J. Ringwood, J. Davidson, and S. Giorgi. Identifying models using recorded data. In *Numerical Modelling of Wave Energy Converters*, pages 123–147. Elsevier, 2016. ISBN 978-0-12-803210-7. doi: 10.1016/B978-0-12-803210-7.00007-4. URL http://linkinghub.elsevier.com/retrieve/pii/B9780128032107000074.

A. Roy, S. Beatty, V. , D. Steinke, R. Nicoll, and B. Buckham. Efficient time-domain hydrodynamic simulation of a rigid body. In *ASME 2015 34th International Conference on Ocean, Offshore and Arctic Engineering , OMAE2015, St. John's, Newfoundland, Canada*, 2015.

H. Rusche. *Computational fluid dynamics od dispersed two-phase flows at high phase fraction*. PhD thesis, Imperial College of Science, Technology and Medicine, 2002.

J. Sanders, J. E. Dolbow, P. J. Mucha, and T. A. Laursen. A new method for simulating rigid body motion in incompressible two-phase flow. *International Journal for Numerical Methods in Fluids*, 67(6):713–732, 2011. doi: 10.1002/fld.2385. URL https://onlinelibrary.wiley.com/doi/abs/10.1002/fld.2385.

T. Sarpkaya and M. Isaacson. *Mechanics of Wave Forces on Offshore Structures*. Van Nostrand Reinhold, New York, NY., 1981.

J. Schoukens, T. Dobrowiecki, and R. Pintelon. Parametric and nonparametric identification of linear systems in the presence of nonlinear distortions-a frequency domain approach. *IEEE Transactions on Automatic Control*, 43(2):176–190, 1998.

R. P. Shaw. An Outer Boundary Integral Equation Applied to Transient Wave Scattering in an Inhomogeneous Medium. *Journal of Applied Mechanics*, 42 (1):147–152, 03 1975. ISSN 0021-8936. doi: 10.1115/1.3423506. URL https://doi.org/10.1115/1.3423506.

L. Shen and E.-S. Chan. Numerical simulation of fluid–structure interaction using a combined volume of fluid and immersed boundary method. 35(8), 2008. ISSN 0029-8018. doi: https://doi.org/10.1016/j.oceaneng.2008.01.013. URL http://www.sciencedirect.com/science/article/pii/S0029801808000139.

T. Shih, W. Liou, A. Shabbir, Z. Yang, and J. Zhu. A new k-epsilon eddy viscosity model for high reynolds number turbulent flows. *Computers and Fluids*, Jan. 1995.

M. Srokosz and D. Evans. A theory for wave-power absorption by two independently oscillating bodies. *Journal of Fluid Mechanics*, 90:337–62, 1979.

G. Stokes. On the theory of oscillatory waves. *Transactions of the Cambridge Philosophical Society*, 1847.

S. Talatahari, A. Kaveh, and N. Mohajer Rahbari. Parameter identification of bouc-wen model for MR fluid dampers using adaptive charged system search optimization. *Journal of Mechanical Science and Technology*, 26(8):2523–2534, 2012. ISSN 1738-494X, 1976-3824. doi: 10.1007/s12206-012-0625-y. URL http://link.springer.com/10.1007/s12206-012-0625-y.

L. Tao, K. Thiagarajan, and L. Cheng. On the parametric dependence of springing damping of tlp and spar columns. *Applied Ocean Research*, 22(5):281 – 294, 2000. ISSN 0141-1187. doi: http://dx.doi.org/10.1016/S0141-1187(00)00017-1. URL http://www.sciencedirect.com/science/article/pii/S0141118700000171.

K. Tarrant and C. Meskell. Investigation on parametrically excited motions of point absorbers in regular waves. *Ocean Engineering*, 111:67–81, 2016. ISSN 0029-8018. doi: 10.1016/j.oceaneng.2015.10.041. URL http://www.sciencedirect.com/science/article/pii/S0029801815005880.

H. Versteeg and W. Malalasekera. *An Introduction to Computational Fluid Dynamics: The Finite Volume Method*. Pearson Education Limited, 2007.

T. Vyzikas, E. Ransley, M. Hann, D. Magagna, D. Greaves, D. Simmonds, V. Magar, and D. Conley. *Integrated Numerical Modelling System for Extreme Wave Events at the Wave Hub Site*, pages 316–325. ICE Publishing, Oct. 2013. doi: 10.1680/fsts.59757.034. URL https://www.icevirtuallibrary.com/doi/abs/10.1680/fsts.59757.034.

Z. Wang, Z. Zhang, J. Mao, and Kemin Zhou. A hammerstein-based model for rate-dependent hysteresis in piezoelectric actuator. In *2012 24th Chinese Control and Decision Conference (CCDC)*, pages 1391–1396. IEEE, 2012. ISBN 978-1-4577-2074-1 978-1-4577-2073-4 978-1-4577-2072-7. doi: 10.1109/CCDC.2012.6244223. URL http://ieeexplore.ieee.org/document/6244223/.

H. G. Weller, G. Tabor, H. Jasak, and C. Fureby. A tensorial approach to computational continuum mechanics using object-oriented techniques. *Comput. Phys.*, 12(6):620–631, Nov. 1998. ISSN 0894-1866. doi: 10.1063/1.168744. URL http://dx.doi.org/10.1063/1.168744.

Y. K. Wen. Method for random vibration of hysteretic systems. *Journal of The Engineering Mechanics Division*, 1976. URL https://ci.nii.ac.jp/naid/10014689922/en/.

G. Weymouth. *Learning Based Computational Models for Breaking BowWaves Based on New Boundary Immersion Approaches*. PhD thesis, MIT, 2008.

G. Weymouth, D. G. Dommermuth, K. Hendrickson, and D. K. P. Yue. Advances in cartesian-grid methods for computational ship hydrodynamics. In *26th Symposium*

on Naval Hydrodynamics, volume 3 of *26th Symposium on Naval Hydrodynamics, Rome, Italy*, 09 2006.

C. Windt, J. Davidson, P. Schmitt, and J. Ringwood. On the assessment of numerical wave makers in CFD simulations. *Journal of Marine Science and Engineering*, 7 (2):47, 2019. ISSN 2077-1312. doi: 10.3390/jmse7020047. URL http://www.mdpi.com/2077-1312/7/2/47.

R. W. Yeung and Y. Jiang. Effects of shaping on viscous damping and motion of heaving cylinders. In *International Conference on Offshore Mechanics and Arctic Engineering*, volume 3 of *International Conference on Offshore Mechanics and Arctic Engineering*, pages 825–836, 06 2011.

Y.-H. Yu and Y. Li. Reynolds-averaged navier–stokes simulation of the heave performance of a two-body floating-point absorber wave energy system. *Computers and Fluids*, 73(Complete):104–114, 2013.

Z. Yu and J. Falnes. State-space modelling of a vertical cylinder in heave. *Applied Ocean Research*, 17(5):265 – 275, 1995. ISSN 0141-1187. doi: https://doi.org/10.1016/0141-1187(96)00002-8. URL http://www.sciencedirect.com/science/article/pii/0141118796000028.

A. Zurkinden, F. Ferri, S. Beatty, J. Kofoed, and M. Kramer. Non-linear numerical modeling and experimental testing of a point absorber wave energy converter. *Ocean Engineering*, 78:11–21, 2014. ISSN 00298018. doi: 10.1016/j.oceaneng.2013.12.009. URL https://linkinghub.elsevier.com/retrieve/pii/S0029801813004393.

Appendix A

Numerical tank verification study

The CFD based NWTs used for system identification are assessed on performance parameter like accuracy by doing a sensitivity analysis. The methodology of sensitivity analysis adapted in this thesis involves following steps.

1. Identifying the parameters for sensitivity analysis.
2. Identifying various metric to evaluate the accuracy of various NWTs.
3. Analyzing accuracy of various NWTs.

A.1 Parameters for sensitivity analysis

Modelling inaccuracies in NWTs can be attributed to various factors. In this thesis only uncertainty due to spatial discretization and numerical wave damping has been considered. For other parameters like solver settings and solution schemes, Windt et al. (2019) and previous experiences have been considered. The spatial and temporal discretization level (*i.e.*, cell size and time step) affect the solution of the flow quantities in NWTs. Convergence studies must be performed inorder to quantify the influence of discretization. The required spatial discretisation is largely driven by the advection method, and can be determined using monochromatic wave propagation. Since the spatial and temporal discretization are connected through the Courant-Friedrichs-Lewy (CFL) condition Courant et al. (1967), temporal convergences was assured by maintaining Courant Number below 0.8 every where in the domain.

A.2 Metrics for sensitivity analysis

Metric-1

The wave height is evaluated with three different spatial discretization levels and the first error metric utilized is grid uncertainty U

$$U = \frac{U_a}{H_f} * 100\% \tag{A.1}$$

where U_a is the absolute grid uncertainty and H_f is the mean wave height for the finest grid size. From the solution for the finest (H_f), intermediate (H_m) and coarsest (H_c) discretisation size, the discrimination ratio, R_D, is determined as follows:

$$R_D = \frac{H_f - H_m}{H_m - H_c} \tag{A.2}$$

The difference between various convergence types, is represented by R_D. Neglecting any case in which divergence is encountered, the absolute grid uncertainty U_a can be calculated for monotonic convergence ($0 < R_D < 1$) and oscillatory convergence ($R_D < 0$ and abs $\mid R_D \mid < 1$). For monotonic and oscillatory convergence, the value of U_a can be calculated by Eqs. (A.3) and (A.4), respectively:

$$U_a = F_s \times \frac{H_f - H_m}{2^p - 1} \tag{A.3}$$

$$U_a = 0.5 \times F_s \times \mid \max(H_f, H_m, H_c) - \min(H_f, H_m, H_c) \mid \tag{A.4}$$

where, F_s is factor of safety ($= 1.5$) and p is the order of accuracy from Richardson extrapolation (Richardson and Gaunt, 1927) given by:

$$p = \frac{\ln R_D}{\ln 2} \tag{A.5}$$

Metric-2

Relative deviation of the phase averaged wave height for various meshes with respect to the mean wave height of the finest mesh is another metric used to quantify the sensitivity of the solution to the mesh considered. The relative deviation is given by

following equation:

$$d\bar{H}_m = \frac{\bar{H}_m - \bar{H}_f}{\bar{H}_f} \times 100\% \tag{A.6}$$

Metric-3

The evaluation metric for the generated wave height is the mean error and standard deviation of the measured phase averaged wave height, $\bar{H}(x)$, and the desired theoretical value H given by:

$$\bar{\epsilon}_{\bar{H}^{\pm}} = \frac{\bar{H}^{\pm}(x) - H}{H} \times 100\% \tag{A.7}$$

where the upper and lower bounds of the mean wave height $\bar{H}^{\pm}(x)$ is given by:

$$\bar{H}^{\pm}(x) = \bar{H}(x) \pm \sigma_{\bar{H}(x)}(x) \tag{A.8}$$

where $\sigma_{\bar{H}(x)}x$ is the standard deviation of wave height calculated by recording the $\eta\ (\lambda, t)$ at over the entire duration of simulation

A.3 Grid independence study-3D Mesh

The first test condition was used to conduct the grid independence study and was assumed valid for all test cases. In this case three different domains with respect to number of grid points have been used. The total cell count for the different grids are approximately 2 million, 2.5 million and 5 million. Another difference between the cases is the degree of resolution of the moon pool region between the spar and float. The region between spar and float is important because it has been found in previous study (Beatty et al., 2015), that linear models could not resolve the flow features in this region. The AMI is also located in this region and accurate prediction of fluid properties across the AMI boundary is important as the interpolation accuracy depends on the gradient of the fluid properties. The distribution of node points between float and spar in the radial direction for the described cases are a uniform distribution of 20 nodes, 24 nodes and 40 nodes respectively. The simulation was done for 3 seconds and the convergence of dynamic forces to its arithmetic mean is presented for spar and float in Figure A.1.

The sensitivity of the force prediction on the distribution and number of cells in

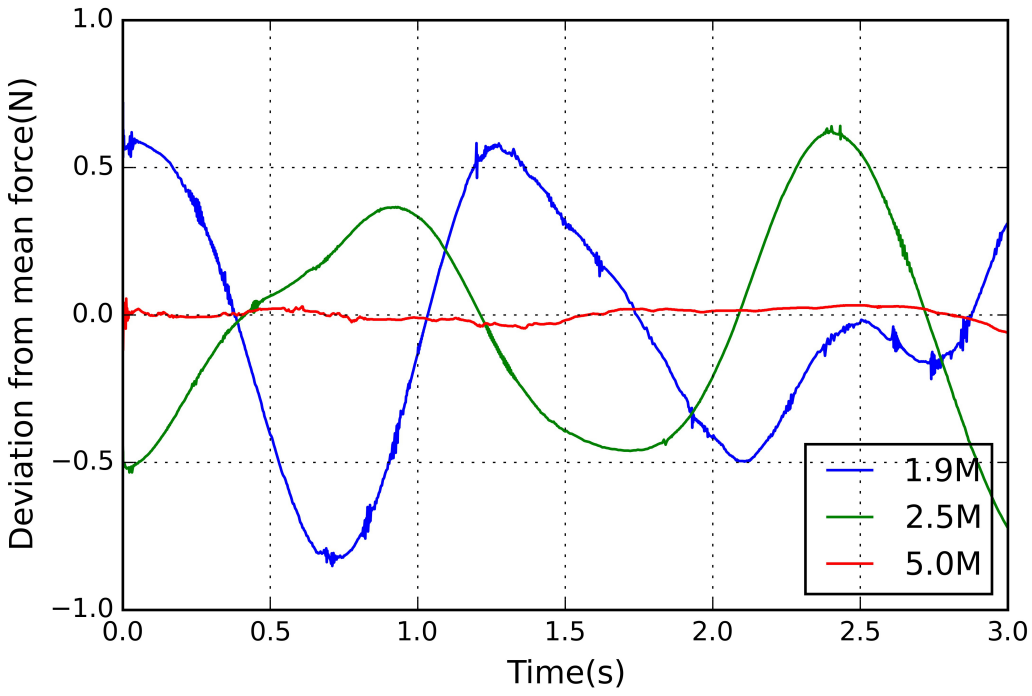

Figure A.1: Convergence of force on spar for different grid densities. M stands for millions of cells

the domain is evident from Figure A.1. It can be seen that the deviation is minimum for the case with 5 million cells. Hence this grid was considered as an acceptable grid for the other test cases, and the solution obtained from this case has been considered as the initial condition for other cases.

Appendix B

Hydrodynamic forces on WEC B

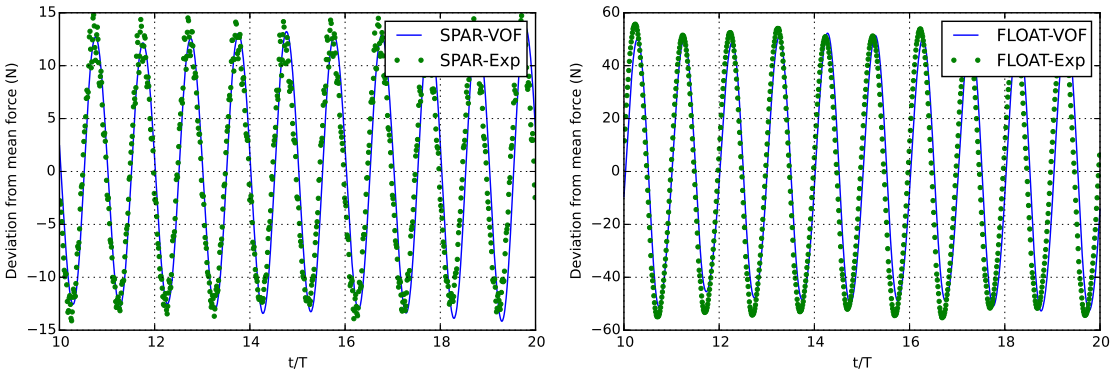

(a) Spar (b) Float

Figure B.1: Comparison between CFD and experimental results of hydrodynamic force values on WEC B oscillating at $\omega = 4.04\ rad/s$

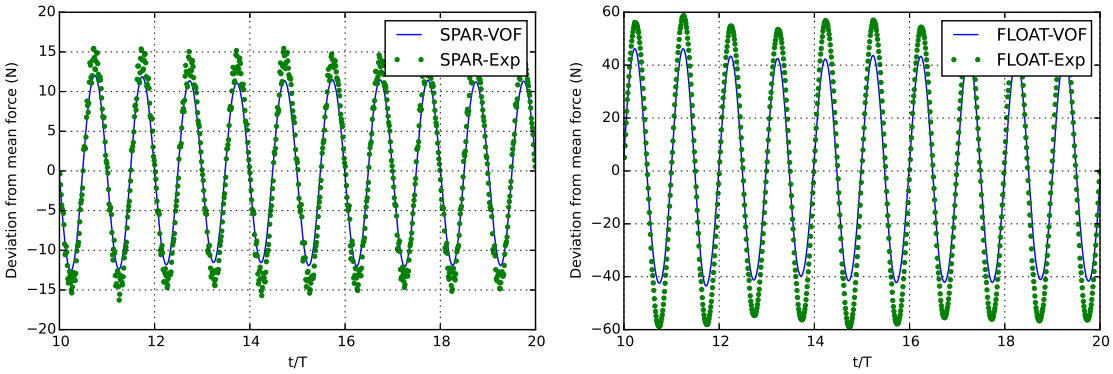

(a) Spar (b) Float

Figure B.2: Comparison between CFD and experimental results of hydrodynamic force values on WEC B oscillating at $\omega = 3.72\ rad/s$

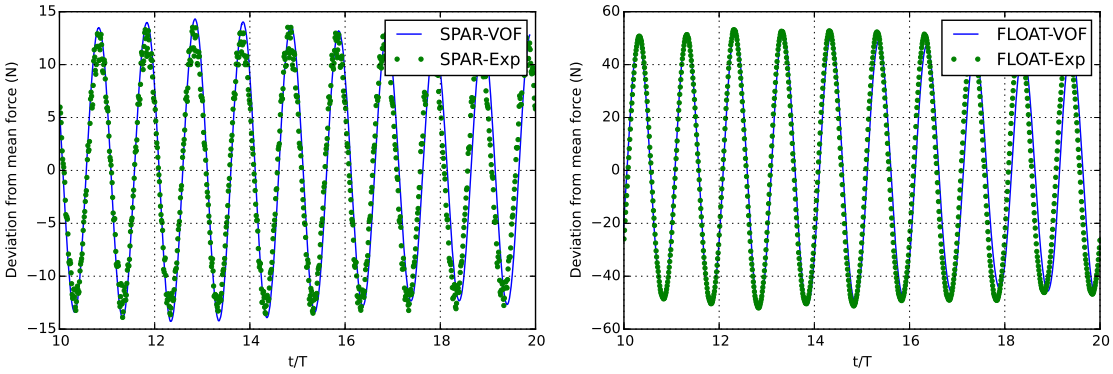

(a) Spar (b) Float

Figure B.3: Comparison between CFD and experimental results of hydrodynamic force values on WEC B oscillating at $\omega = 3.47\ rad/s$

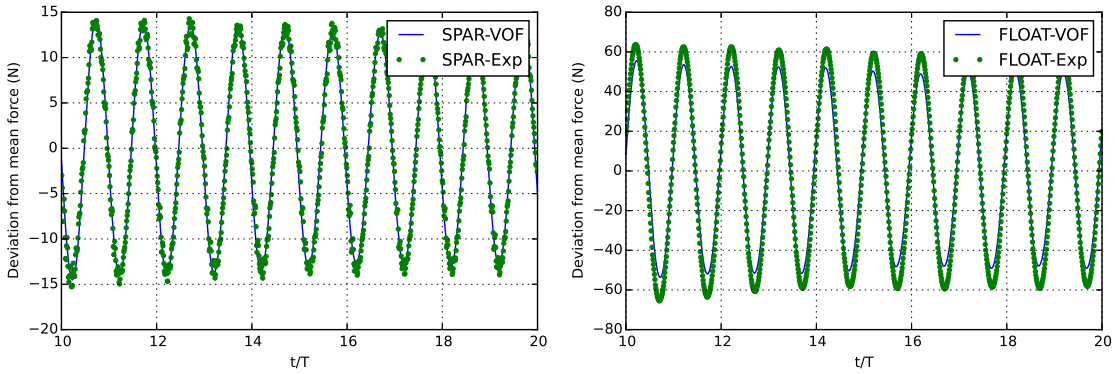

(a) Spar (b) Float

Figure B.4: Comparison between CFD and experimental results of hydrodynamic force values on WEC B oscillating at $\omega = 3.15\ rad/s$

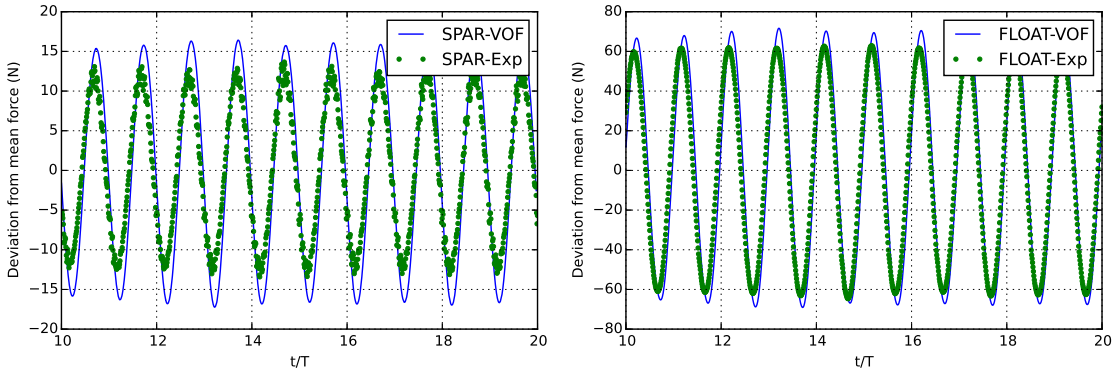

(a) Spar (b) Float

Figure B.5: Comparison between CFD and experimental results of hydrodynamic force values on WEC B oscillating at $\omega = 2.90\ rad/s$

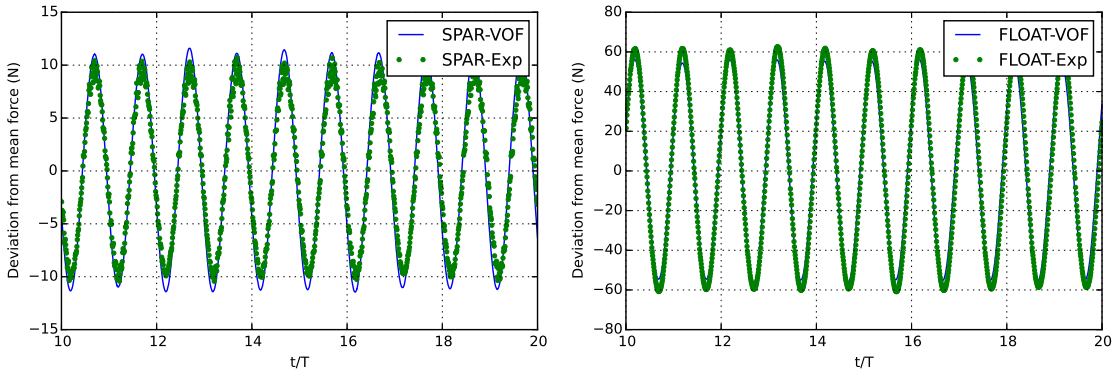

(a) Spar (b) Float

Figure B.6: Comparison between CFD and experimental results of hydrodynamic force values on WEC B oscillating at $\omega = 2.65\ rad/s$

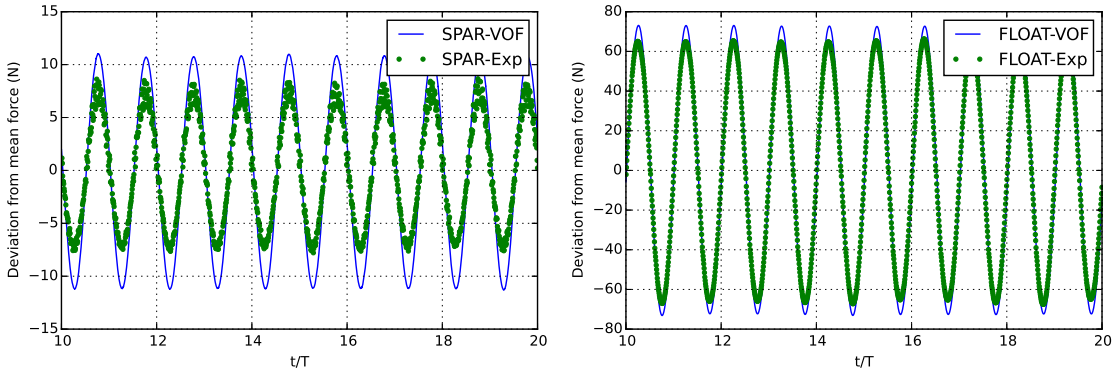

(a) Spar (b) Float

Figure B.7: Comparison between CFD and experimental results of hydrodynamic force values on WEC B oscillating at $\omega = 2.34\ rad/s$

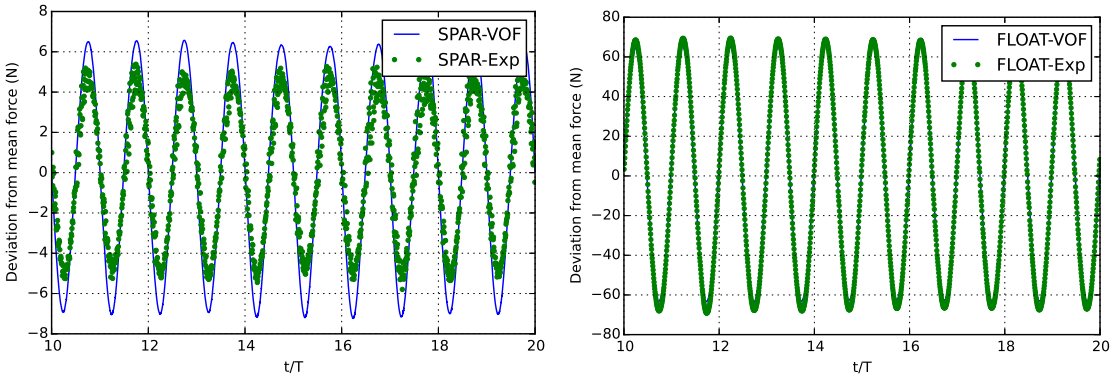

(a) Spar (b) Float

Figure B.8: Comparison between CFD and experimental results of hydrodynamic force values on WEC B oscillating at $\omega = 2.08\ rad/s$

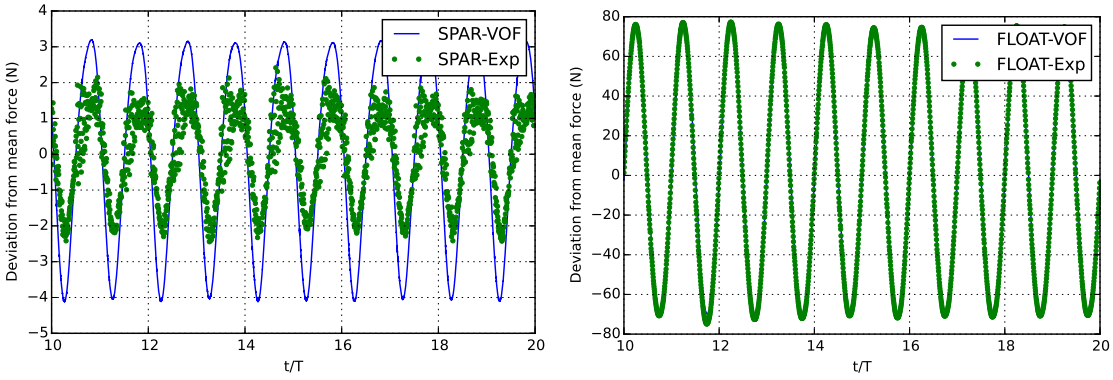

(a) Spar (b) Float

Figure B.9: Comparison between CFD and experimental results of hydrodynamic force values on WEC B oscillating at $\omega = 1.77\ rad/s$

Appendix C

Dynamic order and delay constants

The plots for variation of NRMSE for HP cylinder oscillating at 0.15 m, 0.05 m and 0.00 m for Range 1 is shown in Figure C.2, Figure C.4 and Figure C.5 respectively. Another relevent plot for Range 2 of HP cylinder oscillating at 0.15 m is shown in Figure C.3. The optimal values obtained from these plots have been tabulated in Table 5.4, Table 5.5, Table 5.6 and Table 5.7, respectively. The variation of NRMSE for HP cylinder (see Figure 4.2) oscillating at $amp = 0.25\ m$ and $1.25\ rad/s$ for Range 1 (see Section 5.4.1) is shown in Figure C.1. The plot corresponding to Range 2 (see Section 5.4.2) has been discussed in Chapter 5, Section 5.4.4 and shown in Figure 5.7.

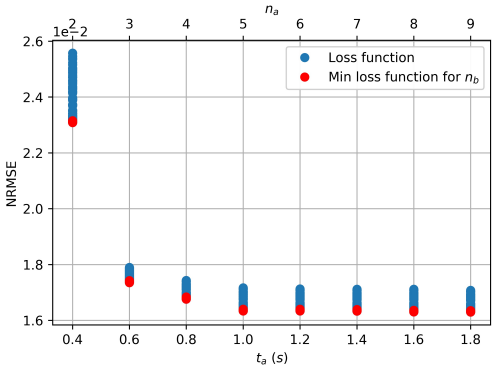

(a) NRMSE Vs n_a (Rate dependent Hammerstein model)

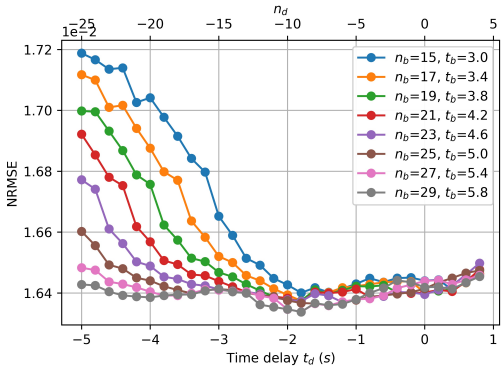

(b) NRMSE Vs n_d (Rate dependent Hammerstein model)

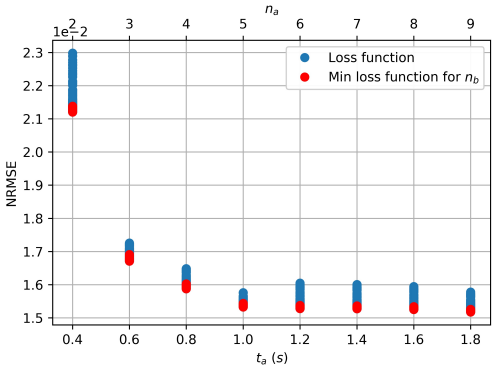

(c) NRMSE Vs n_a (Rate dependent KGP model)

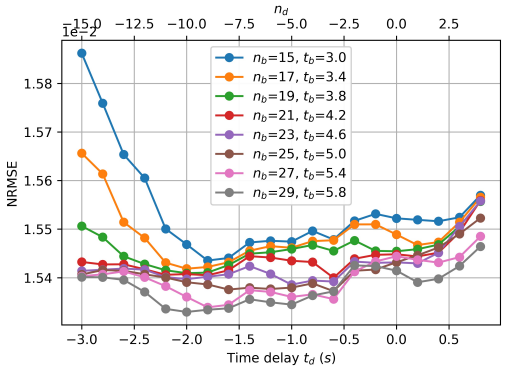

(d) NRMSE Vs n_d (Rate dependent KGP model)

Figure C.1: NRMSE for HP cylinder oscillating at $amp = 0.25\ m$ and $\omega = 1.25\ rad/s$ for realization $R1$ and Range 1, illustrating a comparison between all the system identification models used in this thesis. NRMSE is calculated between the hydrodynamic force values from CFD and model. $n_a - t_a$ and $n_d - t_d$ relationship is provided in Section 5.4

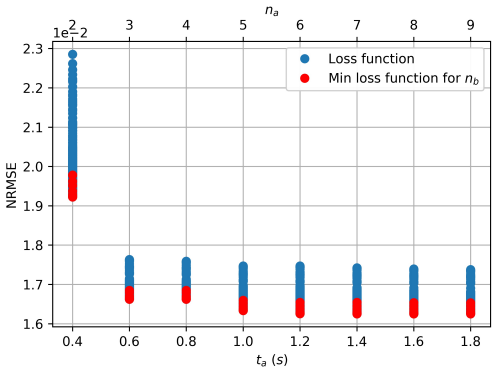

(a) NRMSE Vs n_a (Hammerstein model)

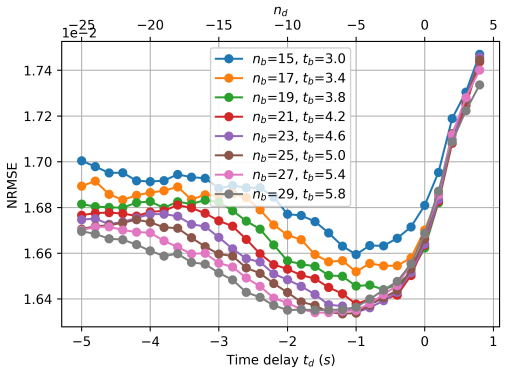

(b) NRMSE Vs n_d (Hammerstein model)

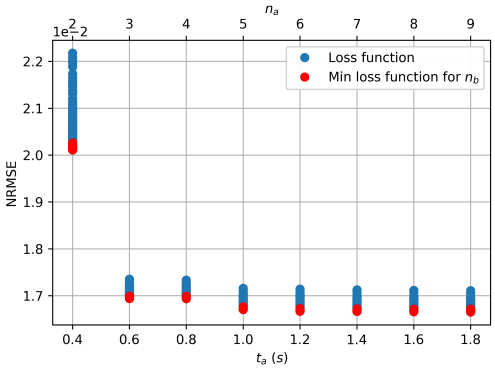

(c) NRMSE Vs n_a (Rate dependent Hammerstein model)

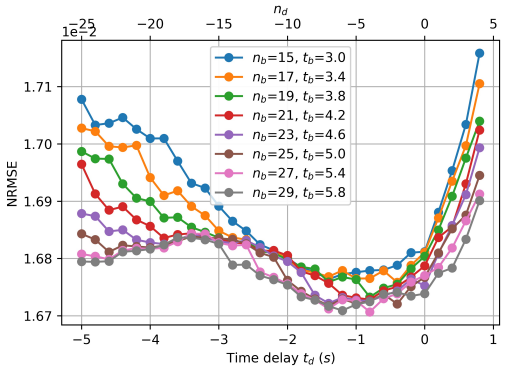

(d) NRMSE Vs n_d (Rate dependent Hammerstein model)

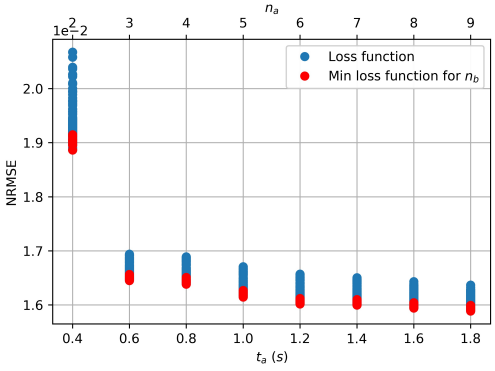

(e) NRMSE Vs n_a (Rate dependent KGP model)

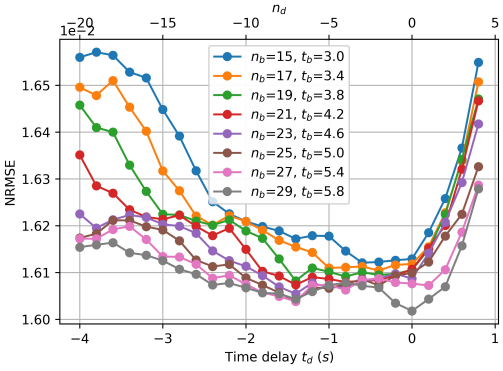

(f) NRMSE Vs n_d (Rate dependent KGP model)

Figure C.2: NRMSE for HP cylinder oscillating at $amp = 0.15\ m$ and $\omega = 1.25\ rad/s$ for realization $R1$ and Range 1, illustrating a comparison between all the system identification models used in this thesis

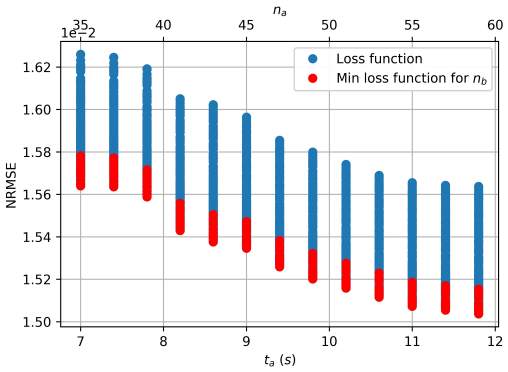

(a) NRMSE Vs n_a (Hammerstein model)

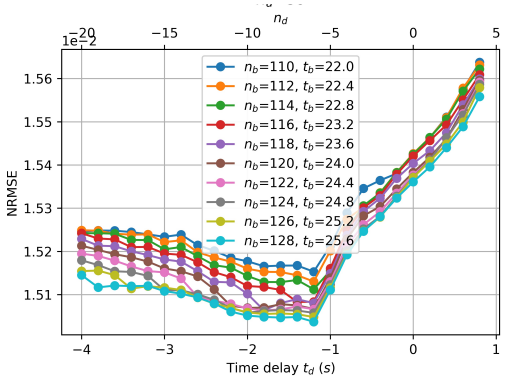

(b) NRMSE Vs n_d (Hammerstein model)

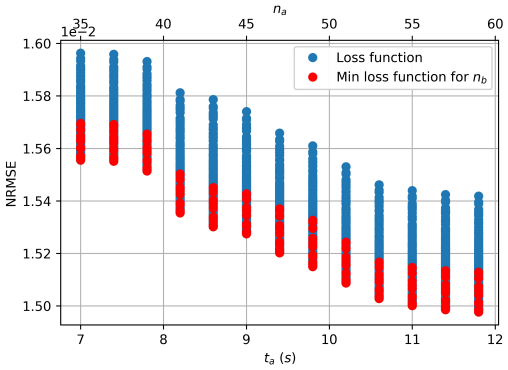

(c) NRMSE Vs n_a (Rate dependent Hammerstein model)

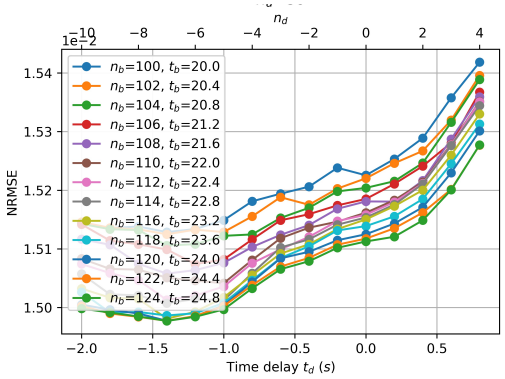

(d) NRMSE Vs n_d (Rate dependent Hammerstein model)

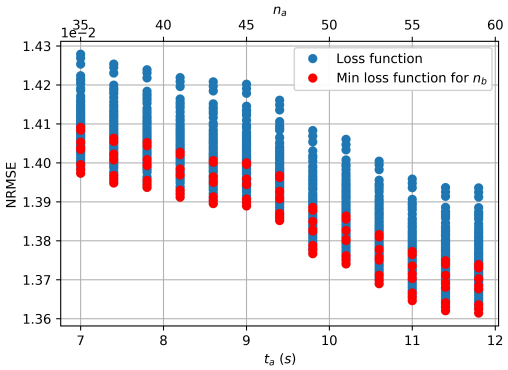

(e) NRMSE Vs n_a (Rate dependent KGP model)

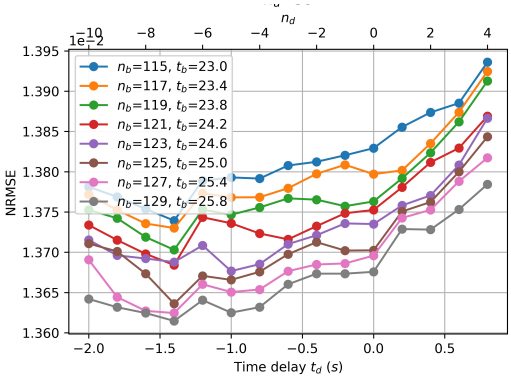

(f) NRMSE Vs n_d (Rate dependent KGP model)

Figure C.3: NRMSE for HP cylinder oscillating at $amp = 0.15\ m$ and $\omega = 1.25\ rad/s$ for realization $R1$ and Range 2, illustrating a comparison between all the system identification models used in this thesis

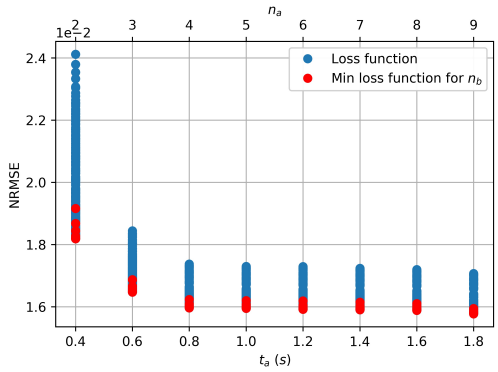

(a) NRMSE Vs n_a (Hammerstein model)

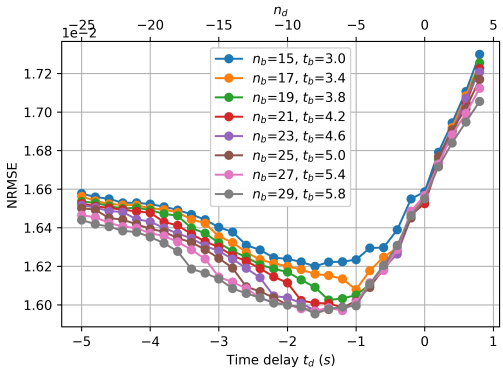

(b) NRMSE Vs n_d (Hammerstein model)

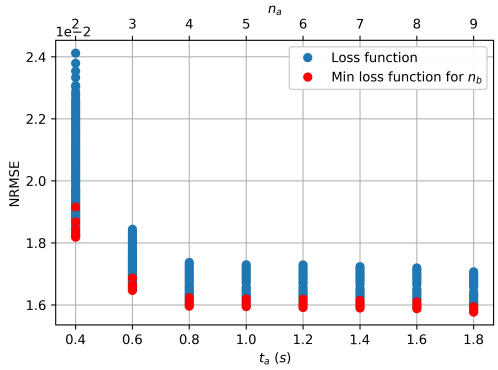

(c) NRMSE Vs n_a (Rate dependent Hammerstein model)

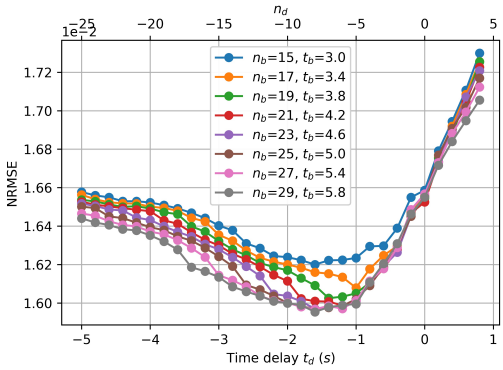

(d) NRMSE Vs n_d (Rate dependent Hammerstein model)

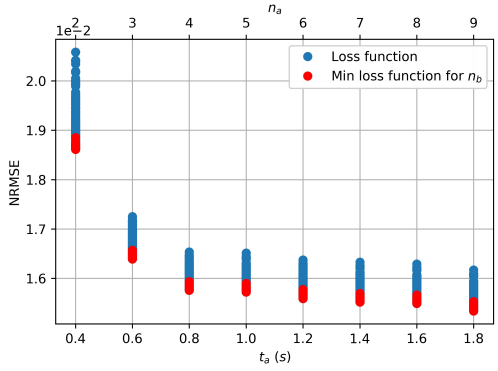

(e) NRMSE Vs n_a (Rate dependent KGP model)

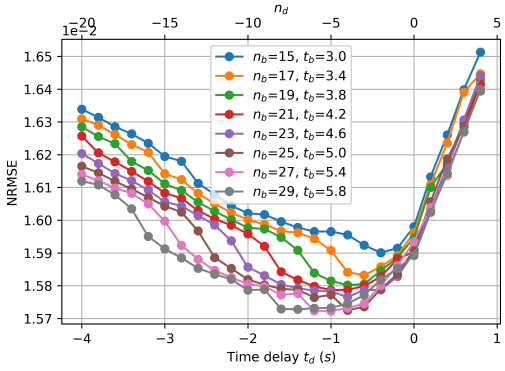

(f) NRMSE Vs n_d (Rate dependent KGP model)

Figure C.4: NRMSE for HP cylinder oscillating at $amp = 0.05\ m$ and $\omega = 1.25\ rad/s$ for realization $R1$ and Range 1, illustrating a comparison between all the system identification models used in this thesis

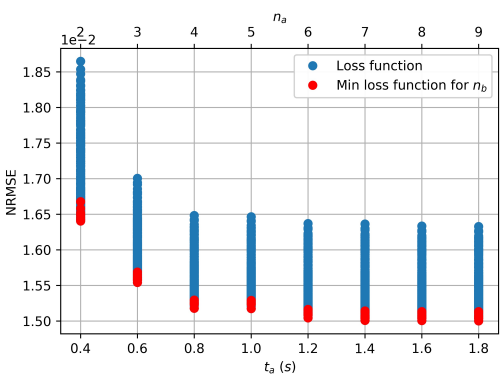

(a) NRMSE Vs n_a (Hammerstein model)

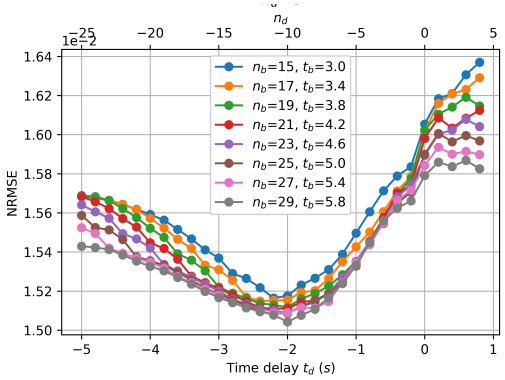

(b) NRMSE Vs n_d (Hammerstein model)

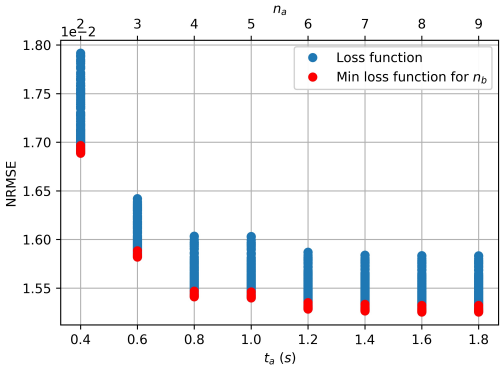

(c) NRMSE Vs n_a (Rate dependent Hammerstein model)

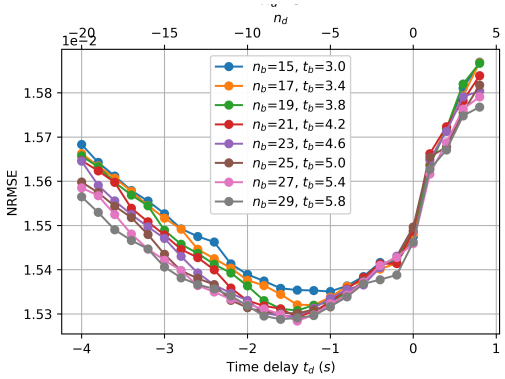

(d) NRMSE Vs n_d (Rate dependent Hammerstein model)

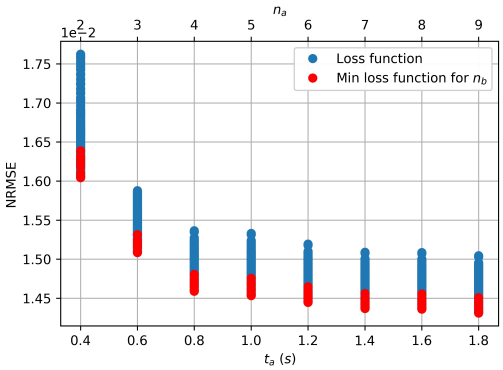

(e) NRMSE Vs n_a (Rate dependent KGP model)

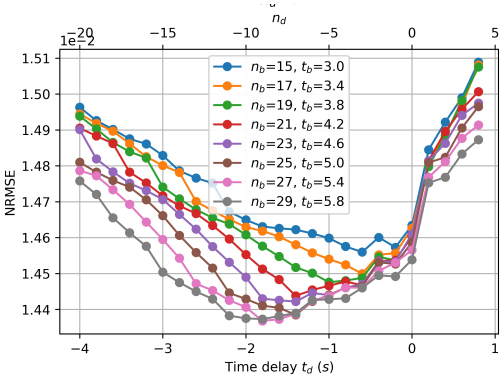

(f) NRMSE Vs n_d (Rate dependent KGP model)

Figure C.5: NRMSE for HP cylinder oscillating at $amp = 0.00\ m$ and $\omega = 0.00\ rad/s$ for realization $R1$ and Range 1, illustrating a comparison between all the system identification models used in this thesis